MAX PLANCK INSTITUTE
OF COLLOIDS
AND INTERFACES

Growth dynamics and mechanical properties of *E. coli* biofilms

DISSERTATION

zur Erlangung des akademischen Grades

„doctor rerum naturalium“

(Dr. rer. nat.)

in der Wissenschaftsdisziplin Biophysik

eingereicht an der

Mathematisch-Naturwissenschaftlichen Fakultät

der Universität Potsdam

von Ricardo Ziege

Hauptbetreuer: Prof. Peter Fratzl

Betreuer*innen: Dr. Cécile Bidan, Prof. Kerstin Blank

Gutachter*innen: Prof. Peter Fratzl, Prof. Kerstin Blank, Prof. Aránzazu Del Campo

‘Nothing in the world is as soft and yielding as water. (…)
The soft overcomes the hard, the gentle overcomes the rigid.’

Lao-Tzu

ABSTRACT

Biofilms are complex living materials that form as bacteria get embedded in a matrix of self-produced protein and polysaccharide fibres. The formation of a network of extracellular biopolymer fibres contributes to the cohesion of the biofilm by promoting cell-cell attachment and by mediating biofilm-substrate interactions. This sessile mode of bacteria growth has been well studied by microbiologists to prevent the detrimental effects of biofilms in medical and industrial settings. Indeed, biofilms are associated with increased antibiotic resistance in bacterial infections, and they can also cause clogging of pipelines or promote bio-corrosion. However, biofilms also gained interest from biophysics due to their ability to form complex morphological patterns during growth. Recently, the emerging field of engineered living materials investigates biofilm mechanical properties at multiple length scales and leverages the tools of synthetic biology to tune the functions of their constitutive biopolymers.

This doctoral thesis aims at clarifying how the morphogenesis of *Escherichia coli* (*E. coli)* biofilms is influenced by their growth dynamics and mechanical properties. To address this question, I used methods from cell mechanics and materials science. I first studied how biological activity in biofilms gives rise to non-uniform growth patterns. In a second study, I investigated how *E. coli* biofilm morphogenesis and its mechanical properties adapt to an environmental stimulus, namely the water content of their substrate. Finally, I estimated how the mechanical properties of *E. coli* biofilms are altered when the bacteria express different extracellular biopolymers.

On nutritive hydrogels, micron-sized *E. coli* cells can build centimetre-large biofilms. During this process, bacterial proliferation and matrix production introduce mechanical stresses in the biofilm, which release through the formation of macroscopic wrinkles and delaminated buckles. To relate these biological and mechanical phenomena, I used time-lapse fluorescence imaging to track cell and matrix surface densities through the early and late stages of *E. coli* biofilm growth. Colocalization of high cell and matrix densities at the periphery precede the onset of mechanical instabilities at this annular region. Early growth is detected at this outer annulus, which was analysed by adding fluorescent microspheres to the bacterial inoculum. But only when high rates of matrix production are present in the biofilm centre, does overall biofilm spreading initiate along the solid-air interface. By tracking larger fluorescent particles for a long

time, I could distinguish several kinematic stages of *E. coli* biofilm expansion and observed a transition from non-linear to linear velocity profiles, which precedes the emergence of wrinkles at the biofilm periphery. Decomposing particle velocities to their radial and circumferential components revealed a last kinematic stage, where biofilm movement is mostly directed towards the radial delaminated buckles, which verticalize. The resulting compressive strains computed in these regions were observed to substantially deform the underlying agar substrates. The co-localization of higher cell and matrix densities towards an annular region and the succession of several kinematic stages are thus expected to promote the emergence of mechanical instabilities at the biofilm periphery. These experimental findings are predicted to advance future modelling approaches of biofilm morphogenesis.

E. coli biofilm morphogenesis is further anticipated to depend on external stimuli from the environment. To clarify how the water could be used to tune biofilm material properties, we quantified *E. coli* biofilm growth, wrinkling dynamics and rigidity as a function of the water content of the nutritive substrates. Time-lapse microscopy and computational image analysis revealed that substrates with high water content promote biofilm spreading kinetics, while substrates with low water content promote biofilm wrinkling. The wrinkles observed on biofilm cross-sections appeared more bent on substrates with high water content, while they tended to be more vertical on substrates with low water content. Both wet and dry biomass, accumulated over 4 days of culture, were larger in biofilms cultured on substrates with high water content, despite extra porosity within the matrix layer. Finally, the micro-indentation analysis revealed that substrates with low water content supported the formation of stiffer biofilms. This study shows that *E. coli* biofilms respond to the water content of their substrate, which might be used for tuning their material properties in view of further applications.

Biofilm material properties further depend on the composition and structure of the matrix of extracellular proteins and polysaccharides. In particular, *E. coli* biofilms were suggested to present tissue-like elasticity due to a dense fibre network consisting of amyloid curli and phosphoethanolamine-modified cellulose. To understand the contribution of these components to the emergent mechanical properties of *E. coli* biofilms, we performed micro-indentation on biofilms grown from bacteria of several strains. Besides showing higher dry masses, larger spreading diameters and slightly reduced water contents, biofilms expressing both main matrix components also presented high rigidities in the range of several hundred

kPa, similar to biofilms containing only curli fibres. In contrast, a lack of amyloid curli fibres provides much higher adhesive energies and more viscoelastic fluid-like material behaviour. Therefore, the combination of amyloid curli and phosphoethanolamine-modified cellulose fibres implies the formation of a composite material whereby the amyloid curli fibres provide rigidity to *E. coli* biofilms, whereas the phosphoethanolamine-modified cellulose rather acts as a glue. These findings motivate further studies involving purified versions of these protein and polysaccharide components to better understand how their interactions benefit biofilm functions.

All three studies depict different aspects of biofilm morphogenesis, which are interrelated. The first work reveals the correlation between non-uniform biological activities and the emergence of mechanical instabilities in the biofilm. The second work acknowledges the adaptive nature of *E. coli* biofilm morphogenesis and its mechanical properties to an environmental stimulus, namely water. Finally, the last study reveals the complementary role of the individual matrix components in the formation of a stable biofilm material, which not only forms complex morphologies but also functions as a protective shield for the bacteria it contains. Our experimental findings on *E. coli* biofilm morphogenesis and their mechanical properties can have further implications for fundamental and applied biofilm research fields.

TABLE OF CONTENTS

LIST OF FIGURES AND TABLES

LIST OF ABBREVIATIONS

adrA	-	Gene involved in curli biogenesis
AFM	-	Atomic Force Microscopy
AP329	-	*E. coli* mutant strain producing pEtN-modified cellulose
AP472	-	*E. coli* mutant strain producing unmodified cellulose
AR198	-	*E. coli* mutant strain with no expression of pEtN-cellulose and curli
AR3110	-	*E. coli* strain producing pEtN-cellulose and amyloid curli
B. subtilis	-	*Bacillus subtilis*
c-di-GMP	-	Cyclic-diguanlyic acid
CLSM	-	Confocal Laser Scanning Microscopy
CsgA	-	Major curli subunit precursor
CsgB	-	Minor curli subunit
CsgD	-	Curli transcriptional regulator
DIC	-	Digital Image Correlation
E. coli	-	*Escherichia coli*
eDNA	-	extracellular DNA
ELM	-	Engineered Living Materials
EPS	-	Extracellular Polymeric Substances
K-12	-	Frequently used *E. coli* laboratory strain
LAP	-	Linear Assignment Problem
LoG	-	Laplacian of Gaussian
LUT	-	Look-up table
P. aeruginosa	-	*Pseudomonas aeruginosa*
P. fluorescens	-	*Pseudomonas fluorescens*
pEtN	-	Phosphoethanoleamine modification of cellulose
PIV	-	Particle Image Velocimetry
PTV	-	Particle Tracking Velocimetry
S. cerevisiae	-	Saccharomyces cerevisiae
S. mutans	-	*Streptococcus mutans*
UTI	-	Urinary tract infection

V. cholera	-	*Vibrio cholera*
W3110	-	*E. coli* mutant strain producing curli fibres

1 INTRODUCTION

The tree of life is an important organizing principle used by biologists to overview the evolution of life on earth.[1] Recent analysis of genomic data of over 1000, yet uncultivated organisms, revealed the dominance of bacterial diversification in early evolution.[1] Fossils of the oldest known, cellularly preserved and colonial microbiota date back to 3.3 – 3.5 billion years.[2] So-called stromatolites are composed of multi-layered microbial mats of filamentous cyanobacteria and other microorganisms, which then became fossilized.[3] Multicellular assemblies of several microorganisms such as bacteria, archaea, fungi or algae are referred to as biofilms nowadays. All biofilms are characterized by the presence of extracellular polymeric substances (EPS), such as proteins, polysaccharides, lipopolysaccharides and eDNA.[3] Most of these biomolecules present in the extracellular space self-assemble to form higher order fibrillary structures.[4]

The formation of a network of EPS biopolymer fibres thus contributes to biofilm cohesion (bacteria cell - cell) and adhesion (biofilm - substrate) by providing a scaffold for bacteria.[5] Other functions that benefit bacteria encased in a dense EPS fibre network include retention of water, physical shielding against environmental challenges or extra nutrient source. Biofilm formation is omnipresent in nature and occurs at interfaces.[6] The three main modes of biofilm growth are: (I) (macro-)colony growth at the solid-air interface, (II) pellicle growth at a liquid-air interface and (III) submerged biofilm growth at a liquid-air interface.[7]

Biofilms are the cause of a pressing medical problem in hospitals worldwide as they favor the resistance of pathogenic bacteria to multiple antibiotics.[8] Clinically significant consequences of biofilm-related infections include the formation of dental caries due to the presence of *Streptococci* or chronic wounds mediated by *Staphylococci*.[9] Further detrimental roles of biofilm formation are reported in industrial settings where they cause clogging of pipelines, bio-corrosion and surface fouling (submerged biofilms).[10] However, biofilms can also have positive impacts in both industrial and natural contexts, e.g. as environmental application for efficient treatment of wastewater[11], by promoting plant growth and defense against plant pathogens through their symbiotic interaction with the roots, and when preventing desiccation and promoting cohesion of soils.[12,13]

In the last years, the beneficial role of biofilms came even more into focus in the context of engineered living material (ELM) considering extracellular polymeric substances as biologically produced protein- and polysaccharide-based materials. The tools of synthetic biology, i.e. genetic modification of bacteria, are utilized to modify these naturally produced biomolecules to provide novel material and medical applications.[14] For example, engineering amyloid proteins with functionalized mussel foot protein led to *B. subtilis* biofilms with tunable adhesion.[15] Also, amyloid nano-fibres from *E. coli* Nissle 1917 have been engineered to use such biofilms as a promoter of gut mucosal healing.[16] Finally, biosensors reporting external stimuli with a fluorescence signal, were made by incorporation of engineered *S. cerevisiae* into bacterial cellulose materials.[17] What unifies these approaches is the potential of such systems to display autonomous, adaptive and self-healing characteristics of living organisms while being engineered to present specific physicochemical and mechanical properties.[18] The ease of genetic modification of single bacteria and their preferred mode of growth as multicellular communities provides the basis for using biology to grow complex structures and to employ their naturally produced bio-nanomaterials.[18]

In that context, it is important to understand that biofilms constitute complex living organisms with the ability to undergo morphogenesis analogous to other multicellular tissues and organisms.[19–22] Gradients of biological activity are generated during the development and maturation of biofilms.[23,24] Indeed, nutrient and oxygen gradients induce a stratified expression of extracellular polymeric substances, in turn leading to highly complex EPS architectures.[25,26] Moreover, the complex organization and the mechanical properties of biofilms are highly influenced by biophysical stimuli such as temperature, fluid flow, pH and the presence of ions.[27,28] As such, environmental stimuli were shown to trigger biological responses at different levels from the molecular to the subcellular, to the cellular and tissue scale.[27,28] Finally, recent studies point out the important role of mechanical processes in determining the macroscopic features of biofilms. In *B. subtilis* and *V. Cholera* biofilms, the complex morphologies result from mechanical instabilities that are in turn determined by an interplay between differential growth, biofilm and substrate material properties, and interfacial friction.[19,29,30]

Yet, a lot remains unknown about the dynamics of *E. coli* biofilm growth, morphogenesis and mechanical properties, and how these latter relate to biological activity. *E. coli* bacteria

constitute a well-studied model system for its cellular and multicellular stress responses, as well as for biofilm growth. Genetic modification of *E. coli* is accessible and promises attractive applications in the emerging field of engineered living materials (ELM). However, how large-scale spatiotemporal patterns give rise to *E. coli* biofilm growth and the emergence of mechanical instabilities is still an open fundamental question. The high adaptivity of *E. coli* biofilms to changing environmental conditions constitutes an interesting avenue to control the material properties of *E. coli* biofilms without the need to utilize tools of synthetic biology. Ultimately, the mechanisms of how the co-expression of rigid amyloid curli fibres and elastic pEtN-modified cellulose fibres gives rise to exceptional mechanical properties of wild type *E. coli* (AR3110) biofilms remain elusive and would deserve more attention for their implications in both fundamental and applied biofilm research. Therefore, my doctoral thesis aims at complementing the current knowledge on the "Growth dynamics and mechanical properties of *E. coli* biofilms".

Chapter 2 first gives an overview of the state of the art on this interdisciplinary topic and highlights the tight interplay between biology, morphology and mechanics during biofilm formation. From this literature review, the three main goals of my work have been formulated as:

1) Clarifying how biological activity alters *E. coli* biofilm growth and morphogenesis on a macroscopic scale.

2) Studying how *E. coli* biofilm morphogenesis and its mechanical properties adapt to an environmental parameter: the water content of their substrate.

3) Estimating how the main components of the EPS matrix of *E. coli* biofilms contribute to the emergent biofilm mechanical properties at the microscale.

To achieve these goals, I have applied experimental approaches from materials science and cell mechanics to monoclonal *E. coli* biofilms, as presented in Chapter 3 (Materials and Methods).

Chapter 4 explores how cell proliferation and EPS matrix production inside *E. coli* biofilms influence the mechanics and dynamics of biofilm expansion and morphogenesis. Therefore, this section first reports a detailed quantification of the spatiotemporal distribution of bacterial cells and EPS matrix components using time-lapse fluorescence imaging. It then presents how tracking micro-particles incorporated into the initial bacterial inoculum enables to obtain spatiotemporal information about *E. coli* biofilm development. Finally, local growth rates are derived from particle displacements and their effect on biofilm and biofilm-substrate interfacial mechanics are discussed.

Chapter 5 presents how *E. coli* biofilm growth, morphology and mechanical properties adapt to changing water contents of their substrates. Biofilms spreading kinetics are first studied with time-lapse brightfield imaging and correlated with their delamination dynamics and their emerging morphology. Biomass accumulation and biofilm water content are then investigated as a function of the water content of their substrate. Finally, a micro-indentation setup is utilized to assess how the mechanical properties of *E. coli* biofilms change as a function of the water content of their substrate.

Chapter 6 demonstrates how the matrix components of *E. coli* biofilm determine their mechanical properties. It first reports the difference in morphology, mass and water content between wild-type and EPS-deficient *E. coli* biofilms. It then details the influence amyloid curli and pEtN-modified cellulose fibres have on the rigidity of biofilms as well as on their adhesion properties as investigated by micro-indentation. The viscoelastic stress relaxation behaviour of *E. coli* biofilms with altered EPS composition is further explored.

Chapter 7 finally discusses the outcome of these three studies in a broader context of biofilm morphogenesis and the mechanical properties of biofilms and potential applications due to their composition of biologically produced protein and polysaccharide fibres.

2 STATE OF THE ART

2.1 Biofilm formation

Bacteria in nature present two modes of growth: the freely swimming planktonic mode and the surface attached sessile mode.[31] While historically the planktonic mode was believed to be the ubiquitous mode of bacteria growth, that view shifted in the last decades. Now, the dominant mode of bacteria growth in nature is believed to be the surface-attached, sessile mode. Biofilms of different microorganism communities are omnipresent on host tissues, plant leaves and roots and marine environments, where they can have both beneficial and detrimental influences.[32] The formation of biofilms is a developmental process, which is initiated by the attachment of planktonic cells to a surface (Fig. 1).[33] Once an irreversible attachment is established, cell division and the production of EPS enhance the adhesion to the surface. Upon maturation, cell aggregates turn into complex 3D structured biofilms, enabling the stratification of gene expression and the co-existence of heterogeneous physicochemical microenvironments.[33] A final stage of biofilm development is the dispersal of planktonic cells from the biofilm, which can colonize new surfaces and thereby re-enter the biofilm life cycle.

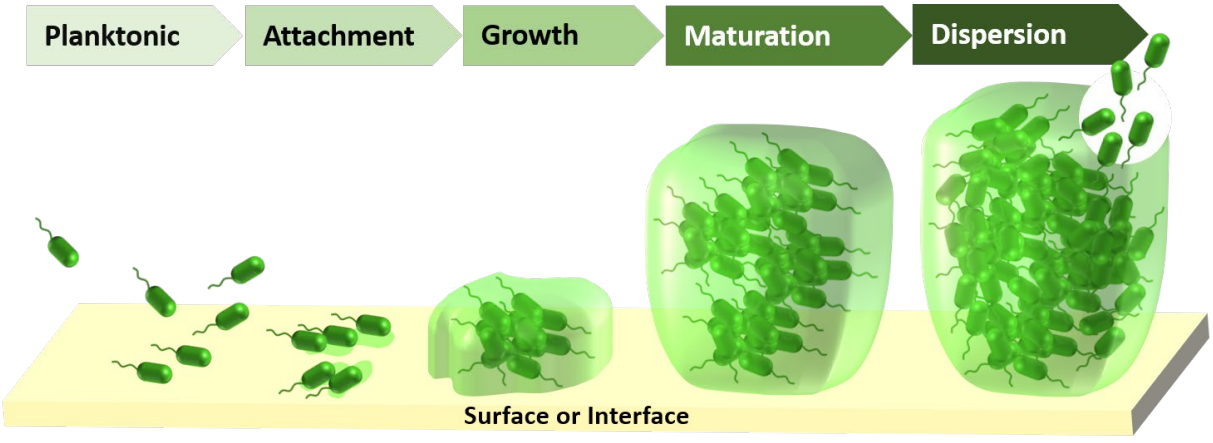

Fig. 1: Biofilm life-cycle presented in five phases. (I) Reversible attachment of planktonic bacteria to a biotic or abiotic surface. (II) Irreversible attachment of bacterial cells to a surface, mediated by their cellular adhesins. (III) Initial growth is characterized by cell division and EPS production, which lead to the formation of surface-attached cell aggregates. (IV) During biofilm maturation, spatial patterns of gene expression lead to differentiated subpopulations of bacteria and heterogeneous physicochemical microenvironments. (V) Biofilm dispersion can be triggered by EPS matrix remodelling leading to the ejection of planktonic bacteria or cellular aggregates from the biofilm.

The initial contact of planktonic bacteria to the surface of host tissues or medical devices is mediated by cell surface-associated adhesins (e.g. type I fimbriae), cellular appendages (e.g. flagella and pili) and other extracellular proteins (e.g. curli fibres).[33] A reversible attachment to the surface is established by overcoming repulsive electrostatic and hydrophobic interactions. Yet, these interactions remain unstable and a substantial amount of attached bacteria migrates back to the surrounding fluid (Fig. 1 - Planktonic).[31] Irreversible attachment is reached by EPS production, which promotes cell-surface and cell-cell interactions while cells cease to move (Fig. 1 - Attachment).[31] Cyclic-diguanylate (c-di-GMP) is an intracellular chemical signal used by many bacterial species to upregulate their expression of EPS, thereby promoting the transition from a planktonic to a sessile state.[34] After attachment, cell division and EPS production lead to the aggregation and clustering of cells, which characterize the early growth phase of biofilms (Fig. 1 - Growth).[33]

Upon maturation, a 3D structured biofilm is formed while EPS matrix components provide a multifunctional and protective scaffold (Fig. 1 - Maturation).[33] Stratification of gene expression and bacterial cell physiology lead to the formation of heterogeneous microenvironments, which further promote cooperative and competitive social interactions between differentiated cell phenotypes.[3] For example, nutrient depletion in the biofilm interior can trigger stationary-phase physiology, which inhibits cell proliferation and thus creates subpopulations of slow-growing or dormant cells.[24] Such subpopulations are shown to be increasingly persistent to some antibiotic treatments.[35] Microcolonies and biofilms mature when bacterial cells reach a growth bottle-neck set by the limited diffusion of nutrients from their environment. This step is often correlated with reaching the maximum thickness of the biofilm. The latest stage of biofilm formation is characterized by remodelling of the EPS matrix or fluidization of the EPS matrix, which enables subpopulations of bacteria to leave the biofilm (Fig. 1 - Dispersion).[31] Further differentiation of cells to sporulating phenotypes and other active dispersal mechanisms promote the dispersal of cell aggregates from densely populated microbial communities.[28,36]

2.2 Spatiotemporal dynamics of biofilm development

2.2.1 Tracking of movement inside microcolonies and biofilms

Rigid biotic and abiotic substrates support the attachment of individual microorganisms, and their co-aggregation enables intercellular signalling and cellular differentiation with gene expression patterns different from those of cells grown in planktonic conditions.[21,37] Spatially structured architectures of bacterial cells and EPS create potential homeostatic zones with optimal use of available nutrients.[37,38] Such spatial patterns of metabolic activity and EPS matrix production are further observable during biofilm spreading at a solid-air interface.[39] Biofilms, as well as microbial swarms, exhibit large-scale spatiotemporal collective behaviours, some analogous to multicellular organisms.[39] Such elaborate cell differentiation patterns and stratification of EPS matrix components provide biofilms with important functions like the enhancement of their mechanical rigidity, the retention of water and nutrients, and enhanced antibiotic resistance.[40–42]

Live single-cell imaging enables simultaneous detection of many single cells.[6] Therefore, it provides a powerful tool to distinguish between single-cell and multicellular stress responses inside microbial colonies.[28] Automated tracking of single cells with confocal microscopy facilitates the acquisition of high spatiotemporal-resolution data of microcolony development for up to 10^4 cells (Fig. 2A).[6] High temporal resolution (5 – 10 min. time intervals) and single cell segmentation allows for cell lineage reconstruction and the measurement of localized growth rates (Fig. 2B).[6] Automated single-cell imaging reveals further multi-scale dynamical processes during *B. Subtilis* swarming expansion. Cell densities are highest in the swarm centre and cell velocities are larger at the swarm periphery.[43] The formation of non-motile clusters of bacteria in the centre and motile rafts (groups of aligned cells) at the periphery dominate their collective behaviour.[43]

During biofilm growth, 2D mono-layered bacteria microcolonies become 3D complex structures. This verticalization results from mechanical instabilities that emerge from cell division in confinement.[44] The overall rate of microcolony expansion increases for large elongated cells in contrast to small round cells which was studied by agent-based modelling and 3D single-cell imaging.[44] The transition from a 2D to 3D *E. coli* microcolony further depends on the asymmetric adhesion of the rod-shaped bacteria to the substrate and to neighbouring bacteria by creating tension and subsequent surface detachment.[45] Yet, to investigate the

dynamics of cm-large macrocolony biofilms containing up to billions of cells, as opposed to mm-sized microcolonies, 3D single-cell confocal imaging is limited. However, a recent approach based on a novel optical system for imaging tissue volumes (Mesolens) enabled the study of intra-colony channels in *E. coli* macrocolony biofilms.[46]

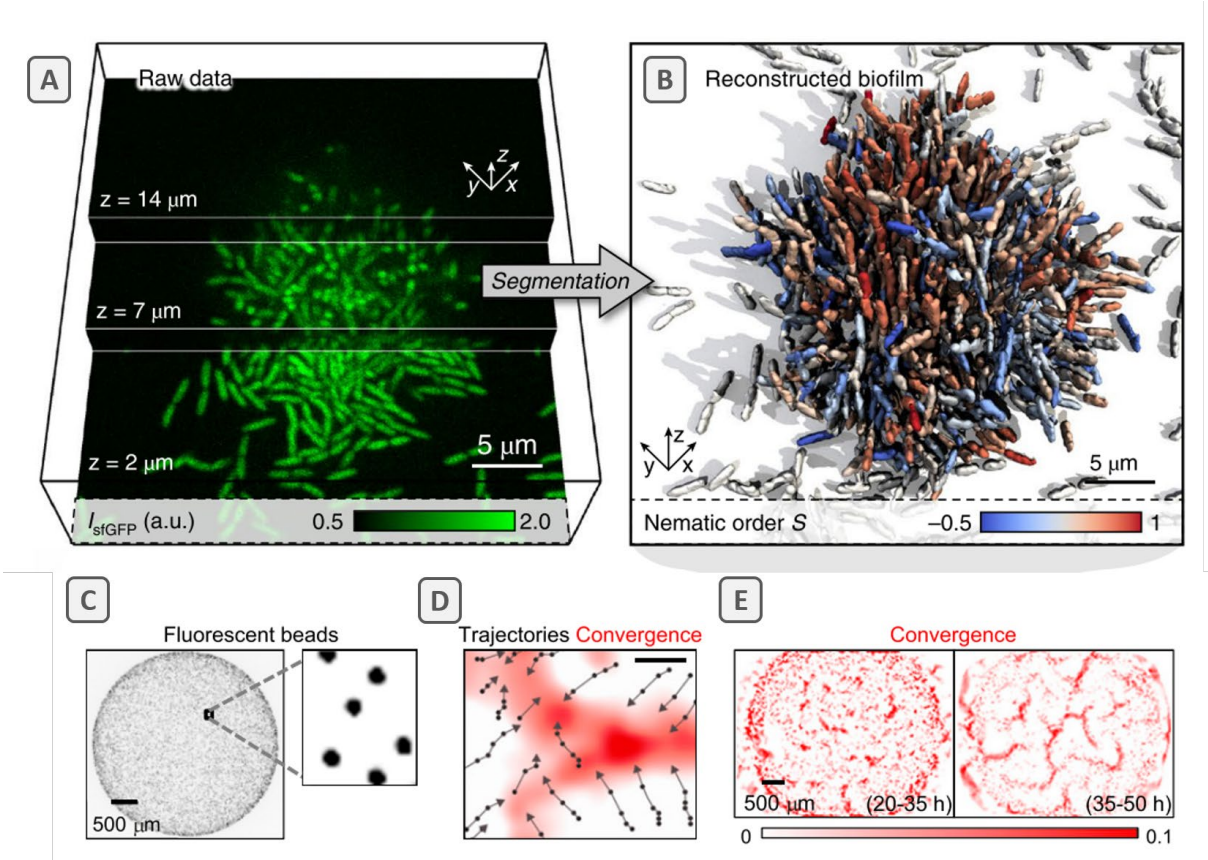

Fig. 2: Live single-cell tracking and segmentation from 3D confocal images inside a microcolony and movement of fluorescent microparticles inside a macrocolony biofilm. (A) *V. cholera* cells expressing green fluorescent protein (sfGFP) and imaged by spinning disc confocal microscopy.[6] (B) 3D reconstruction of the microcolony shown in A, Segmentation of individual cells allowed cell lineage reconstruction due to high time resolution imaging (Δt = 5 – 10 min.), colour indicates the nematic order parameter.[6] (reprinted with permission from Nature Physics) (C) Fluorescent particles mixed to initial cell suspension (inverted fluorescence image).[47] (D) Particle tracking during biofilm development, black arrows and dots indicate particle trajectories. Note that particle trajectories end when leaving the focal plane in the z-direction.[47] (D, E) Convergence field extracted from interpolated vector field of particle trajectories for two time windows.[47]

When single-cell resolution is not achievable, a continuum perspective can prove useful to describe the mechanics of a developing organism.[48] From a continuum perspective, a local volume element of tissue contains many single cells and EPS matrix molecules and is described by averaged properties (e.g. tissue strain and shear rates).[49] Particle image velocimetry

algorithms (PIV) used to analyse biofilm growth rely on a continuum view by constructing flow fields based on spatial image cross-correlation between two time steps.[19,36] This method is based on continuum mechanics (material model is a continuum) and fluid dynamics (measuring flow fields). Embedding fluorescent microparticles into deforming tissues (e.g. biofilms) constitutes another method to sample localized growth and buckling.[47] Particle tracking velocimetry algorithms (PTV) provide discrete information of the velocity of single particles inside a medium in motion. These two approaches (PIV and PTV) can be combined to reach reasonable spatial accuracy while saving computational time. For example, such combined cross-correlation algorithms have been used to determine the displacement fields of fluorescent beads embedded in soft cell substrates in the context of cell traction force microscopy.[50] To account for localized and large displacements, it proved useful to use small sub-window sizes with substantial overlap before cross-correlation of subsequent image pairs.[51]

Embedding fluorescent beads in living tissues and using their displacement to derive stresses proves challenging due to unclear binding sites of beads, viscoelastic material properties of the tissues and their potential growth in time. Yet, the analysis of particle trajectories in *B. subtilis* biofilms helped determine that localized cell death might be a precursor to initiate the formation of wrinkled structures by focusing mechanical forces (Fig. 2D).[47] Fluorescent particles trajectories were shown to converge around the wrinkle sites (Fig. 2D, E) after localized patterns of cell death were detected.[47]

2.2.2 Spatiotemporal dynamics of macrocolony biofilm growth

Tracking fluorescent particles inside biofilms enables following the movement and buckling of biomass. On the other hand, time lapse-imaging of fluorescent reporter genes opens the possibility of measuring spatiotemporal distributions of different cell phenotypes, as demonstrated in *B. Subtilis* biofilm development (Fig. 3A).[36,52,53] Non-homogenous patterns of biological activity generate forces that drive biofilm expansion over a substrate. For example, spatially localized cell proliferation and extracellular matrix production constitute the main biological origins of non-uniform expansion of *B. subtilis* biofilms at the solid-air interface (Fig. 3B).[41,54,55]

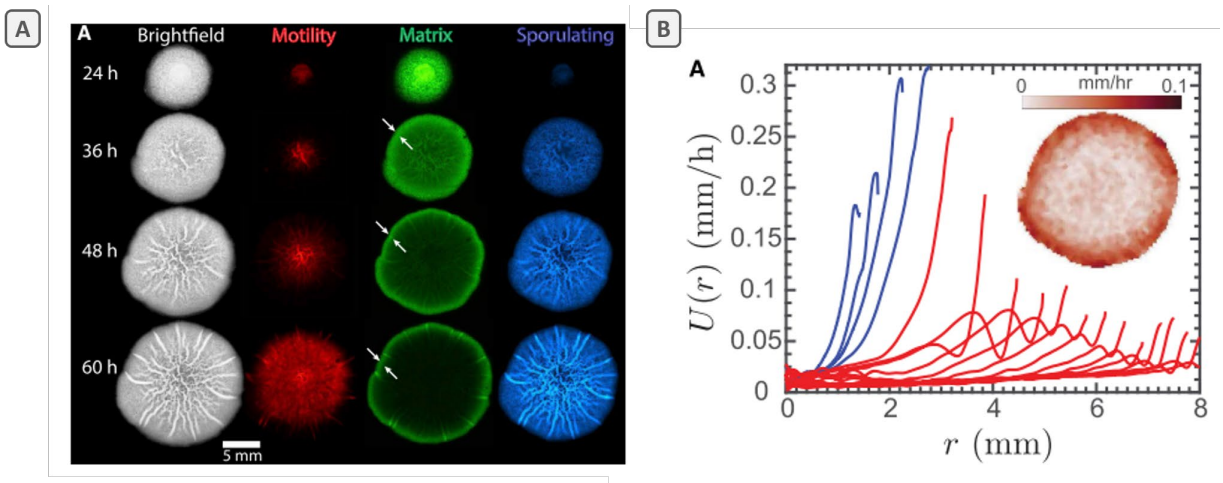

Fig. 3: Non-uniform distribution of different cell phenotypes and non-uniform radial expansion in *B.subtilis* biofilms. (A) Time-lapse fluorescence imaging of a developing biofilm from a triply-labelled *B. subtilis* MTC871 strain (P_{hag}-mKate2 reporter for motility (red), P_{tapA}-cfp reporter for matrix production (green), P_{ssp}B-citrus reporter for sporulation and brightfield images at 24, 36, 48 and 60 h). (B) Azimuthally averaged radial velocity profiles *U*(r), blue curves indicate increasing maximum edge velocities (starting at 10 h with curves being 100 min. apart) and red curves indicate decreasing maximum edge velocities; the inset shows a map of velocity magnitude at 36 h, derived from PIV done on brightfield time-lapse series.[36]

Time-lapse fluorescence imaging of fluorescent reporters provides a non-invasive technique for spatiotemporal tracking of biofilm growth and the distribution of different cell phenotypes.[52] The up-right geometry, low magnification and long working distance of stereomicroscopes is particularly suited to monitor the growth of cm-sized biofilms at the solid-air interface. Taking advantage of the circular biofilm geometry, the construction of kymographs helped follow these three cell phenotypes in space and time.[52] Kymograph plots depict azimuthal averages of light intensity as a function of space (biofilm radius) and time (biofilm age).

During *B. Subtilis* biofilm development, matrix production becomes increasingly localized within an annular region at the biofilm periphery (< 500 µm, Fig. 3A).[36] While active matrix production is present over the whole biofilm area (Fig. 3A – 24 h) in the early stage of *B. Subtilis* biofilm development, it localizes to the annular periphery already 12 h later (Fig. 3A – 36 h).[36,52] By estimating the expansion rates of the different cell phenotypes, motile and sporulating cells were found to be almost at rest, whereas the matrix-producing phenotype dominated the biofilm expansion at the periphery.[53] Biofilm expansion, as well as the distribution of the

different cell phenotypes, are further influenced by environmental factors like nutrient availability, substrate stiffness and colony competition.[53]

The change of localization of matrix-producing cells from the biofilm centre (early stage) to an annular periphery (late-stage) suggests that the youngest biomass is increasingly produced at the biofilm edge due to progressive nutrient depletion in the centre.[36] The physical expansion of *B. Subtilis* and *V. cholera* biofilms at the solid-air interface was thus shown to follow at least three basic regimes.[20,36,53] The initial regime takes place before steady expansion is reached and was shown to be edge-dominated.[20] This early stage of biofilm development has been described as a lag period (t ~ 10 h) as the biofilm remains restricted in the centre and the periphery only slowly propagates outward.[20] The second kinematic regime consists of a fast and accelerated radial expansion[20,39] resulting from a homogeneous growth (increasing velocities from the biofilm interior to the biofilm periphery in Fig. 3B – blue curves).[36] At a critical time t_c the maximum expansion velocity is reached and this time correlates with the peak of matrix production during *B. subtilis* biofilm development.[36] This critical time t_c also marks the transition to a third kinematic regime, characterized by a deceleration of the radial expansion. This transition was suggested to result from a transition of homogenous bulk growth to edge-only growth,[36] which is likely driven by nutrient depletion in the biofilm interior, accompanied by a drop of matrix production.[20,36]

Spatial and temporal patterning of cell phenotypes and biofilm growth are not limited to the 2D expansion at the solid-air interface. Indeed, most biofilms present complex and intricate 3D architectures[24,25] and the vertical stratification of bacterial microcolonies and biofilms leads to differential zones of metabolic activity. Spatial heterogeneities in biofilms, such as heterogeneous production of extracellular polymeric substance, result from gradients in nutrient and oxygen availability.[40,56] Microelectrode experiments introduced the measurement of oxygen concentration gradients inside biofilms with micrometre depth resolution.[57] With this methods, De Beer et al could prove the formation of anaerobic zones inside cell clusters exposed to aerobic conditions.[58] Variations in metabolic activity are thus expected along both the lateral direction of a growing biofilm (parallel to the substrate) and its vertical direction (perpendicular to the substrate).

Such stratification of nutrient and oxygen availability and gene expression results in vertical gradients of production and quantity of EPS matrix molecules.[5,40] The EPS network is meant to

preserve the structural integrity of the multicellular microbial community as it connects immobilized bacteria in close vicinity and constitutes an immediate protective environment.[5] Exopolysaccharides were shown to be involved in the formation of the 3D architecture of *V. cholera* biofilms,[59] where they also act as macromolecular osmolytes.[60] They enable nutrient rich-water to be drawn into the biofilm, which leads to a physical swelling of its EPS network, a property that EPS-mutant strains often lack.[61] Swelling can thus provide additional spreading forces for biofilm radial expansion.[62]

As shown for *B. subtilis* and *V. cholera*, the distribution of matrix production and cell proliferation is uneven in biofilms grown by various biofilm-forming species and evolves in non-uniform patterns on a macroscopic scale. Interestingly, *E. coli* biofilms also have intricate 3D EPS architectures and biofilm morphologies,[23,63] yet a dynamical investigation of the spatiotemporal distribution of biological activity at a large scale is still lacking. Further insights into the correlation between biological and mechanical processes that drive *E. coli* biofilm morphogenesis require their correlation in space and time and still constitute a scientific challenge.[47]

2.3 Biofilm morphogenesis

Morphological development in organisms is not only controlled by large-scale gene expression programs, but also mechanical forces contribute to the emergence of shapes in nature.[64] Morphomechanical processes shape plant organs such as leaves by differential growth leading to twisting, bending, and saddle shape formation.[65] The wrinkling of developing vertebrate guts leads to looping patterns allowing the gut to fit inside the abdominal cavity.[66] Another example is the inward folding of the cerebral cortex of large mammals, which significantly increases its surface area.[67]

Natural systems develop such structures by simple processes including differential growth, drying, and/or confinement.[68] Likewise, biofilms attached to a surface can undergo morphological transitions, such as initially smooth bacteria colonies that develop into complex morphologies during growth.[69] One model suggests that localized cell death patterns serve to focus the mechanical stresses, which determine biofilm morphogenesis.[47] More recently, a theory of global mechanical instabilities was proposed to govern biofilm morphogenesis.[19,30,70] As mechanical instability models have been previously proposed in abiotic systems, similar basic mechanical principles are expected to elucidate biofilm morphogenesis.[71]

2.3.1 Surface instabilities in film-substrate systems

For a long time, tissue folding has been understood to be guided by mismatch strains in different biological layers of tissue.[72] A wide variety of morphological surface structures is observed in the development of cells, tissues, organs and microbial communities depending on the physical constraints imposed (e.g. boundary conditions). When considering unidimensional growth alone, such surface instabilities can lead to wrinkles, creases, ridges and delaminated buckles, among others (Fig. 4A).[29] One model proposed to study the emergence of mechanical instabilities in biofilms consist of a soft bilayer system made of a thin and stiff film, which grows while being attached to a thick and soft substrate.[68]

One way of inducing stresses in a thin film-substrate system is to imagine the two layers as initially detached in a stress-free state with lengths $l_f < l_s$ (Fig. 4B).[71] The film becomes pre-stretched to the length of the substrate l_s, the layers are attached and left to relax to a combined length l. Upon stress relaxation, the system becomes mechanically unstable and minimizes its potential energy by bending the surface (Fig. 4B). The final morphology can be

controlled by changing the extent of pre-stretching, the mechanical properties of the thin and/or the thick layer and their adhesion to each other (Fig. 4A and C).[29,73]

In the model, these physical determinants can be normalized into the dimensionless parameters of modulus ratio between film and substrate ($\frac{\mu_F}{\mu_S}$), mismatch strain ε_m and normalized adhesion energy ($\frac{\Gamma}{\mu_S \cdot H_F}$) (Fig. 4C).[29] Note that more than one mode of mechanical instabilities can coexist, and transition into another, for example by increasing the pre-stretch to a critical value for transition.[73] Also, it was shown that a system with $\frac{\mu_F}{\mu_S} < 1.3$ is unable to wrinkle but instead forms creases under higher strain, and delaminates locally when the adhesion energy between the film and the substrate is small (Fig. 4A – iii).

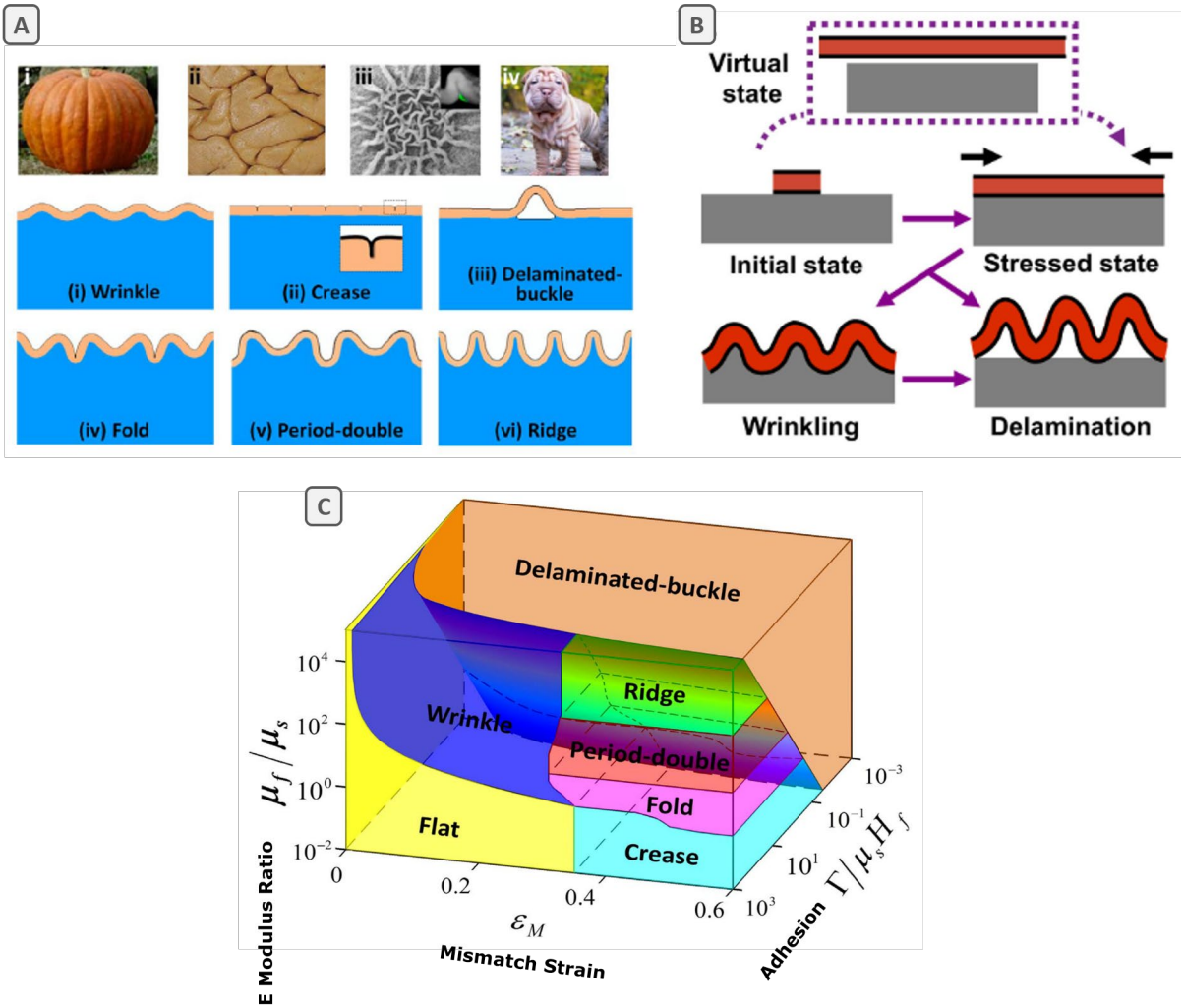

Fig. 4: Different modes of growth-induced surface instabilities. (A) Depiction of wrinkle, crease, delaminated buckle, fold, period double and ridge instabilities and some examples where they occur in nature.[29] (B) Growth-induced in-plane stresses give rise to wrinkling and potential delaminated buckles.[19] (reprinted under Creative

Commons BY 4.0 licence) (C) Three-dimensional phase diagram of growth-induced surface instabilities governed by stiffness ratio of film to substrate, mismatch or growth strain and normalized adhesion energy[29]; (reprinted under Creative Commons BY 4.0 licence)

2.3.2 Morphomechanics of bacterial biofilms

At a solid-air interface, biofilm growth leads to both lateral spreading and accumulation of internal mechanical stresses, which are introduced by two-dimensional growth into increasingly constrained space.[19,20,63] More complexity to the morphogenesis model of bacterial biofilms is added when accounting for the biological anisotropy and spatial heterogeneity of growth. One model proposed incorporates a 2D growing disk adhering to an elastic layer.[30] To explain the growth pattern, the total growth strains need to be decomposed into elastic and growth strains such as $\varepsilon^{total} = \varepsilon^{elastic} + \varepsilon^{growth}$. Due to the constraints imposed by the substrate layer, growth introduces compressive stresses in the adhering disk layer. Just as in the one-dimensional case mentioned above, when a critical growth strain ε_c of the film is reached, the surface starts to destabilize. This critical growth strain was shown in simulations to decrease with increasing stiffness ratio $\frac{\mu_F}{\mu_S}$ ($\varepsilon_c \sim \left(\frac{\mu_F}{\mu_S}\right)^{-2/3}$) and to depend on the anisotropy of the growth strains (Fig. 5A).

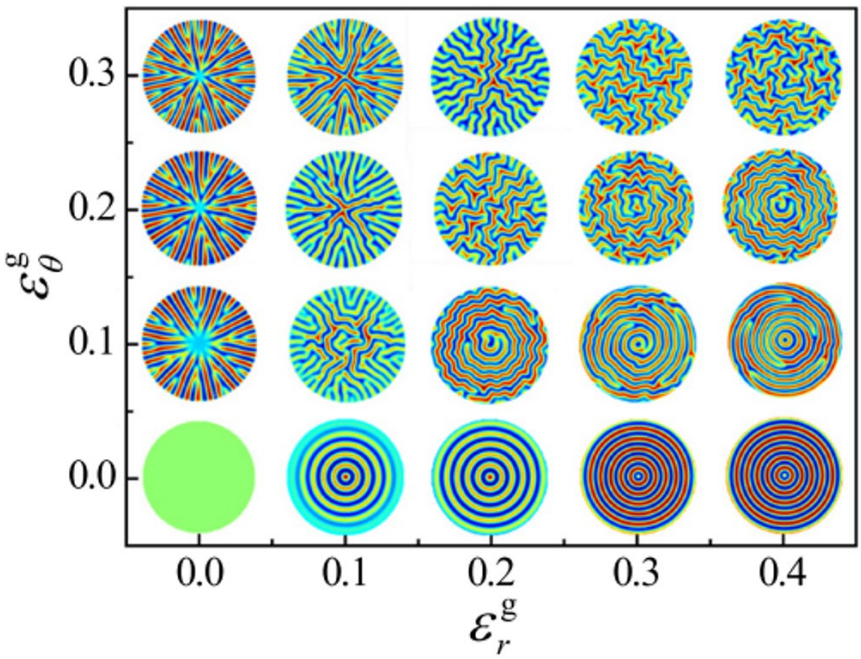

Fig. 5: Complexity of morphological structures, which emerge in simulations of growing flat disks with anisotropic growth strains. Domination of either radial or circumferential growth strains of a flat disk gives rise to radial, circumferential and mixed morphologies.[30] (reprinted with permission from AIP publishing)

To release internal compressive stress, flat biofilms buckle out of the growth plane. This leads to a variety of complex morphologies, including radial, circumferential or zig-zag wrinkles and delaminated buckles that subsequently emerge in different regions of the biofilm (Fig. 5A). These simulations predict that if radial growth ($\varepsilon_r > 0;\ \varepsilon_\varphi = 0$) dominates, concentric-ring patterns are created as observed in *E. coli* W3110 biofilms.[63] In the case of predominantly circumferential growth ($\varepsilon_\varphi > 0;\ \varepsilon_r = 0$), circumferential buckling occurs which leads to periodic wrinkle patterns as observed in *E. coli* AR3110 biofilms.[63] In the third case of isotropic growth, unregular or labyrinth (zig-zag) patterns dominate. Most biofilms grown at solid-air interfaces reveal circumferential, radial or isotropic wrinkling patterns, varying in space and time depending on the growth conditions and the underlying biological processes.

In the case of radial wrinkles, the wrinkle wavelength follows a similar scaling law with respect to the stiffness ratio parameter as for the one-dimensional case ($\lambda \sim \left(\frac{\mu_F}{\mu_S}\right)^{1/3}$). After reaching the critical growth strain, wrinkles forms and their amplitude increases by continuous growth. The film deforms together with the substrate, thus creating high tensile interfacial stresses, which might overcome the adhesive strength between the film and the substrate and give rise to delaminated buckles (Fig. 5B).[71] Therefore, continuous growth favours delaminations, especially if the film only weakly adheres to its substrate.[74] The adhesion energy is another parameter influencing biofilm morphogenesis, which was studied in simulations. For example, it was found that enhanced interfacial sliding promotes longer and denser folds, whereas increased normal bonding prevents biofilms from delaminating and favours wrinkling.[70]

Only a few studies couple experimental biofilm growth measurements with a model of mechanical instability to clarify biofilm morphogenesis, but they revealed further important details. For example, Yan et al quantified the morphogenesis of *B. subtilis* biofilms with such an approach. By measuring the wrinkle wavelength as a function of radial position r, biofilm thickness and biofilm-to-substrate stiffness ratio, they validated the scaling power law of $\lambda \sim \left(\frac{\mu_F}{\mu_S}\right)^{1/3}$ and therefore suggest the applicability of this model for biofilm morphogenesis.[19]

The soft bilayer model, which prevents wrinkling for films with $\frac{\mu_F}{\mu_S} < 1.3$ was found violated and was therefore extended to include a compliant intermediate layer. This addition allows wrinkling even in film-substrate systems of comparable stiffness ($\frac{\mu_F}{\mu_S} = 1$). Such a compliant intermediate layer could be an interfacial layer providing adhesion, or a layer of reduced matrix

production, which still enables the deformation of the rigid top-layer upon biofilm growth. Therefore the advantage of a tri-layer model is that the substrate does not need to undergo substantial deformation.[19]

Biofilm morphogenesis represents a complex three-dimensional growth problem, which solution also highly depends on additional physicochemical signals from the biofilm environment (e.g. substrate properties).

2.3.3 Physicochemical mechanisms influencing biofilm morphogenesis

As early as 1968, Cooper et al proposed that the diffusion of glucose in agar plates densely covered with microcolony is unlikely to govern the radial growth rate of colonies as growth ceases after about 1 day.[75] Yet, growth becomes diffusion-limited on more sparsely covered plates and when microcolonies are cultured for several days.[75] Such growth limiting factors give rise to perimeter undulations and ultimately morphological transitions of microcolonies and biofilms.[20,75,76] In contrast to macromolecular solutes, the diffusion of small solutes, such as glucose in agar gels, is comparable to free diffusion in water due to the high water content.[77]

However, it is reported that the water content of agar substrates does influence biofilm growth and morphogenesis. Indeed, biofilms were shown to reach larger spreading diameters when increasing the agar concentration of the substrate.[78] The role of substrate water content (i.e. agar concentration) in the interplay of biofilm growth and morphology has been studied in biofilm model organisms such as *B. subtilis*[52,79] and *V. cholera.*[19,60,80] Some studies suggest that the change of agar water content predominately influences biofilm morphology by changing the stiffness of the agar substrate.[19] Yet, other authors demonstrated the minor role of substrate stiffness on the observed differential biofilm growth by performing a similar experiment on semipermeable membranes laid on the different agar substrates.[55] In the latter case, the bacteria were shown to synthesize EPS macromolecules that establish an osmotic pressure difference between the biofilm and the substrate, leading to water transport, swelling and thereby enhanced nutrient uptake by the biofilm.[60,81]

Indeed, osmotic pressure gradients can play an important role in the surface spreading of biofilms.[61,62] *B. subtilis* biofilms grown from wild-type and flagella-deficient strains are reported to spread at comparable rates but much faster compared to EPS deficient mutants.[61] As such, the presence of EPS macromolecules seems to provide biofilms with a physical mechanism for

generating osmotic spreading, which is more relevant than bacteria motility.[61,62] A very recent study suggests that an interplay of osmotic pressure and a poroelastic response of the substrate governs biofilm growth and morphology.[82] The generation of osmotic pressure differences is particularly relevant at the expanding front of a biofilm, where recently produced EPS molecules can act as macromolecular osmolytes.[39,55] In the biofilm centre, the EPS scaffold presents a swollen EPS network at osmotic equilibrium with the substrate.[39] The osmotic pressure of an EPS network applied against a compliant substrate can further compress the substrate by fluid intake and thereby lead to persistent mechanical deformations.[83]

Surface forces also influence biofilm growth and morphogenesis at the solid-air interface. For example, the wild-type *B. subtilis* strain NCIB 3610 is known to produce surfactin, a lipopeptide acting as a biosurfactant.[84] A transition from continuous to arrested spreading at the solid-air interface was described for mutant strains lacking surfactin production, thus suggesting the determining role of surface and wetting phenomena in biofilm spreading.[85] More recently, cationic polyelectrolyte substrate coatings were shown to impair biofilm spreading, due to altered surface charges and interfacial energies.[86] Potential interaction of charged molecules with bacteria cell walls or EPS fibres might therefore aid in creating friction between a growing biofilm and its substrate. The friction of biofilm and substrate resists the expansion of a biofilm along the substrate. In the bulk, friction interferes with biofilm expansion, whereas at the biofilm front it was shown to cause an increase of the front leading angle.[20]

Biofilm morphogenesis is expected to emerge from mechanical instabilities, which arise in the biofilm-substrate system.[19] Simulations and theoretical considerations reveal the important role of three parameters governing the emergence of complex morphologies in soft bilayer systems: (I) mismatch strains introduced by biofilm growth, (II) stiffness ratio and (III) the adhesion energy between biofilm and substrate (Fig. 4C).[29] Yet, little effort was undertaken to design biofilm growth experiments validating the proposed mechanisms and their influence on the emergence of complex morphologies.

Dynamic and localized monitoring of biofilm growth until the late stages of biofilm development can provide further insight into the influence of mismatch strains on the emergence of mechanical instabilities. An osmotic equilibration between substrate and biofilm is expected to control the water content and thereby the mechanical properties of biofilms.[40,55] Thus, how the water content of the substrate can be utilized as an external stimulus influencing

biofilm growth, mechanical properties and morphology remain to be explored. Most experimental efforts studying biofilm morphogenesis rely on the biofilm model systems of *V. cholera* and *B. subtilis*. Yet, a dynamic investigation of *E. coli* biofilm growth and morphogenesis could complement these efforts, given their ability to form complex wrinkle and buckle morphologies.

2.4 Mechanical properties of biofilms

In the last decades, the investigation of biofilm mechanics was approached by many disciplines like microbiology, materials science and soft matter physics.[56] Studies about biofilm mechanics are expected to enhance the understanding of the biofilm life cycle, the importance of its viscoelastic material properties to survive in static and flow environments, or the mechanical removal of biofilms. Debridement (or mechanical scraping) of biofilms is a classical procedure in the care of chronic wounds, where disrupting the cohesiveness of biofilms makes the remaining adherent bacteria more susceptible to antibiotics.[87] Further important studies including biofilm mechanics target the prevention of biofilm formation or their beneficial use in industrial or bioprocessing settings, such as wastewater treatment.[11]

2.4.1 Biofilms as viscoelastic materials

In the context of soft matter physics, biofilms are described as complex fluids with viscoelastic material properties.[40] Bacterial cells are seen as colloids, which are embedded in a hydrated and viscous EPS matrix made of different macromolecules. As the hydrated EPS matrix contains more than 70 % of water, biofilms are further modelled as hydrogels.[88,89] Viscoelasticity is characterized by a time- and rate-dependent mechanical response of the material.[90] One portion of the total stress energy upon deformation is stored in a reversible, elastic manner, whereas another portion of the energy dissipates over time. Energy dissipation can enable biofilms to deform under large mechanical perturbations without failure.[91]

From rheometer experiments one can derive the viscoelastic mechanical parameters of elastic shear modulus G' and viscous shear modulus G''. Creep and stress relaxation experiments respectively measure the deformation under constant stress and stress relaxation upon constant deformation. When modelling the stress response of biofilms during stress relaxation, multiple characteristic time scales have been identified in relation to the composition of the EPS matrix.[92] Furthermore, bacterial cells present the highest masses inside a biofilm and are thus slowest to rearrange. Consequently, bacterial rearrangement is expected to dominate the long-term stress relaxation behaviour,[90] whereas the flow of water through the biofilm network is expected to dominate the relaxation behaviour on very short time scales (< 1 s). Biofilm viscoelasticity is proposed to have emerged as a survival adaptation for biofilms to withstand challenges in their environment, such as fluctuating shear stresses in flow environments.[93]

In biofilm research, the polymer network consists of EPS molecules such as proteins and polysaccharides. The matrix usually accounts for volume fractions of dry biomass larger than 0.5 in contrast to the volume fraction of bacterial cells. This justifies the assumption that EPS matrix components are the main mediator of the response of the material to deformation.[94] Furthermore, single bacterial cells are much more rigid than the surrounding hydrated EPS matrix, spanning a range of a few to several hundred MPa for gram-positive and gram-negative bacteria compared to orders of magnitude lower rigidities of the biofilm matrix ranging from few to several hundred kPa.[95] Yet, not only does EPS matrix volume fraction influences biofilm rigidity, but also the type of EPS components and their mutual interactions.

In *P. aerigunosa* biofilms, increased production of the main EPS polysaccharide Psl increases the biofilm rigidity, whereas increased expression of Pel and alginate had no influence on biofilm elasticity.[96] A similar behaviour was reported for *P. fluorescens* biofilms, which become more ductile when the EPS-to-cell ratio is increased.[97] Interactions between different EPS components further promote biofilm cohesion as demonstrated by the prevention of mechanical failure in *S. mutans* biofilms.[98] Understanding the molecular mechanisms of interactions between different EPS matrix components is therefore essential for a thorough explanation of the macroscopic mechanical rigidity of biofilms.

Most soft and biological materials, such as mammalian cells or tissues, exhibit viscoelastic material behaviour due to their complex arrangement of cells, intra- and extra-cellular fibres, and high water contents. Biofilms share some similarities to other multicellular tissues, especially soft collagen-rich tissues (single cells embedded in a soft matrix, growth in time).[99] Viscoelastic behaviour and elasticity might thus be a prerequisite for biofilm self-organization.

2.4.2 Heterogeneity of mechanical properties in space and time

Biofilms are complex, highly heterogeneous and living materials. Consequently, biofilm material properties will present high intra- and inter- biofilm variability.[56] Beside their morphological development, their material properties develop over time. Therefore, one needs to account for the highly time and scale-dependent material response when assessing biofilm mechanical properties. As discussed before, biofilm materials can behave as a solid on very short time scales, whereas they reveal fluid-like behaviour on longer time scales.[100] This complex response to mechanical deformations leads to difficulties of comparing mechanical

parameters across different studies, even when considering the same bacterial strain grown in different conditions.[56] The living nature of biofilm growth also makes the standardization of sample preparation and mechanical test conditions challenging.

Biofilms are considered as composite materials, whereby colloid-like cells are embedded in a hydrated matrix of EPS fibres. Another level of structural heterogeneity derives from gradients of nutrients and oxygen, which result in gradients of metabolic activity and EPS production.[40] Therefore, local mechanical properties are determined by the local composition (cell density and EPS density) and EPS network structure. Biofilms can also exhibit porous structures or channels for nutrient transport and diffusion, adding to the heterogeneity of their mechanical response.[46,81]

As the EPS matrix is highly hydrated, biofilms contain more than 70 % of water and protect the encased bacteria from desiccation.[12] Thus, biofilm mechanical properties are expected to be susceptible to the moisture in their environment. Porous structures, liquid-filled channels or EPS matrix-free regions have locally different water contents, thereby leading to a locally softer material response (reduced Young modulus *E*). Upon compression of a biofilm material, water flows out of the biofilm through its porous EPS network structure, whereas upon relaxation water can be drawn back into the biofilm.

Exposure to osmotic stress (PEG-8000) in the environment was shown to stiffen *S. mutans* biofilms by a change of the osmotic equilibrium of biofilm and environment.[101] Such time- and length-scale dependant mechanical behaviour upon internal fluid redistribution is known as poroelasticity.[102] On a macroscopic level, both viscoelastic and poroelastic materials undergo stress relaxation, yet *via* different microscopic or molecular mechanisms.[103] Viscoelastic material behaviour is facilitated by rearrangement or breaking of physical or chemical crosslinks of a polymer network or by simple disentanglement of polymer strands. Poroelastic material behaviour instead is analogous to compressing a sponge: upon compression water is moved out of a porous matrix.[103]

Biofilms are multicellular, living systems with the ability to adapt their mechanical properties to environmental stimuli. As presented before, different small molecules (like water) and other chemicals can alter the mechanical properties of biofilms. Nutrient availability can further influence biofilm mechanical properties. For example, *P. fluorescens* biofilms grown under low nutrient conditions stiffen (higher Young modulus) compared to the same biofilms grown under

high nutrient conditions.[104] Temperature is another environmental cue affecting biofilm stiffness. *E. coli* biofilms grown at a temperature below 30 °C yields maximum expression in amyloid curli protein and produce stiffer biofilms than at 37 °C.[105] Another strong effect on biofilm mechanical properties can be achieved by the addition of di- and trivalent metal ions in the culture medium (Cu^{2+}, Zn^{2+}, Fe^{2+}), which are proposed to engage electrostatic interactions and/ or crosslinking of EPS macromolecules, leading to more rigid *B. subtilis* biofilms.[106] In this sense, biofilms are 'active' materials with the ability to adapt their material properties to a wide range of biophysical cues (such as water, nutrients, osmotic stress, presence of ions).[27] Therefore a dynamic adaptation to environmental stimuli offers new routes to tune biofilm material properties.

Due to the highly heterogeneous and adaptable structure of biofilms, biofilm material properties thereby are length- and time-scale dependent and bulk mechanical measurements will be significantly different from micro-scale measurements.[107] The choice of the method and scale are therefore an important aspect to account for in any mechanical study of biofilms.[56]

2.4.3 Mechanical characterization of biofilms

Most mechanical characterization types of equipment were developed for studying engineering materials, like metals, ceramics and polymers. Consequently, they often prove inadequate for the study of soft biological materials.[56] For example it is impractical, and often impossible, to produce reproducible biofilm samples for extensiometric measurements due to their softness and adhesiveness. Yet, other more advanced techniques, such as nano- and microindentation or tracking of active or passive microparticles, inspired by cell mechanobiology have proved more useful.[98,105]

Owing to biofilms heterogeneity, one needs to distinguish between bulk and localized testing (Fig. 6). Static assays are performed on submerged biofilms or biofilm grown at the solid-air interface while loading the biofilm material in shear, compression or tension. The material properties of biofilms are numerous and include elastic, plastic, viscous, poroelastic or adhesive mechanical behaviour. Yet, a common requirement is to measure small forces in a range of multiple length scales (nm - mm).

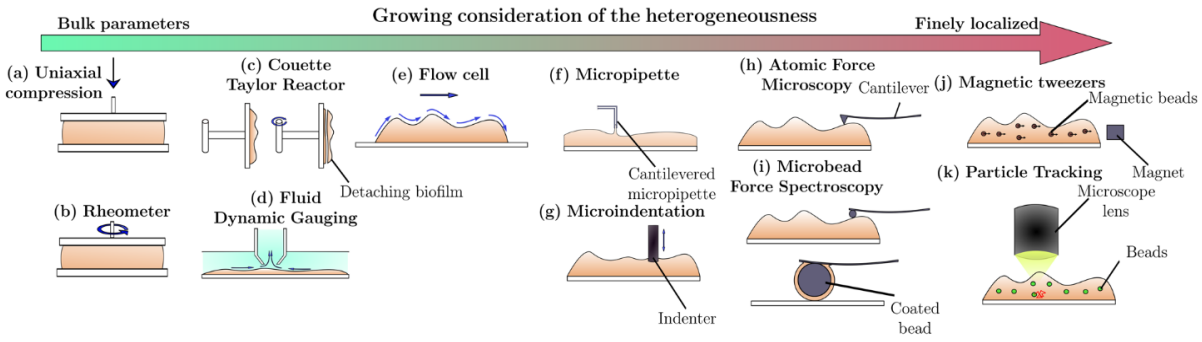

Fig. 6: Illustration of mechanical test equipment sorted by length scale of mechanical probing (from bulk to finely localized)[56]; (reprinted under Creative Commons BY 4.0 licence)

One method for measuring the resistance to shear forces, which dominate in flow environments, is the rheometer (Fig. 6 - rheometer).[96] Yet, the sample preparation protocols for rheological experiments are limited, because they often involve scraping biofilms from their substrate or removing them from a liquid interface, thereby potentially destroying their micro-scale EPS matrix architecture. Such limitations have partially been overcome by culturing biofilms on a rheometer plate *in-situ* and testing them in native conditions without the need for prior handling.[108,109] Although there are more advanced micro-rheology methods, which involve the incorporation of nano- or micron-sized particles, classical rheometer characterization is limited by only measuring bulk mechanical properties (Fig. 6 – rheometer).

Other static mechanical assays, which take into account biofilm heterogeneity, include nano- and micro-indentation, which measure the mechanical interaction of a material surface to a harder tip of defined geometry (Fig. 6 – AFM and microindentation). Upon loading by the tip, the biofilm surface becomes compressed.[56] The load applied on the sample is recorded as a function of displacement of the tip during approach and rentention of the tip, and different models for tip-material interaction are used to derive mechanical parameters.

Hertzian contact models describe the indentation upon contact of a spherical indenter with a purely elastic material.[110] Precautions are necessary when applying such a model on soft biofilms due to their viscoelastic and adhesive material behaviour.[110] However, the use of Hertzian models is still found valid, when indentation depths do not exceed 1/10 of biofilms thickness. Elastic parameters upon compression (i.e. Young modulus *E*) are then extracted by fitting a Hertzian contact model to the indentation part of the loading curve.

While AFM measurements are attractive due to their high spatial resolution and the possibility of creating height and stiffness maps[111], micro-indentation setups are better suited for microscale testing of the complex EPS network of biofilms. Indeed, soft materials like biofilms can present substantial adhesion between the tip and the sample, which can interfere with proper surface detection and measurement of elasticity.[112] Yet, adhesive forces can also be quantified upon tip retraction, which represents an interesting option for biofilm research.
The Johnson-Kendall-Roberts (JKR) model was introduced to account for adhesive contacts in contrast to purely elastic contact models (Hertz model).[113] Adhesion between the tip and a soft sample leads to the formation of a liquid meniscus upon indentation, as soft samples typically contain substantial amounts of fluid.[114] Yet, another competing mechanism, especially when indenting very compliant soft materials (< 100 kPa) is the surface tension generated between the sample and the tip.[115] Adhesion and capillarity do subsequently lead to high negative (adhesive) forces upon tip retraction and typically require large displacements above the initial surface contact.[115] To achieve meaningful measurement and interpretation of biofilm mechanical parameters, the method applied has to match the scale of interest and account for the EPS composition and structure.[56]

Today, most strategies to engineer the mechanical properties of living materials produced by bacteria involve genetic approaches from synthetic biology.[14,116] While increasing evidence shows how single bacteria respond to external stimuli on a cellular level, it remains largely unknown how external stimuli (i.e. the water content of the substrate) affect biofilm mechanical properties as a whole[27] and how this knowledge could be leveraged to design biofilm-based functional materials.

2.5 *E. coli* biofilm model system

E. coli's primary habitat is in the intestinal tract of warm-blooded mammals. Viscoelastic material properties could support *E. coli* biofilms to occupy their niche in the low flow environment of the colon.[117] Yet, pathogenic *E. coli* strains also reside on other host tissue such as in the urinary tract,[118] where they promote urinary tract infections (UTI'S) as shown through the expression of curli fibres in a mouse model.[119] The main EPS matrix components found in *E. coli* biofilms - amyloid curli and cellulose – can further promote the adhesion to organic and inorganic substances outside the host and help resist desiccation.[13] Attachment of *E.coli* bacteria to surfaces by their cellulosic EPS components might be especially relevant for their interaction with plants.[120] In that context, the exact role of *E.coli* EPS components is yet unclear, but the maximum EPS production observed under nutrient-limited conditions and ambient temperatures below 30 °C suggest the biological function of amyloid curli and cellulose supports the adhesion to plant surfaces.[121]

The production of amyloid curli fibres is essential for the structural integrity of *E. coli* biofilms.[122] Curli are non-branched protein amyloid fibres with an extensive β-sheet secondary structure made of two subunits.[123] The CsgB subunit is attached to the outer cell surface and CsgA subunits self-assemble into long fibres in the extracellular space.[25,123] The rigid β-sheet structure of CsgA subunits gives the protein low flexibility, i.e. a high storage modulus G'. Curli biogenesis is activated by the biofilm-master regulator of CsgD. CsgD further activates the adrA gene, which encodes an enzyme for the synthesis of the bacterial second messenger of cyclic di-GMP.[124] Cyclic-di-GMP is an intracellular chemical signal used by many bacterial species to regulate gene expression (e.g. inhibit flagella production) and promote the switch from planktonic growth to biofilm formation.[34] Besides curli biogenesis, CsgD coactivates the synthesis of extracellular polysaccharides in *E. coli*.[124]

A phosphoethanolamine (pEtN)-modified cellulose is the second most abundant ECM component in wild-type *E. coli* biofilms.[125] The pEtN-modification of homopolysaccharides of beta-1-4-linked glucose residues was recently shown to reside at every second residue.[125] PEtN-modified cellulose in *E. coli* biofilms is arranged in long and thick filaments (up to 15µm long) and sheets.[25] The self-assembly process of multiple pEtN-cellulose chains into long fibres remains elusive.[38] Yet, the pEtN-modification was suggested to assist the self-assembly process in contrast to unmodified cellulose chains.[38]

The *E. coli* strain AR3110 is a W3110 derivative with a restored capacity to produce phosphoethanolamine (pEtN)-modified cellulose.[63,125] Thus, AR3110 is a highly proficient biofilm-forming strain that produces both amyloid curli protein and pEtN-cellulose as major matrix components. Co-expression of both components yields a dense nanocomposite EPS architecture with combined properties of amyloid curli fibres described as 'mortar' embedding cells whereas pEtN-modified cellulose provides an elastic network.[38,126] Solid-state NMR enabled to estimate the relative ratio of amyloid curli to pEtN-modified cellulose in AR3110 biofilms around 3 : 1.[127]

While *E.coli* strain W3110 produces only amyloid curli fibres as its main matrix component, it was still shown to form thicker biofilms compared to AR3110. The *E.coli* strains AP329 and AP472 lack curli biogenesis and only produce pEtN-modified cellulose or unmodified cellulose respectively as their main matrix component.[63] The exclusive production of pEtN-modified cellulose by *E. coli* AP329 yields biofilms with a loose EPS network with large pores. Bacteria from mutant strains expressing only non-modified cellulose (AP472) form only shorter and thinner filaments.[125] Yet, to date a detailed mechanical analysis of this fibrous EPS network structure of amyloid curli and pEtN-cellulose fibres and the question of how both components contribute to the mechanical properties of *E. coli* biofilms are still to be explored.

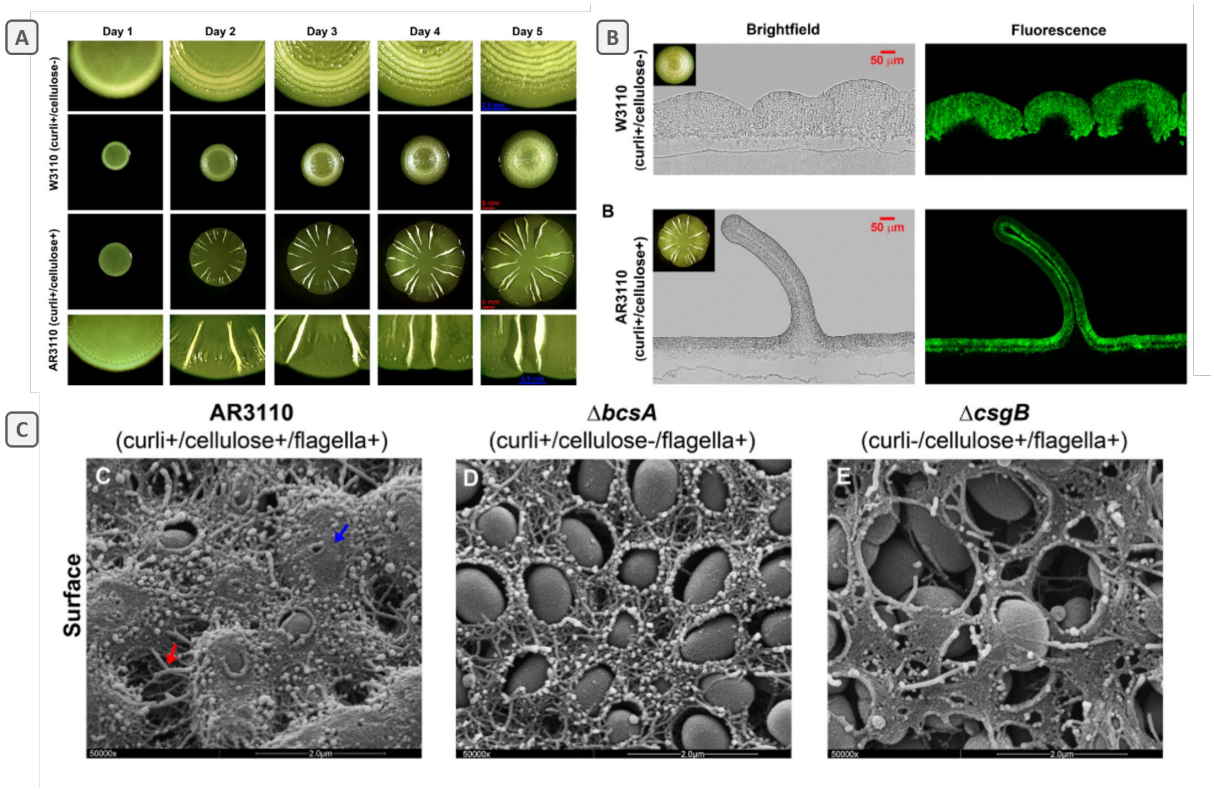

Fig. 7: *E. coli* biofilm development, cross-sectional distribution of EPS matrix components and EPS architecture at the biofilm surface. Time-lapse image series of biofilms of only amyloid curli producing *E. coli* strain (W3110) and of amyloid curli and pEtN-cellulose producing *E. coli* strain (AR3110) till 5 days of growth. (B) Brightfield and fluorescence images of cross-sections of *E.coli* strains mentioned above with amyloid curli stained by thioflavin S. (C) SEM images of the biofilm surface of an amyloid curli and pEtN-cellulose producing *E. coli* strain (AR3110), an *E.coli* strain (AR3110) deficient in cellulose production and an *E.coli* strain (AR3110) deficient in curli production (from left to right).[63] (reprinted with permission from the Journal of Bacteriology)

E. coli biofilms present a layered architecture, where matrix-producing *E. coli* bacteria encase themselves in a dense network of remarkable micro-scale architecture in the upper layer of E. coli AR3110 biofilms (closer to the biofilm-air interface). Bacteria in the bottom layer (closer to the nutritive substrate) do not produce matrix fibres but ensure cohesion through the entanglement of their flagella (Fig. 8).[63,125] Active cell growth becomes increasingly restricted to the outer edges and the bottom during *E. coli* biofilm development.[24] Indeed, cells in the upper layers of *E. coli* biofilms adopt stationary phase physiology and start amyloid curli and cellulose biogenesis, which leads to an asymmetric distribution of matrix components along the biofilm cross-section.[25] The upper layer is further subdivided into three zones of slightly different matrix composition and architecture (Fig. 8).[24]

At the top, close to the biofilm-air interface, the cells are embedded in a dense layer composed of a curli and cellulose nano-fibre composite (Fig. 8).[63] Right below, a network of vertically oriented pEtN-modified cellulose fibres transitions to a more loosely oriented network of cellulose fibres closer to the bottom (Fig. 8).[24] Note that regions closest to the substrate and in between and below delaminated buckles are not stained with thioflavin S (amyloid curli stain) and therefore only contains non-matrix producing cells (Fig. 8).

When EPS is artificially produced also in the bottom layer, it becomes more rigid.[26] The upper layer subsequently detaches and the biofilm can no longer retain its water content via capillary action and therefore dries out.[26] This hints at the crucial role the EPS matrix asymmetry has for the fitness of the whole biofilm.[26] Concluding these statements, a thick matrix-rich layer at the top of AR3110 biofilms was proposed to serve the long-term stability of the macrocolony by providing a protective and cohesive environment as well as to preserve the biofilm from desiccation by guaranteeing hydration of the whole biofilm.[26]

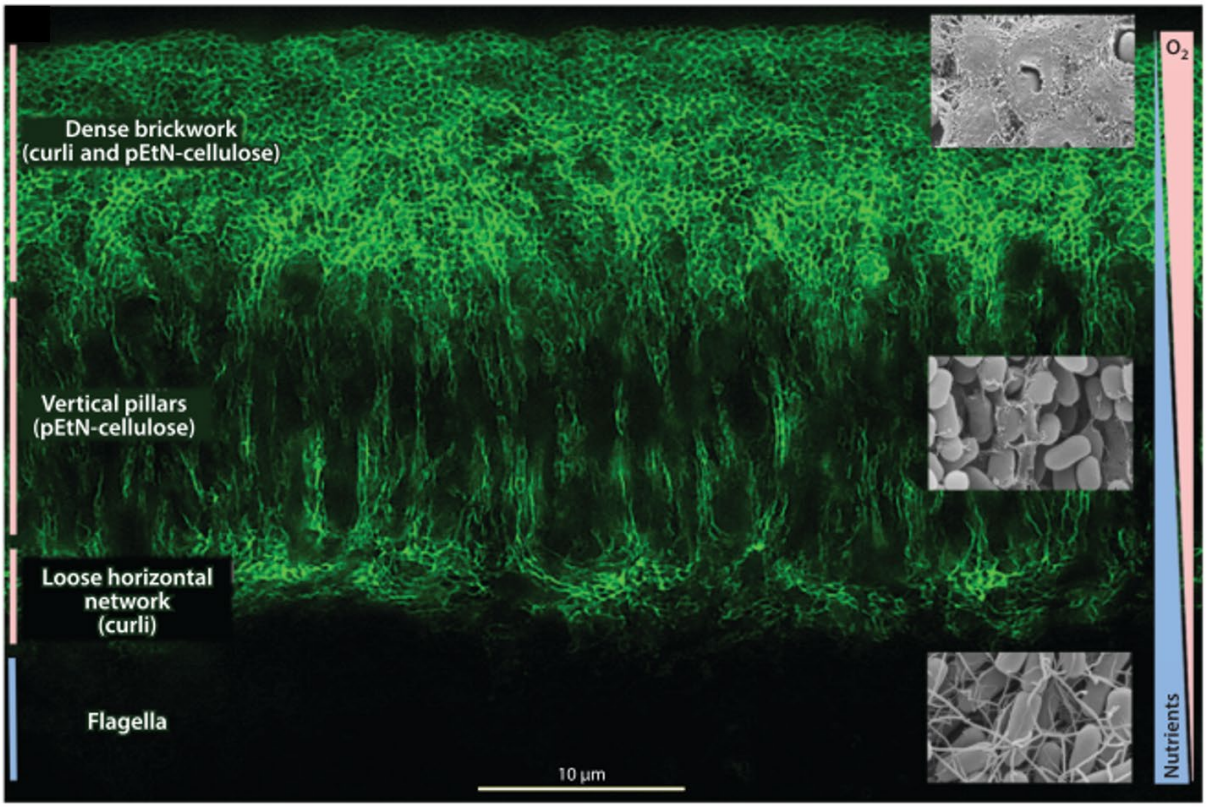

Fig. 8: Microscale architecture of *E. coli* AR3110 biofilms viewed as cross-sections with EPS matrix components stained with thioflavin S (green). At the top resides dense brickwork of amyloid curli and pEtN-modified cellulose closely embedding bacteria. Below extends a network of vertically aligned pillars of pEtN-modified cellulose which transitions to a loose horizontal network of curli fibres. At the bottom and closest to the nutrient-rich substrate

reside highly flagellated cells without significant amounts of EPS components (no fluorescence). (reprinted with permission from Annual Review of Microbiology)

At the solid-air interface, the combination of the two matrix fibres was suggested to confer AR3110 biofilms with tissue-like elasticity.[25] These properties are required to form a radial wrinkle pattern at the periphery, which transitions to high aspect ratio delaminated buckles (height/thickness reaching 10 to 30).[26,127] In contrast, *E. coli* macrocolony biofilms grown from the cellulose-deficient strain W3110 present a morphology with thick concentric wrinkles from centre to periphery and no morphological structures are observed for macro-colonies grown from curli-deficient strains (AP329, AP472).

The onset of biofilm morphogenesis is associated with signals from the environment, which include the presence of salts, oxidative stress, ethanol or the humidity of the agar.[63] As pronounced wrinkling of an initially flat biofilm dramatically increases its surface-to-volume ratio, it was proposed to support the function of oxygen uptake by increasing the exchange surface.[24] Furthermore, an increase in the surface area increases the evaporation of water, thereby constituting an active mechanism to drive nutrient-rich fluid into the biofilm.[81]

As described before, biofilm material properties are dependent on the composition and structure of its EPS network.[128] Rheological investigation of *E. coli* biofilm properties omits the contribution of the matrix architecture, which is damaged during sample preparation. Nevertheless, compared to wild-type *E. coli* biofilms, an altered expression of individual EPS matrix components reduces the storage modulus G' and the cohesive energy, as a consequence of impaired gel stability.[122] As *E. coli* biofilms are hydrophilic, they are expected to soften when water is added either from their environment (agar content 1.5 – 3 %) or by direct mixing with water during rheological experiments.[122]

The investigation of the mechanics of native *E. coli* EPS architectures at the nano- and microscale still poses a challenge. Utilizing the resolution of an AFM is one option to gain insight into structural and nano-mechanical aspects of *E. coli* cells and their EPS matrix components. In *E.coli* (AR3110) biofilms, producing amyloid curli and pEtN-modified cellulose, several subdomains of mechanical response are identified on the nanoscale.[129] At the biofilm surface local heterogeneities include three subdomains of I) fibre-coated bacteria, II) dense EPS layers and III) only bacteria.[129] EPS rigidity was estimated to be in the range of 1 to 3 kPa, whereas the rigidities of individual *E. coli* bacteria range from 1 to 10 MPa.[129] Local heterogeneities of the

EPS structure might support *E. coli* biofilms viscoelastic behaviour by incorporating different time scales of stress relaxation, which can be important in remodelling the EPS network during biofilm growth and morphogenesis.

Nonetheless, an in-depth understanding of *E. coli* biofilm mechanics at an intermediate scale between sub-cellular (AFM) and bulk properties (rheology) is still lacking. The combination of amyloid curli and pEtN-cellulose fibres in *E. coli* is suggested to provide increased elasticity to biofilms.[63] While amyloid curli fibres provide rigid elements to the EPS network and pEtN-cellulose fibres are suggested to provide more elasticity, a quantitative investigation of mechanical parameters of wild type *E. coli* (AR3110) and its EPS mutant strains is of high interest. Performing mechanical analysis on the microscale seems adequate to capture the influence of an intact EPS network of native *E. coli* biofilms.

3 MATERIALS AND METHODS

3.1 Bacteria culture and biofilm growth

All *E. coli* strains used within the scope of this thesis are derived from the strain W3110, which can synthesize amyloid curli protein but not pEtN-cellulose.[63] The *E. coli* strain AR3110 is a derivative from W3110 with a restored capacity to produce phosphoethanolamine (pEtN)-modified cellulose.[63] Thus, AR3110 is a highly proficient biofilm-forming strain that produces both amyloid curli protein and pEtN-cellulose as major matrix components. AP329 (csgBA::kan) is an AR3110 derivative strain that is deficient in the production of curli (i.e., it is a curli mutant; it produces only pEtN-cellulose).[63] This strain has a kanamycin resistance cassette associated with the mutation in the structural curli operon (csgBA). AP472 (bcsG::scar, csgBA::kan.) is an AR3110 derivative strain that is deficient in the production of curli and that produces cellulose, but in a non-modified form (i.e., without the pEtN-modification).[63] This strain has a kanamycin resistance cassette associated with the mutation in the structural curli operon (csgBA). AR198 (bcsA::scar csgB::cm) is as well an AR3110 derivative strain that is deficient in the production of both curli and pEtN-cellulose.[63] This strain has a chloramphenicol resistance cassette associated with the mutation in the curli structural gene csgB.

Large plates (15 mm diameter) were filled with 100mL of salt-free agar prepared with 1.8 w/v% of bacteriological grade agar-agar (Roth, #2266), supplemented with 1 w/v% tryptone (Roth, #8952) and 0.5 w/v% yeast extract (Roth, #2363), and kept in ambient conditions for 48 h. Bacteria single colonies were grown overnight at 37 °C after streaking a few mL of the bacteria stock solution on LB agar (Luria/Miller, Roth, #969). Each bacterial suspension was then prepared from a single colony grown overnight in LB liquid medium (Roth, #968) at 37 °C with shaking at 250 rpm. Finally, each plate was inoculated with arrays of 4 or 9 drops of 5 µL of bacterial suspension (OD_{600} ~ 5.0) (Table 1). After inoculation, the excess of water evaporated from the drops and bacteria-rich disks of comparable sizes of around 3-4 mm were visible on the surface.

Table 1: Overview table of biofilm growth conditions for chapter 4, 5 and 6 including *E. coli* strains used, agar concentration of substrate, supplemented nutrient concentration, number of inoculations per 15cm petri dish, the total time of biofilm growth, the added concentration of thioflavin S staining and concentration of added red fluorescent microparticles to initial inoculum.

Parameter	Chapter 4	Chapter 5	Chapter 6
E. coli strain	AR3110 AR31110-mcherry	AR3110	AR3110 W3110 AP329 AP472 AR198
Agar concentration (% w/v)	1.8	0.5 1.0 1.8 2.5	1.8
Nutrients concentration (% w/v)	1 tryptone + 0.5 yeast extract	1 tryptone + 0.5 yeast extract	1 tryptone + 0.5 yeast extract
Number of inoculations per plate	9	4 4 9 9	9
Time of biofilm growth	time-lapse imaging: 100h	4 days or for time-lapse imaging: 24h or 100h	4 days
Addition of thioflavin S to liquid salt-free agar	If needed 40 µg/mL	If needed 40 µg/mL	-
Addition of fluorescent microparticles to inoculum	0.004% v/v 3.5 µm red fluorescent particles 0.04% v/v 10µm fluorescent red particles	-	-

Chapter 4

In order to visualize the bacterial cells inside biofilms using fluorescence microscopy as done in chapter 4, the AR3110 strain was previously transformed with the plasmid pMP7604 (TetR) that carries the gene for the fluorescent protein mCherry.[130] This genetically modified *E. coli* AR3110 expressing mCherry fluorescent protein intracellularly was cultured for spatiotemporal fluorescence time-lapse imaging (Table 1). If EPS matrix staining was needed, thioflavin S

(Merck, T1892; 2 mg/mL in 70 % ethanol) was added to the liquid salt-free agar directly before pouring to reach a final concentration of 40 µg/mL. For particle tracking experiments, 0.004 % v/v (2.5-4.5 µm, Fluorescent Nile Red particles, 1 w/v%, Spherotech) or 0.04 % v/v (10µm, Fluospheres red, 3,6 x 10^6 microspheres/mL, Invitrogen) fluorescent polystyrene microspheres were added to the initial inoculum. Pure microsphere suspensions followed by bacteria cultures supplemented with microspheres were vortexed for 30 s before further use. For all time-lapse imaging experiments, biofilms were grown for 100 h at 28 °C in static conditions.

Chapter 5

E. coli AR3110 was used throughout the study reported in chapter 5.[63] Salt-free agar plates (15 mm diameter) were prepared with 0.5, 1.0, 1.8 or 2.5 w/v% of bacteriological grade agar-agar (Roth, #2266), supplemented with 1 w/v% tryptone (Roth, #8952) and 0.5 w/v% yeast extract (Roth, #2363) (Table 1). Each plate was inoculated with arrays of 4 or 9 drops of 5 µL of bacterial suspension (OD_{600} ~ 5.0). After evaporation of the excess water from the inoculum, the bacteria-rich disks left on the agar surface were of comparable sizes within each plate, ranging from 4 mm diameter for high agar content to 8 mm for low agar content. If matrix staining was needed, Thioflavin S (Merck, T1892; 2 mg/mL in 70 % ethanol) was added to the liquid salt-free agar directly before pouring to reach a final concentration of 40 µg/mL. Biofilms for live imaging were grown for 100 h at 28 °C in static conditions. Biofilms used for estimation of mass, water content and mechanical parameters were grown for 4 days in total (96 h).

Chapter 6

The *E. coli* strains AR3110, W3110, AP329, AP472 and AP198 that form biofilms with different EPS matrix compositions were used throughout the study presented in chapter 6 (Table 1, Fig. 9).[63] Salt-free agar plates (15 mm diameter) were prepared with 1.8 w/v% of bacteriological grade agar-agar (Roth, #2266), supplemented with 1 w/v% tryptone (Roth, #8952) and 0.5 w/v% yeast extract (Roth, #2363) (Table 1). The different bacterial suspensions were prepared from single bacterial colonies of the different strains and grown overnight in Luria-Bertani (LB) medium at 37 °C with shaking at 250 rpm. For the mixed-species biofilms, a 50:50 mixture of bacteria suspension of W3110:AP329 suspensions was prepared. Therefore, 50µl of each bacterial suspension was added to a 2ml Eppendorf vial, vortexed for the 30s and further used for inoculation. Each plate was inoculated with arrays of 9 drops of 5 µL of bacterial suspension (OD_{600} ~ 5.0) per mutant strain. After inoculation, the excess of water evaporated from the drops and left bacteria-rich disks of comparable sizes of 4 mm diameter. Biofilms were grown for 4 days at 28 °C in static conditions.

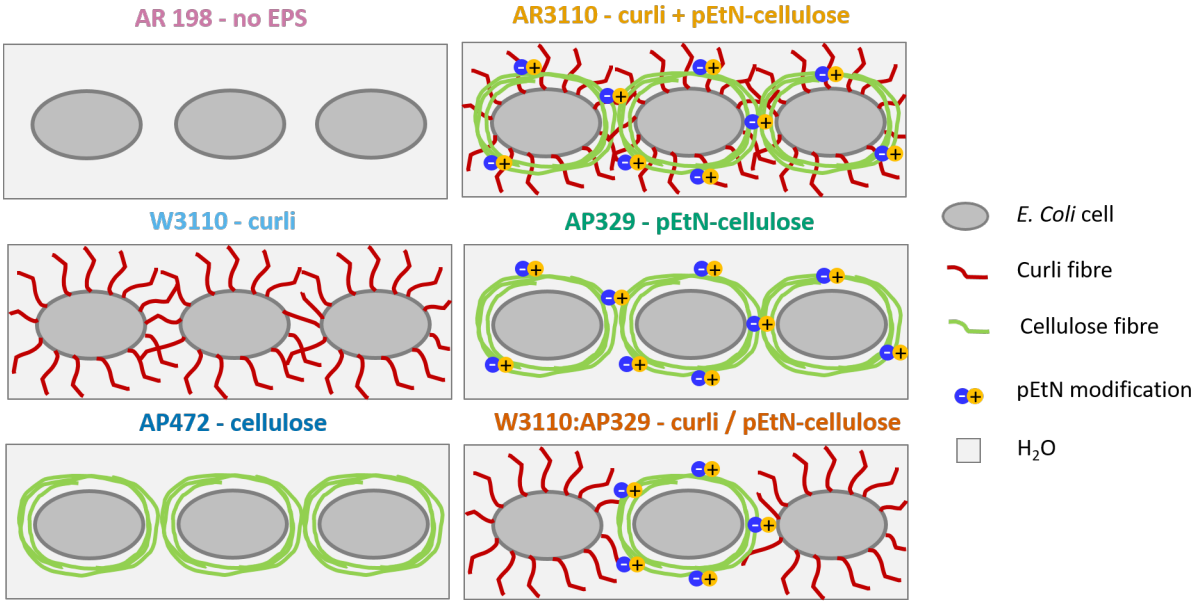

Fig. 9: Sketch of bacterial cells at the biofilm surface expressing different EPS components for all *E. coli* strains used within the scope of this thesis (AR198 – no EPS, AR3110 – curli and pEtN-cellulose, W3110 – curli, AP329 – pEtN-cellulose, AP472 – Cellulose, 50:50 mixture of W3110 and AP329 – curli / pEtN-cellulose).

3.2 Time-lapse imaging

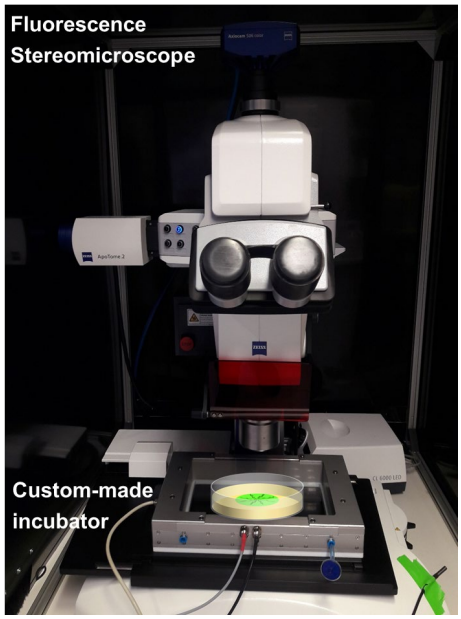

Fig. 10: Fluorescence stereomicroscope (Zeiss, Germany, AxioZoomV.16) with automated staged and installed custom-made on-stage incubator. At the top, we further see the camera used (Axiocam 506 color, Zeiss, Germany) and on the left side the Apotome.2 system, which improves z-stack resolution through structured illumination.

For time-lapse imaging experiments, biofilms were grown in a custom-made on-stage incubator installed on the motorized stage of an AxioZoomV.16 stereomicroscope (Zeiss, Germany, Fig. 10). To control the temperature a heating system was embedded in the frame of the on-stage incubator, which allows heating the conductive ITO (Indium Tin Oxide) top window. Slight local overheating was used to prevent condensation inside the chamber, which would impair the imaging of growing biofilms. The stereomicroscope was positioned in a dark box, to avoid interference with ambient light, especially for fluorescence time-lapse imaging. For fluorescence time-lapse imaging of mCherry fluorescent protein and thioflavins S a black sheet was placed below the petri dish to increase fluorescence yield, which prevents simultaneous brightfield imaging by transmitted light. Exceptions were made for fluorescence imaging of high fluorescence intensity microspheres, where brightfield imaging was carried out in parallel. To monitor biofilm growth over time, 3x3 and 2x2 tile regions were automatically imaged at 4 to 9 positions on a 15 cm petri dish over the course of 100 h of biofilm development with 1 h intervals. Temperature and relative humidity inside the on-stage incubator was controlled and set to 28 °C and > 90 % respectively by Multi Control (v2.2.4) software developed and installed by the workshop of the Max-Planck Institute of Colloids and Interfaces.

3.2.1 Brightfield time-lapse imaging and analysis

Chapter 5

After recording biofilm growth using brightfield illumination in transmission as in chapter 5, biofilm spreading area $A(t)$ and delaminated buckle area $A_{DB}(t)$ were analyzed automatically, using custom-written MATLAB codes (Matlab 9.7.0 R2019b, MathWorks, Natick, MA). In a first step, automated thresholding was applied to the intensity values of the pixels to segment the background (high grey values) from the flat biofilm (intermediate grey values) and the wrinkle areas (low grey values). As the image contrast increased due to biofilm growth, recognizing the biofilm from the background was possible from $t > 10$ h. For each condition, $A_i=1$ was defined at the time point, when all different samples grown in this condition could be detected, to have a common reference point for the calculation of the relative area increase $A(t)/A_i$. Onset times of biofilm spreading (later referred to as the transition from phase I to II) were defined as $A(t)/A_i > 1.05$. The transition time point from phase II to III was defined at the maximum of the areal spreading rate $1/A_i * dA/dt$ (Appendix 6). Finally, phase II was later split into phase IIa and IIb, after defining the onset of delamination as $A_{DB}(t)/A(t) > 0.005$.

3.2.2 Fluorescence time-lapse imaging and analysis

Confocal Laser Scanning Microscopy (CLSM) has been widely used to study 3D biofilm EPS architecture but does not provide the field of view nor depth of field necessary for the analysis of macrocolony biofilm development. Therefore, within the scope of this thesis, I use a time-lapse fluorescence stereo imaging approach, which allows a non-destructive spatiotemporal characterization of *E. coli* biofilm development.

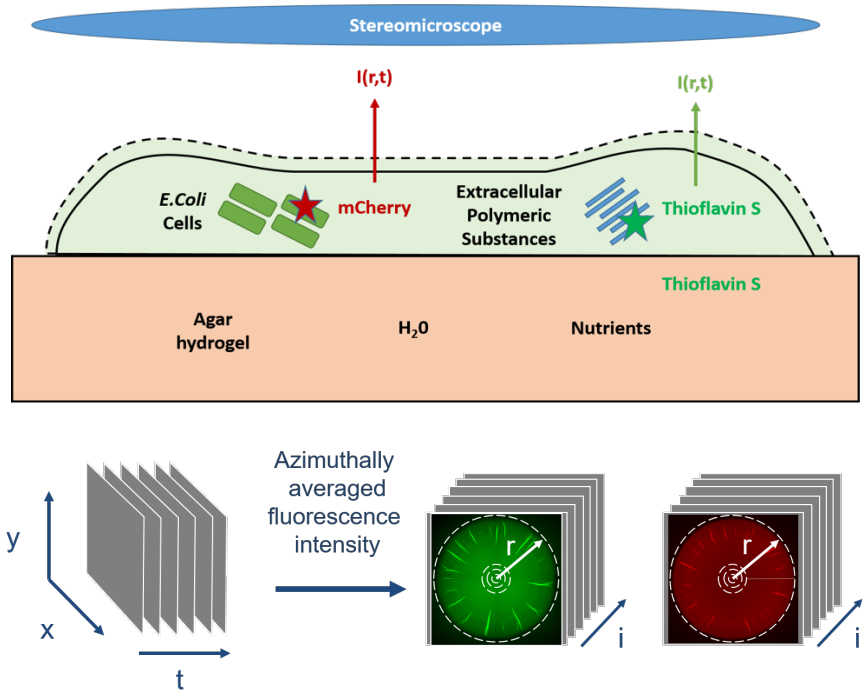

Fig. 11: Illustration of fluorescence time-lapse imaging (top) and analysis (bottom)**.** Time-lapse image series are recorded with a time step of 1 h to analyse the fluorescence intensities of thioflavin S staining amyloid curli and phosphoethanolamine-cellulose fibres and mCherry labelled bacteria (top), fluorescence intensities are azimuthally averaged over the radial distance from biofilm centre to the periphery for the whole period of biofilm growth.

Chapter 4

Fluorescence time-lapse imaging was mainly used in chapter 4. In this work, mCherry fluorescent protein (Ex: 540-590 nm, Em: BP 550-650 nm) was imaged with the Zeiss filter set 63 HE (Ex: BP 572/25 nm, Em: BP 629/62 nm) to locate the bacteria, 3.5 and 10 µm red fluorescent microspheres (Ex: 580 / Em: 605) were imaged with the Zeiss filter set 63 HE, and the fluorescent staining thioflavin S (Ex: 412 nm, Em: 490 nm – when bound to β-amyloid fibrils) was imaged using the Zeiss filter set 38 HE (Ex: BP 470/40 nm, Em: BP 525/50 nm). For each channel, 2x2 tile regions were automatically recorded at 9 positions on a 15 cm petri dish over the course of 100 h of biofilm development with 1 h intervals. The magnification used was 11.2x, which translates into a pixel size of 5 µm/pixel.

Before quantification, 2x2 tile regions were first stitched and shadowing was corrected from the raw data in the Zeiss software (Zen 2.6, blue edition, Zeiss). Background fluorescence for mCherry (150 a.u.) and thioflavin S (3000 a.u.) time-lapse series was subtracted manually with

Fiji software.[131] Background fluorescence was determined from intensity images at 10 h and subtracted from the whole image sequence to preserve low-intensity fluorescent signals present in early biofilm development. For visualization, fluorescence intensity image sequences were normalized by the maximum fluorescence intensity of the respective image sequence, specific “look up tables” (LUT) were used to enhance intensity differences in mCherry (red hot) and thioflavin S (green hot) image sequences, and images were further corrected for contrast and brightness in Fiji.

For the quantification of the radial distribution of fluorescence intensity in early-stage biofilm development, image sequences were cropped to square (around the last image at 30 h) and azimuthally averaged (100 bins along with the radius r) around the biofilm centre with custom-written MATLAB code. For the quantification of the azimuthal distribution along a thin annular region a circular ROI at a distance of r(azimuth) / R(biofilm) = 0.8 with a width of 100 µm was selected. Fig. 16D displays the azimuthal profile over an azimuthal angle φ = 45°. To calculate the average wavelength λ , peaks were counted (N) over an azimuthal angle φ = 90° at the different time points of 30h and 90h, and divided by the respective arc length of the outer radius of the ROI (s = $\frac{\pi R \varphi}{180°}$) following the formula.

$$\lambda = \frac{2N}{\pi R} \tag{1}$$

3.3 Single-particle imaging and tracking analysis

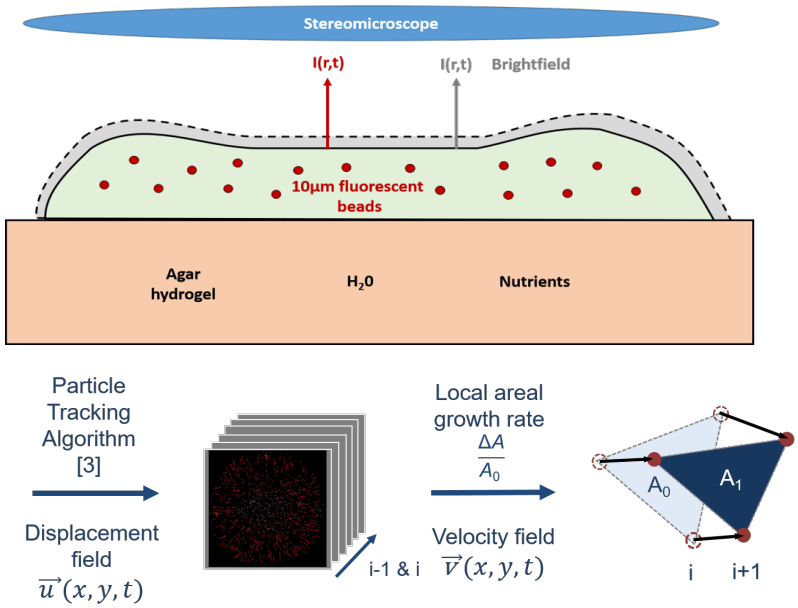

Fig. 12: Illustration of fluorescent single-particle time-lapse imaging (top) and analysis (bottom)**.** Time-lapse image series were recorded with a time step of 10min. or 1h to track the 2D projected positions of fluorescent particles inside the biofilm. (top) We use particle tracking methods like the TrackMate[132] plugin in Fiji software and a custom-written particle tracking and image velocimetry (PTV and PIV) algorithm. To extract 2D displacement fields two consecutive images of a time are cross-correlated. Subsequent calculation of discrete or interpolated velocity fields and estimation of local areal growth rates by Delaunay triangulation of particle positions in MATLAB. (bottom)

Chapter 4

For the analysis of the early stage of *E. coli* biofilm development performed in chapter 4, 3.5 µm fluorescent particles were embedded to the initial inoculum and tracked with the TrackMate plugin in Fiji software.[132] Square-shaped regions of interest (ROI: 300x300 pixel ~ 654x654 µm) were cropped from fluorescence raw image sequences (16-bit, grayscale) and converted to 8-bit grayscale image sequences. The sampled time period spans the time from 1.5h – 20h (90 – 1200 min., which represents 111 single images with time steps of 10 min.). Particle detection was performed at sub-pixel resolution using a Laplacian of Gaussian (LoG) detector with an estimated blob diameter set at 10 µm. The estimated blob diameter was set larger than 3.5 µm (i.e. the size of the bead) to account for the increase of their apparent diameter over the course of the experiment due to deflection in the vertical (z) direction. This effect could not be fully eliminated by using the auto-focus function of the stereomicroscope. Initial filtering by the

quality of detected particles was performed before utilizing the 'simple (Linear Assignment Problem) LAP tracker' tracking algorithm to construct particle trajectories (maximum linking distance: 20 µm, gap closing distance: 10 µm, maximum frame gap: 0). Constructed particle trajectories were consecutively filtered by the track duration so that only trajectories spanning the whole time period of 90 – 1200 min. (111 frames) are considered for further trajectory analysis. Particle positions, track identifier and frame number were exported to MATLAB (R2019b, The Mathworks Inc.) for plotting time colour-coded particle trajectories. The gradient of the x component of particle positions was calculated in MATLAB and further used for velocity analysis of particles at the periphery of the biofilm.

To further analyse particle trajectories over the course of 100 h of biofilm growth, particle tracking and image velocimetry methods were combined in a custom-written MATLAB code[51]. Before this, fluorescence intensity image series (.tif stacks) were first transformed to binary image series using an automated threshold. In order to avoid performing the calculations on the whole image and thereby spare computational time, a bounding box was created for each image separately to span the region containing the beads, with a margin of 10 pixels. Particle positions and displacements were then calculated in 2 steps: in the first step, global particle movements were determined for every image of the time series using particle image velocimetry (PIV) and in a second step, particles were tracked individually in smaller interrogation windows of size 64 x 64 pixels overlapping by 16 pixels, between time t and t+1 using particle tracking velocimetry (PTV). Furthermore, particles were filtered by size, radius, circularity, intensity and maximum displacement and duplicates due to window overlap were removed.

Particle trajectories were then plotted with Fiji and overlayed on brightfield images. As displacements happen over time steps of t = 1 h, they characterize the instantaneous velocity of particles. Discrete velocity vectors were overlayed to particle positions in MATLAB. Maximum velocities were plotted over the radial distance from the centre of the bounding box, which was revealed to be a good approximation for the biofilm centre, as tested for several image series. Further interpolation of particle positions and displacements yielded average maps of maximum velocity. These maps were split into their polar components and kymographs were created to show the distribution of radial and circumferential velocity during 100 h of biofilm development.

To achieve a spatiotemporal analysis of biofilm areal growth rates, the region covered with particles was meshed using a 2D Delaunay triangulation algorithm implemented in MATLAB. Particle positions (x- and y- coordinates) and their 2 nearest neighbours were considered as vertices to construct a triangle mesh over the whole particle point cloud of the first image of the sequence. The triangle mesh then evolved in time following the displacement of each vortex, i.e. following the trajectories of each particle previously tracked. For each frame of the image sequence (corresponding to a time t) and for each triangle i of the whole mesh, the positions of the triangle centre $(x,y)_{i,t}$ and their respective areas $A_{i,t}$ were calculated. To indicate if the biofilm region defined by a triangle is locally expanding or shrinking, the normalized area difference of each triangle between two frames was then derived as $(A_{i,t} - A_{i,t-1}) / A_{i,t}$ and the triangles of the mesh were coloured according to a red scale for expansion and blue scale for compression (shrinkage).

3.4 Gravimetric water content and biomass measurements

Chapter 5

The nominal water contents of the nutritive agar substrates used in chapter 5 were determined from the respective agar masses used during preparation as $W_{nominal} = m_{water} / (m_{water} + m_{agar} + m_{nutrients})$ * 100 (w/w)%. Their effective water contents were determined gravimetrically by weighing and drying 2x2 cm agar gel pieces at 60 °C for 20 h in an oven, and calculated from the wet and dry masses (m_{wet}, m_{dry}) as $W = (m_w - m_d) / m_w$ * 100 (w/w)%. Effective agar water contents were averaged from 4 independent measurements per condition. The difference in nominal and effective agar water contents results from nutrients being dissolved in the water phase, but still contributing to the dry mass measurements.

For biofilm weight and biofilm water content measurements, 7 individual biofilms per condition were scraped from the respective agar substrates after four days (~96 h) of growth using a cell scraper. Single biofilms were weighed in weighing boats and dried at 60 °C for 3 h. Wet and dry mass (m_w, m_d) were determined before and after drying. Gravimetric biofilm water contents were calculated as $W = (m_{wet} - m_{dry}) / m_{wet}$ * 100 (w/w)%.

Chapter 6

The water content of biofilms grown from different *E. coli* mutant strains in chapter 6 were measured following the same procedure as described in Chapter 5. Yet, a small but systematic error may have been introduced in the weighing of biofilms grown from amyloid curli deficient strains (AP329, AP472, AR198). Indeed, due to their less cohesive material properties and increased adhesiveness, minor parts of the biofilm material remained stuck to the Teflon head of the cell scraper and could therefore not be transferred to the weighing boats.

3.5 Cross-sectioning of biofilms

Chapter 5

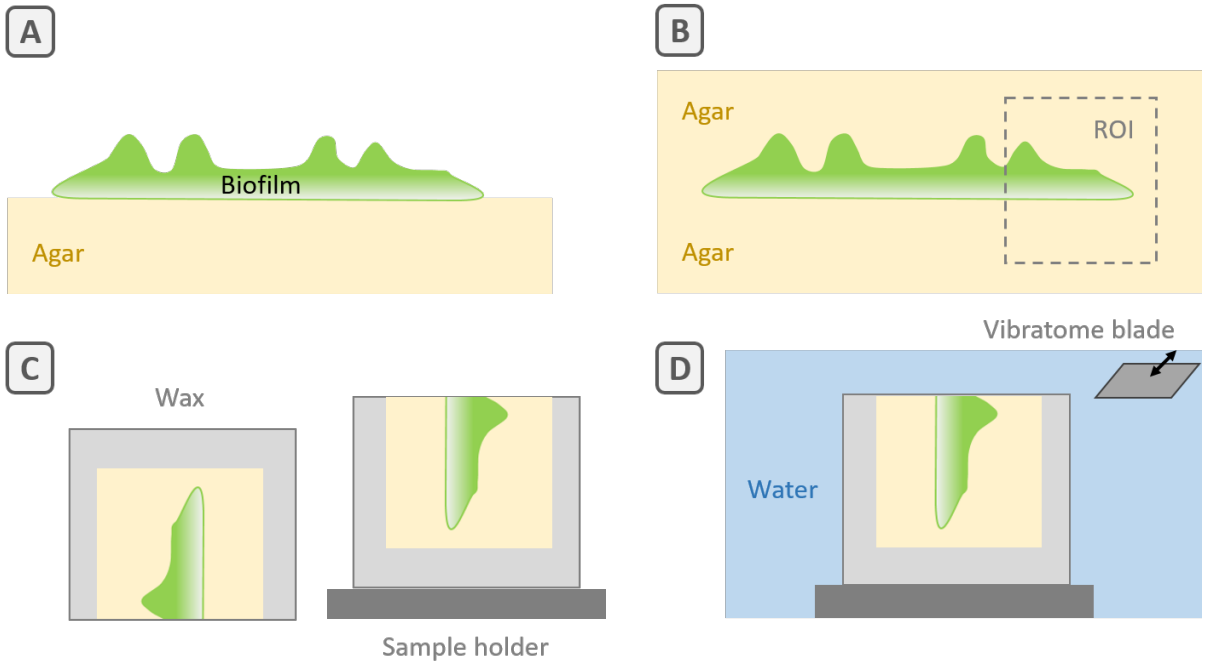

Fig. 13: Cross-sectioning protocol of biofilms. (A) Isolating of individual biofilms (B) Embedding of biofilms in liquid agar (1.8%) and cutting of region of interest (ROI) (C) Embedding of agar-biofilm-agar sandwich in wax and glueing to the sample holder (D) Performing slices with the VT1000 S vibratome vibrating blade with a lateral distance of 250 µm

The protocol established to obtain the cross-sections of living biofilms as reported in chapter 5 was adapted from a paraffin embedding technique for biofilms.[133] The biofilms of interest were isolated by trimming the underlying agar substrate into ~4x4 cm pieces. One piece was placed in a 6 cm diameter petri dish and slowly but continuously submerged with 50 °C hot liquid salt-

free agar (Fig. S6B, 1.8 %, without supplemented nutrients) while avoiding direct pouring on the biofilm and especially on the delaminated buckles. The resulting agar-biofilm-agar sandwiches were left to solidify for at least 20 minutes and then further trimmed. With a scalpel, sandwiches were cut to ~1x1 cm pieces involving the biofilm region of interest (periphery for delaminated buckles, Fig. S6B). These pieces were then placed in a muffin silicone mould (with the side involving the region of interest facing the bottom, Fig. S7C) and liquid paraffin wax at T > 60 °C was poured on top. After 30 minutes, the excess of solid paraffin was cut with a scalpel. Using liquid wax, the samples were then glued to the sample holders of the vibratome with the side of interest facing up (Fig. S7C). A drop of ultrapure water was added to the sample to prevent evaporation. Cuts were performed the same day with a VT1000 S vibratome (Leica, Germany). The thickness was adjusted to obtain 250 µm thick slices and cross-sections were collected with the help of a paint brush or directly floated onto a glass slide for fluorescence imaging.

3.6 Micro-indentation of biofilms and substrates

Biofilms were grown for four days and either measured directly after growth or stored in the fridge for less than 5 days. For storage at 4 °C, the petri dishes were sealed with parafilm to prevent evaporation. 2 - 4 biofilm samples were tested per condition. 8 measurements were performed in the central region of biofilms, which were still attached to the respective agar substrate. Average and standard deviations were calculated over all measurements from a respective condition. The lateral distance between two measurement points was at least 250µm in x or y directions to avoid the already deformed sample surface.

Chapter 5

Micro-indentation measurements were carried out using a TI 950 Triboindenter (Hysitron Inc., USA) to determine the load-displacement curves $p - \delta$. The instrument was calibrated in the air. Indentations were performed with a spherical diamond tip of radius $\mathrm{R} = 50\mu\mathrm{m}$ using an extended displacement stage (XZ-500), allowing a maximum displacement of 500 µm in the indentation direction. The measurements were done using “air-indent” mode and in a displacement control condition, which avoids pre-intending the surface prior to indentation.[134] The sample surface was approached from 300-400 µm above the surface and retracted to the

starting position while recording the measured force over the whole range. Loading rates ranged from 20 to 30 µm/s, which translates to loading and unloading times of 10 s. A Hertzian contact model was fit to the loading part of the curve (indentation depth range $\delta = 0 - 10\mu m$) to obtain the reduced Young's modulus E_r:[135]

$$p = \frac{4}{3} E_r R^{\frac{1}{2}} \delta^{\frac{3}{2}} \quad (2)$$

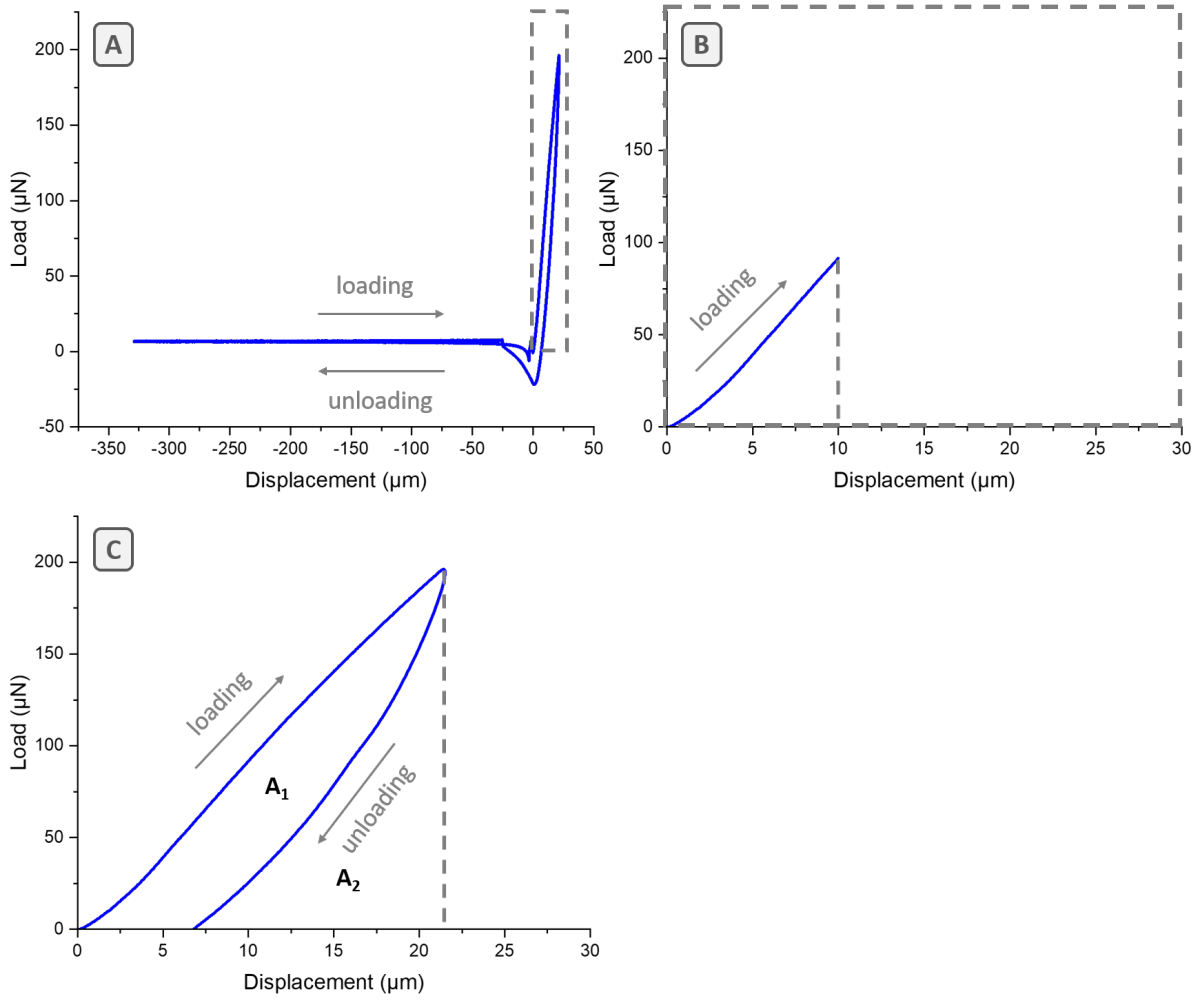

Fig. 14: (A) Representative load-displacement curve during loading and unloading *E. coli* AR3110 biofilm surface (1.8% agar). (B) Zoom in on part of the loading curves used for fitting a Hertzian contact model (displacements 0-10µm). (C) Indicated are the areas used for calculating the plasticity indices (A1, A2) from loading-unloading parts of the load-displacement curves.

Bare agar substrates with all concentrations were further prepared in duplicate and tested with the same conditions as biofilms and data were processed the same way as described above. Agar substrates were prepared two days before measurements according to our biofilm growth protocol. The plasticity index ψ is defined as ψ = A1 / (A1 + A2), where A1 describes the area

between the loading and unloading curves and A2 describes the area under the unloading curve (Fig. 14). As it was our aim to compare the measured plasticity indices, we only considered areas with positive force values. Yet, for the calculation of absolute plasticity values (or the total amount of dissipated energy), the area with negative forces (due to the work of adhesion) until zero displacements is reached should be considered as well.

Chapter 6

Wild-type (AR3110) and mutant biofilms were grown for four days and either measured directly after growth or stored in the fridge for less than 5 days. Instrumentation, measurements and deriving Young modulus values by fitting a Hertz contact model was performed analogous as described above. Loading rates ranged from 20 to 30 µm/s, which translates to loading and unloading times of 10s with a 10s holding period with constant displacement in between to estimate the load relaxation over time (Fig. 15D).

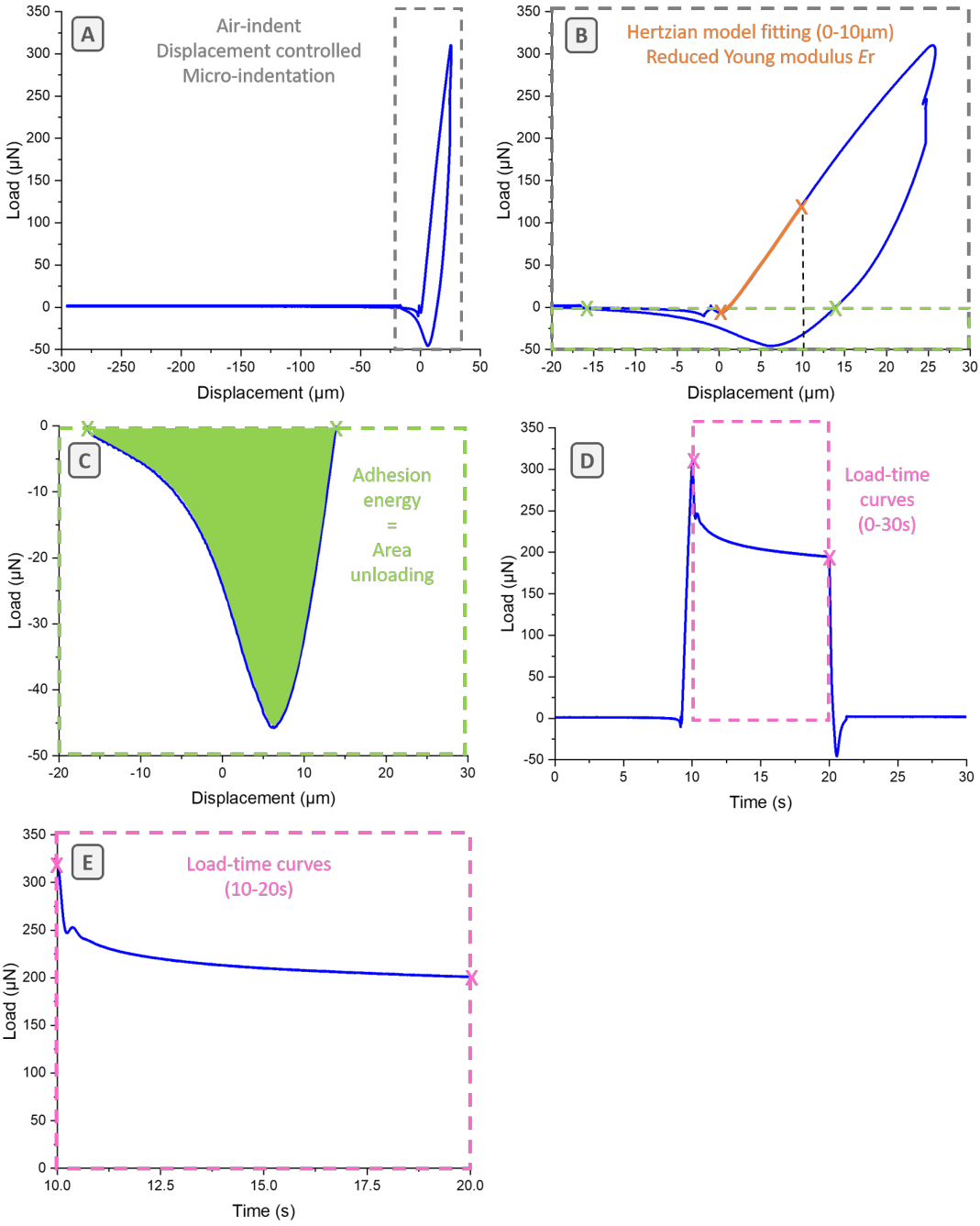

Fig. 15: Data analysis work flow of displacement controlled, air-indent micro-indentation experiments explained for a typical loading-unloading curve of indenting an *E. coli* AR3110 biofilm. (A) Full load-displacement curve for a loading-unloading cycle. (B) Zoom-in on a region of indentation indicated is a load-displacement region used for fitting a Hertzian model after surface contact is established (displacement set to 0-10µm, in orange). (C) Adhesion energy is calculated as the area under the unloading curve for load $p < 0$, (zoom-in on the green region in B). (D) Full load-time curve from the same indentation experiment on an *E. coli* AR3110 biofilm over the 30s. (E) Zoom-in on a load-time curve during holding period of 10s (pink in D), showing maximum load and minimum load after 10s (pink crosses).

A typical load-displacement curve recorded upon indenting an *E. coli* AR3110 biofilm is shown in Fig. 15A. Specifically, upon indenting *E. coli* AR3110 biofilms we observed a slightly increasing attractive (negative) force before approaching the biofilm surface, which might be the result of electrostatic interactions (Fig. 15A, B). After an initial instability a stable tip-surface contact was established (Fig. 15B – first orange cross). Displacements corresponding to the force minimum after the 'jump-in' of the tip were set to zero (surface contact established). Subsequently, a Hertzian contact model was fit to the loading part of the curve (displacement range of $\delta = 0 - 10\mu m$) to obtain the reduced Young's modulus E_r analogous as described above (Fig. 15B). Adhesion energies were calculated as the integrated area under the unloading curve for negative loads ($p < 0$, Fig. 15C). Yet, only load-displacement curves were analysed where the maximum load was reached in the displacement range of $\delta = 7 - 30\mu m$, to ensure comparable contact areas of tip and sample. This selection of single curves was necessary as the absolute depth of indentation cannot be controlled by running the nano-indenter in 'air-indent' mode. Average and standard deviations of adhesion energies were calculated only over the extracted load-displacement curves for each respective condition. A subset of 10 load-displacement curves from 2 samples (5 curves per sample) was analysed for visco-elastic load relaxation. Here, the corresponding load-time curves from 0-30s were extracted (Fig. 15D). Load-time curves during the holding period (10-20s, with constant displacement) were normalized by the maximum load (Fig. 15D, first pink cross = maximum load). Normalized load-time curves were aligned in Matlab and averaged normalized load–time curves were plotted for each condition. Yet, some load-time curves needed to be excluded especially for the more compliant AP329 and AP472 strains, as they reached their maximum load during tip instability short after the onset of the 10s holding period. Therefore the sample size varies from n = 5 – 10.

3.7 Statistical Methods

Chapter 6

Two-paired and two-sided t-tests were performed in Matlab to evaluate the statistical significance of two experimental groups for biofilm water content, rigidity and adhesion energy measurements. Due to small sample sizes, we also performed a non-parametric Mann-Whitney U-test which mostly gave equivalent results. We report significance levels from t-tests by p-values as statistically significant for $p < 0.05$ (*), $p < 0.005$ (**), $p < 0.0005$ (***) and $p < 0.00005$ (****) and no statistical significance as n.s.

4 NON-UNIFORM GROWTH AND MATRIX PRODUCTION DRIVE E.COLI BIOFILM MORPHOGENESIS

4.1 Results

In this chapter, we investigate how an initial non-uniform distribution of bacterial cells and EPS matrix gives rise to mechanical instabilities during *E. coli* biofilm development. We first use time-lapse fluorescence imaging to follow the spatiotemporal distribution of *E.coli* AR3110 bacterial cells expressing mCherry from plasmid and of the EPS matrix components stained with thioflavin S. We then add 3.5 µm fluorescent particles to the bacterial suspension and derive single-particle velocities to follow early, localized growth and confinement at the biofilm centre and periphery. Finally, we find that *E. coli* biofilm development follows four successive kinematic stages by tracking 10 µm fluorescent particles until 100 h of growth and discuss their influence on biofilm and substrate mechanics.

4.1.1 Non-uniform distributions of cells and EPS matrix precedes mechanical instabilities in *E. coli* biofilms

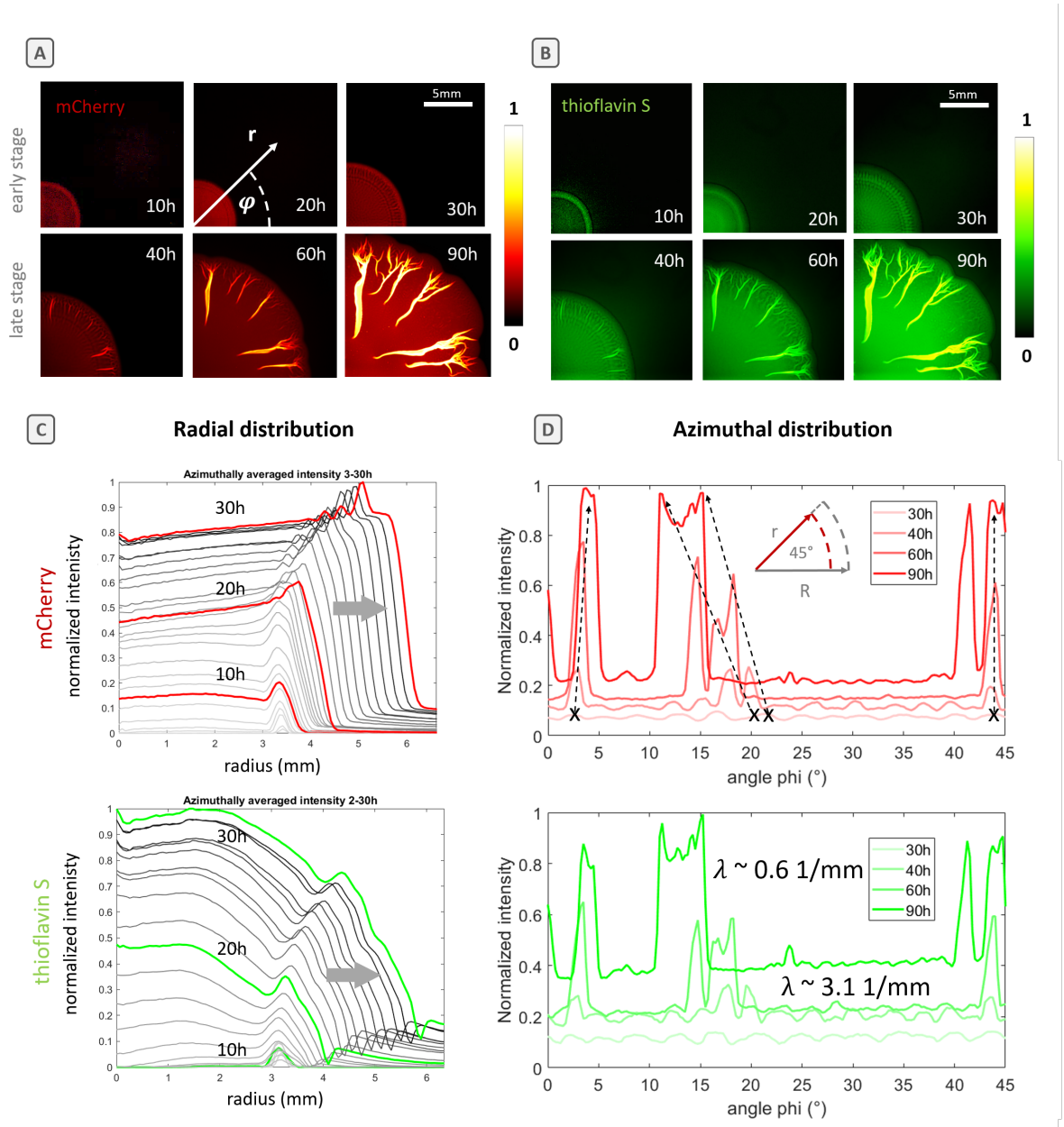

Fig. 16: Fluorescence time-lapse imaging of mCherry-protein being expressed from genetically modified *E. coli* AR3110 (red) and thioflavin S fluorophore (green) staining EPS matrix components of amyloid curli and pEtN-cellulose fibres during 100 h of biofilm development. (A) mCherry fluorescence intensity images of early (10, 20 and 30 h) and late-stage (40, 60, 90 h) biofilm development indicating the number of bacterial cells. (shown for one biofilm, representative of n = 9 biofilms) (B) thioflavin S fluorescence intensity images of early (10, 20 and 30 h) and late-stage (40, 60, 90 h) indicating the amount of EPS matrix components (shown for one biofilm, representative of n = 9 biofilms, scale bars are valid for all images of the respective image series). (C) Normalized (0 – 1) and azimuthally averaged radial distribution of mCherry and thioflavin S fluorescence intensity during early-stage biofilm development (0 – 30 h); grey arrows indicate the time period of maximum radial expansion

between 20 – 30 h. (D) Normalized azimuthal (0 – 45°) distribution of mCherry and thioflavin S fluorescence intensity in late-stage biofilm development (30 – 100 h) recorded at annular region with r/R = 0.8 (inset - top) with R being the biofilm outer radius; black crosses and arrow indicate initial wrinkles that transition to delaminated buckles (shown as increasing peak intensity of mCherry and thioflavin S, which represents a growth in vertical (z) direction).

An important feature of *E. coli* biofilm development is that cell differentiation leads to spatially heterogeneous distributions of bacterial cells and EPS matrix components.[23,63] As the stratified, cross-sectional *E. coli* biofilm architecture was studied in detail, here we focus on the spatiotemporal dynamic analysis of cell and EPS matrix densities during *E. coli* biofilm development. For this, we inoculated agar substrates (1.8 % agar, supplemented with thioflavin S) with 5 µL of *E. coli* AR3110-mCherry cell suspensions (~2.5 x 10^6 cells/µL) and monitored biofilm growth by time-lapse fluorescence imaging (Fig. 16A). The onset of wrinkling in *E.coli* AR3110 biofilm cultured on 1.8% agar appears approximately at 30 h. Therefore we proceeded with analysing the early stage of E.coli biofilm development from 0 – 30 h and the late stage of *E. coli* biofilm development from 30 – 100 h separately.[136] Please note that fluorescence intensity differences, such as periodic patterns at the periphery, result from different surface densities of bacteria (and matrix respectively) on the projected 2D image and are not attributed to structures inside the biofilm.

Spatiotemporal non-uniform distribution of bacterial cells and EPS matrix components characterize the early-stage biofilm development (Fig. 16B). At 10 h after inoculation, we observe an annular region of approximately 500 µm width with high mCherry intensity at the edge of a growing biofilm. EPS matrix components are co-localized at this annular region of increased cell density at 10 h of *E. coli* biofilm development (Fig. 16B – 10 h). Higher cell densities at this annular region are sustained till 30 h, i.e. amount of cells close to the edge, even though biofilm lateral spreading starts at around 20 h. From 20 h onward most EPS matrix components accumulate at the biofilm central region (Fig. 16C, Appendix 1 and Appendix 2). EPS matrix production in the biofilm interior continues until 30 h with a doubling of normalized thioflavin S intensity from 0.5 to 1, suggesting a high rate of EPS matrix production at this central and developmentally oldest region of the biofilm. The emergence of periodic circumferential patterns (along φ-axis) at the periphery in both mCherry and thioflavin S

intensities at 30 h clarifies the onset of a mechanical instability at this annular region (i.e. circumferential wrinkling) (Fig. 16A, B and D – 30 h).

Consistent with a transition of mechanical instabilities due to continuous growth at 40 h biofilm single surface wrinkles transition to delaminated-buckles with fluorescence intensity maxima larger than the ones of wrinkles at 30 h (Fig. 16A, B and D – 40 h). This transition of mechanical instabilities from periodic circumferential wrinkling to circumferential delaminations might reduce the overall surface energy by promoting the verticalization of single high-aspect-ratio buckles. Once delaminated buckles are formed, they further verticalize at the expense of neighboring wrinkles (Fig. 16D – 60h). The flattening of initially formed wrinkles between delaminated buckles is indicated by a flattening of the average azimuthal intensity between two delaminated buckles (black crosses and arrows) at 60 and 90h visible in both the mCherry and thioflavin S intensity images (Fig. 16D).

Early biofilm development is characterized by a lag phase where bacteria from a liquid culture adapt to the biofilm lifestyle at a solid-air interface (Fig. 16C, mCherry 1 – 5h).[75] Consequently, bacteria start to divide and proliferate and the density of bacteria increases (Fig. 16C, 5 – 10h). This increase in bacterial density is observed to mainly translate to an increase in biofilm thickness in the first 10h, while the biofilm as a whole remains confined to the substrate inside the circular boundary of the initial inoculum. When cell densities reach a critical value EPS matrix production is triggered and leads to further crowding of the extracellular space (Fig. 16C, thioflavin S, 10 – 20h).

4.1.2 Confinement of bacteria micro-environment during early-stage biofilm growth

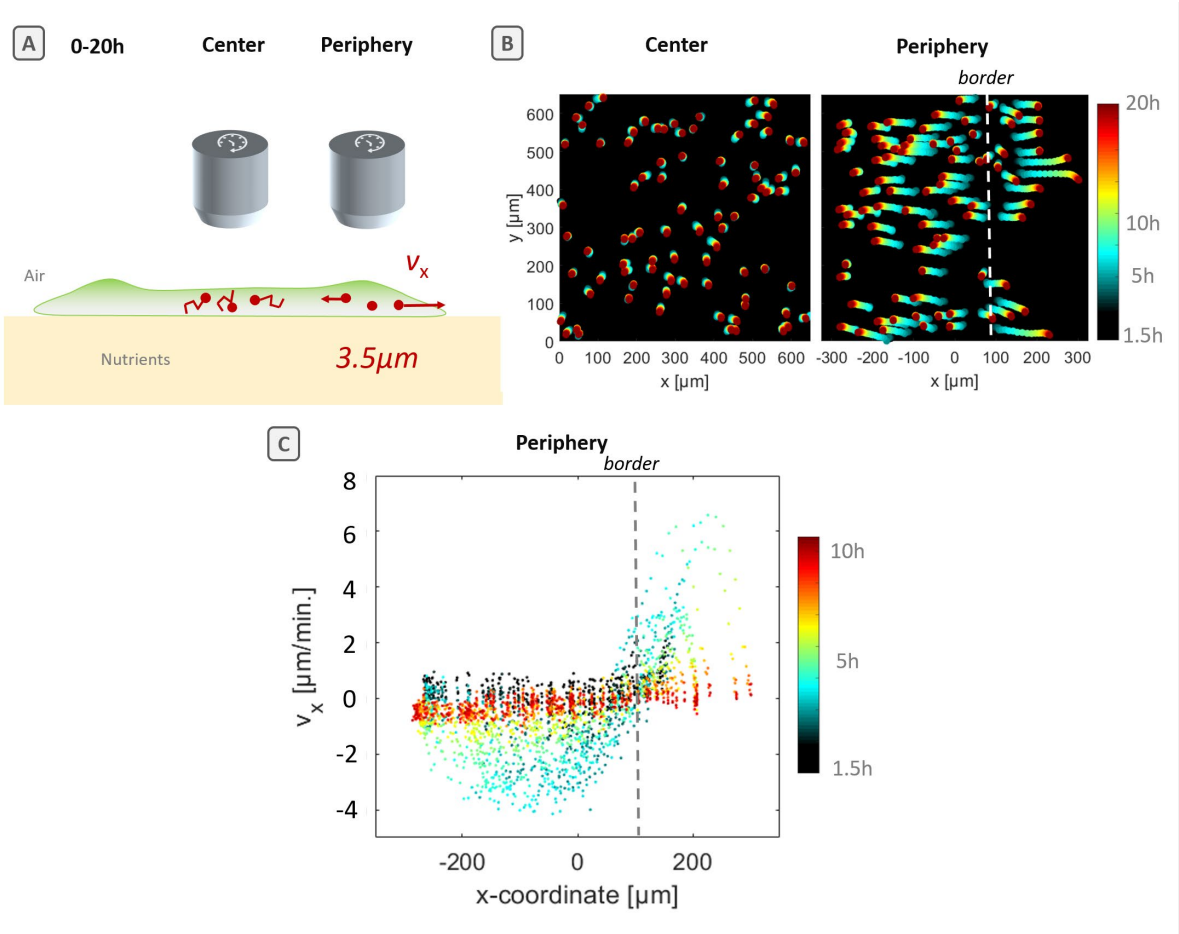

Fig. 17: Confinement of bacteria local micro-environment. (A) Sketch of the experimental setup, showing the random movement of 3.5 µm particles in the biofilm centre in opposition to a directed spreading at the biofilm edge during early-stage biofilm development (here only considered for 1.5 – 20 h, before overall surface expansion sets on). (B) Representative time-colour coded plots of particle trajectories at the biofilm centre and periphery, from a region of interest of 650 x 650 µm. (C) Time colour-coded spreading rates v_x of all single particles present in (B) at the biofilm periphery at 1.5 – 10 h of biofilm growth.

To investigate the initial crowding due to cell proliferation and matrix production we use single-particle tracking of 3.5 µm fluorescent particles. We derived particle trajectories with Trackmate[132] (a Fiji plugin) in the biofilm centre and periphery to compare how small, bacteria-sized particles experience their increasingly crowded local environment. Our biofilm growth protocol starts with a non-uniform distribution of cell densities (i.e. higher cell density at an annular periphery in comparison to the biofilm centre, (Fig. 16A)), which results from the coffee-ring effect when the initial bacteria culture droplet evaporates.[137]

Analogous to bacterial cells distributions, we observe a higher density of 3.5 µm fluorescent particles at the biofilm annular periphery compared to the biofilm centre. Following 3.5 µm particle trajectories from 1.5 to 20 h, we find more confined trajectories in the biofilm centre, where particles undergo random directional movement due to cell proliferation. Whereas at the biofilm annular periphery particles undergo a directed movement even before 5 h after inoculation (Fig. 17B). Even though particles at the annular periphery undergo substantial displacements around 5 h, they become confined in the period until 10 h (Fig. 17C). Confinement is also observed for particles in the biofilm centre in this period (10 – 20h) which correlates with the onset of matrix production in this region (Fig. 17B).

Particles at the periphery initially follow the multi-cellular migration outward to the free agar surface but also inward towards the biofilm centre (Fig. 17C, 1 – 5 h). Yet, some particles in the border region remain almost confined during the entire early-stage of biofilm growth, whereas others at the edge of the annular region become highly accelerated when collective cell migration propagates towards the free agar surface.

However, the onset of collective migration and confinement at the biofilm edge becomes more pronounced when looking at the v_x component of particles. Particles outside the border region follow a slow migration movement and become accelerated at the time 1.5 – 5h until they reach a maximum velocity of about 6 µm/min (Fig. 17C). Subsequently, particles undergo a deceleration, the velocity v_x ceases and particles become confined (Fig. 17C). Particles inside the border region start following a migratory movement towards the biofilm centre with a maximum velocity v_x of – 4 µm/min, which is transmitted to neighbouring areas to an extent of approximately 300µm from the border region. This initial inward migration is directed to an already colonized surface, which could serve as an additional explanation to local confinement by an increase in cell density and onset of matrix production.

Taken together, we need to distinguish the confinement of the bacteria micro-environment at the biofilm centre and periphery at early-stage biofilm development for its possible impact on *E. coli* biofilm morphogenesis. Yet, the entrapment of small micron-sized particles during early-stage biofilm development, most probably caused by local confinement due to increased cell density and crowding of the extracellular space with EPS matrix components, enables us to follow the growth and morphogenesis also during the later stages of *E. coli* biofilm development.

4.1.3 *E. coli* biofilms follow four kinematic stages during morphogenesis

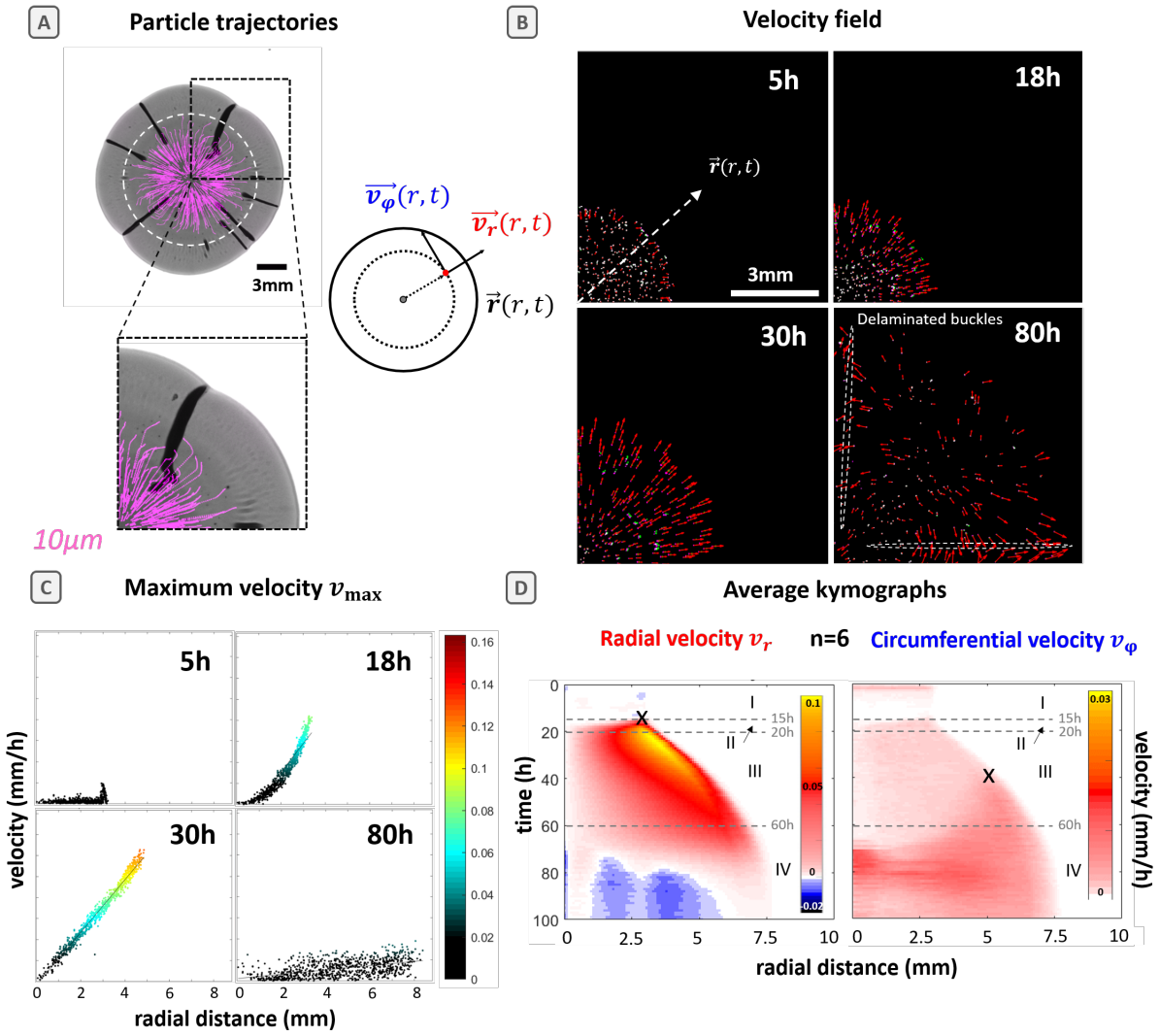

Fig. 18: Single particle-tracking velocimetry of *E. coli* biofilm development (100 h of growth). (A) Brightfield, transmitted image of mature *E. coli* biofilm with 10 μm fluorescent particle trajectories overlayed (pink); zoom-in showing substantial circumferential deflection of particle trajectories towards a growing delaminated buckle (left), visualization of radial and circumferential components of particle velocity vector (right). (B) Discrete velocity vectors at 5, 18, 30, 80 h of *E. coli* biofilm development overlayed over binary beads displacement images. (C) Discrete radial distribution of all single-particle maximum velocities at 5, 18, 30 and 8 0h of *E.coli* biofilm development. (D) Averaged radial and circumferential velocity kymographs extracted from interpolated velocity maps (for n = 6 biofilms).

The spatiotemporal non-uniform distribution and production of EPS matrix components was shown to be associated with a succession of several kinematic stages of radial expansion during *V. cholera* and *B. subtilis* biofilm growth.[19,36] Here, we investigate which regimes of physical

expansion exist during *E. coli* biofilm development by embedding 10 µm fluorescent particles to the initial inoculum of bacteria suspension (0.04 % v/v, approx. 600 – 800 particles). With fluorescence time-lapse imaging we recorded particle positions at 1 h intervals and derive particle trajectories as representatively shown in Fig. 18A. Custom particle tracking velocimetry (PTV) algorithm written in MATLAB enables the calculation of discrete particle velocities at every consecutive time step (Fig. 18B). As the length of each velocity vector mirrors its absolute value, we can extract a maximum velocity for each individual particle. As biofilm growth is radially symmetric and wrinkles and delaminated buckles emerge in a circumferential direction we further construct velocity kymographs of its polar components v_{r} and v_{φ} to track the displacement of biomass during *E. coli* biofilm morphogenesis.

We find that *E. coli* biofilm development follows four kinematic stages, which we characterize by individual velocity profiles. The first stage (0-15 h) in *E. coli* biofilm development is characterized by a localized peak in maximum velocity at the annular region at about 5 h (Fig. 18C). The radial position of this peak corresponds to the annular region of higher mCherry intensity at the periphery of the initial inoculum (r ~ 3-4 mm) (compare Fig. 16A). Comparing with the direction of the velocity vectors in Fig. 3B, we see that this maximum velocity v_{max} of 0.02 mm/h is directed towards the center of the growing biofilm, which corresponds to a negative radial velocity v_{r}. This is exactly what we observe in Fig. 18D (I) with the small light blue area on the 5 h horizontal line in the average kymograph of the radial velocity v_{r}. In the transitional stage between 6-12 h the particles on the outer annulus become immobilized again with a velocity below 0.01 mm/h.

Taken together with the results from the previous section, 10µm particles undergo a similar confinement as 3.5 µm particles. After an initial acceleration from the annular region of high cell and matrix density, particles become confined by the onset of EPS matrix production. Yet with 10 µm particles we cannot track the initial outward spreading of *E. coli* biofilms, as they might be more confined towards the center during coffee-ring like evaporation.[138]

The second kinematic stage (15-20 h) of *E. coli* biofilm development is characterized by a non-linear outward radial acceleration of biomass starting from the annular periphery (Fig. 18C – 18 h). At 15h we observe a sharp increase in radial velocity of the beads at the annular region (r ~ 3-4 mm) with a maximum velocity v_{max} of 0.025 mm/h (Fig. 18C – x). At 18 h the maximal velocity v_{max} has more than tripled to 0.08 mm/h (Fig. 18C). This rapid increase in maximal

velocity is mostly attributed to an outward radial expansion perpendicular to the edge (Fig. 18D). Furthermore this increase in maximal velocity $v_{\max}$ is accompanied by a mobilization of biomass away from the edge (r > 1 mm) at 18 h leading to the non-linear distribution of maximum velocities (Fig. 18C).

The third kinematic stage (20-60 h) of *E. coli* biofilm development is represented by a linear radial velocity profile from biofilm centre to periphery indicating an isotropic and uniform expansion. By fitting a linear regression model to the maximum velocity $v_{\max}$ over radius *r* we define the onset of linear velocity profiles for $R^2 > 0.9$ at 20 h (Appendix 3). At around 23 h a global maximum of radial velocity (i.e. outward expansion) is reached. Note that $v_{\max}$ is still dominated by its radial velocity component v_r ($v_r >> v_\varphi$) until around 60 h (Fig. 18D). Even though the formation of larger delaminated buckles is detected in the kymographs at 40 h (Fig. 18D – x-mark on kymograph of v_φ) radial outward expansion in the biofilm centre continues until 60 h, but subsequently slows down. That is also the time when particles become increasingly deflected (perpendicular to r-axis) towards the nearest delaminated buckle, which grows in vertical direction. Note that particles converging at the buckles leave the focal plane in z-direction and are no longer detected.

The forth kinematic stage (60-100 h) of *E. coli* biofilm development is characterized by the transition from radially to circumferentially dominated growth rates indiciated by $v_\varphi \sim v_r$ in the biofilm centre. In late stage *E. coli* biofilm development delaminated buckles progressivly penetrate towards the biofilm central region. At 80 h the radial outward expansion recedes (approaches 0 mm/h) and the maximum velocity is dominated by circumferential movement around the delaminated regions (Fig. 18D – indicated regions). Particle velocities in between delaminated buckles reach zero maximum velocity $v_{\max}$, while particles maximum velocities increase towards delaminated buckles (Fig. 18B).

4.1.4 Mechanics of the biofilm and substrate

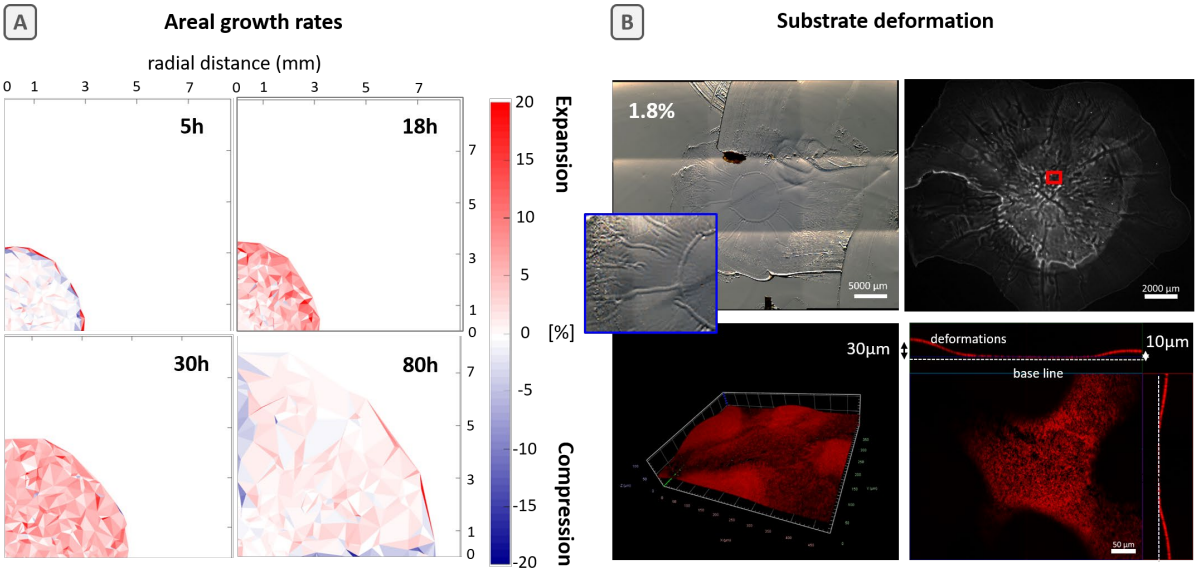

Fig. 19: Biofilm and substrate mechanics. (A) Areal growth rates estimated from particle positions (x- and y-coordinates) by Delaunay triangulation and colour-coded plotting of the normalized change of triangular area ((A_i – A_{i-1}) / A_{i-1}) from time t_{i-1} to time t_i for every single triangle of the mesh and all frames i (red = expansion, blue = compression), shown at 5, 18, 30 and 80 h. (B) Apparent substrate deformation upon scraping an *E. coli* AR3110 biofilm from a 1.8 % agar substrate. (top left), fluorescence imaging of agar substrate surface with the addition of 1:10 diluted 1 µm red fluorescent particle solution. (top right, red square indicates the region for 3D imaging), 3D fluorescence apotome image z-stack of 1µm red fluorescent particles, showing deformation of agar substrate. (bottom left), orthoview of z-stack showing the base plane in x-y (valley – fluorescent, deformation – non-fluorescent) and extent of substrate deformation in x-z and x-z view to range between 10 – 30 µm at the biofilm centre.

To access biofilm mechanics we measured areal growth rates derived from Delaunay triangulation of fluorescent particle positions. Therefore, a triangle meshes is evolved over the sampled biofilm area constructed from displaced particle positions at consecutive time steps. By normalizing the difference of each triangular area i at time t+1 and time t with their initial area at time t we can infer a local areal growth rate. If particles are locally diverging the area of a constructed triangle is increasing during consecutive time steps. Therefore, the biofilm is expected to locally expand in this region. If particles are locally converging, the triangle area will decrease at consecutive time steps. Therefore, the biofilm is expected to become locally compressed in such a region.

Appling this to the different kinematic growth phases studied in the previous chapter, we observe a compression on the annular region in the first stage of *E. coli* biofilm development. At 5 h localized compression is detected at the annular region as particles become displaced towards the biofilm centre (Fig. 19A – 5 h). During the second kinematic stage, characterized by non-linear velocity profiles, areal growth rates are larger towards the biofilm periphery indicating non-homogenous growth (Fig. 19A – 20 h). When biofilms enter the linear velocity region from 20 – 60 h, areal growth rates are more homogenous across the biofilm surface (Fig. 19A – 30 h). In the last kinematic stage of *E. coli* biofilm development, areal growth rates between delaminated regions cease such as maximum velocities slow down, whereas the converging of particles around delaminated buckles indicate strong localized compressive strains down to – 15 % (Fig. 19A – 80 h). However, estimating areal growth rates by Delaunay triangulation only provides approximate information on the biofilm growth mechanics. Due to the adhesion and friction of biofilm and substrate, it is expected that the estimated areal growth rates of the biofilm also influences the deformation of the substrate.

Following the observation that *E. coli* AR3110 biofilms leave an imprint on soft 1.8 % agar substrates after scraping them from the surface (Fig. 19B – top left). Especially, the areas below delaminated buckles show persistent deformations. Therefore, we further tried to estimate the extent of deformation in the vertical direction. By adding a concentrated solution of 1 µm fluorescent particles and 3D fluorescence imaging we could derive the topography of these substrate deformations (Fig. 19B – top right, bottom left). The ortho-view of the z-stack of 3D fluorescence images shows the presence of valleys and hills on the substrates with vertical deformations of 10 to 30 µm (Fig. 19B – bottom right). These deformations could result from the growth periods when delaminated buckles are formed. Fluorescent particles are diverging towards delaminated buckles during late-stage *E. coli* biofilm development and strong compressive strains are suggested from estimating areal growth rates in these regions. This might lead to substantial deformations of the substrate and points towards the coupled role of biofilm and substrate mechanics.

4.2 Discussion

Previous studies of biofilm development indicate the important connection between biological processes such as cell division and matrix production that give rise to non-uniform biofilm growth. Here, I explore in a spatiotemporal manner how a non-uniform distribution of cells and EPS gives rise to *E. coli* biofilm morphogenesis. For the relevant biological processes, we focus less on the spatiotemporal distribution of cell differentiation from motile to matrix-producing cells but more on the integrated densities of cells and EPS matrix during biomass accumulation and the resulting local confinement and global growth rates with the aim to quantify them. In detail, I find similarities of the spatiotemporal development of *E. coli* biofilms with that of *B. subtilis* and *V. cholera*.[20,36] Our findings strengthen the hypothesis that a non-uniform distribution of cell and matrix production in early-stage biofilm development favours non-uniform biofilm growth (i.e. expansion over a substrate), which in turn is expected to promote the emergence of mechanical instabilities at an annular region of a growing *E. coli* biofilms.

Non-uniform cell densities, due to the coffee-ring effect of the initial inoculum, are preserved at later stages of *E. coli* biofilm development (Appendix 1). Regions of higher cell density at the biofilm periphery are co-localized with regions of early matrix production, which are sustained to later stages of *E. coli* biofilm development (Fig. 16C, D and Appendix 2). Internal mechanical stresses are suggested to accumulate much earlier at this annular region at the biofilm periphery than in the biofilm interior.

Such annular accumulation of EPS matrix components might therefore serve as a template for the emergence of mechanical instabilities in this peripheral region, somewhat analogous to differential growth of plant leaves.[139] This finding contrasts with a mechanical instability model proposed by Fei and co-workers, where wrinkles first appear either in the peripheral region and propagate inward (soft substrate/ low friction) or central region propagating outwards (stiff substrate/ high friction).[20] Even when changing agar concentrations from 0.5 % to 2.5 % I only observed wrinkle initiation at the periphery and propagation inward (Appendix 4).

After an initial lag phase (~ 5 h), cell proliferation mainly translates to an increase in biofilm thickness, yet lacking substantial outward spreading of the whole biofilms (Fig. 16C, 0 – 10 h). Only after matrix production is triggered in the biofilm centre (Fig. 16D, 10 – 20 h), biofilm spreading over a nutritive agar surface initiates (Appendix 1). This correlation of the onset of matrix production, which precedes overall biofilm spreading, suggests osmotically swelling of

matrix-rich layers to contribute to overall biofilm expansion in early-stage *E.coli* biofilm development.[41] Small bacteria-sized particles become confined at 10 h at the biofilm periphery, which further suggests an increased crowding of the extracellular space due to EPS matrix production. Such extracellular crowding with EPS matrix in the upper layers of *E. coli* biofilms is expected to confer this layer with cohesive material properties.

In the later stages of biofilm development, nutrient depletion in the central region and localization of biomass accumulation to the periphery were proposed to drive biofilm morphogenesis.[20,36] For *E. coli* biofilms we find extended linear velocity profiles of outward expansion (Fig. 18C; 20 – 60 h). This finding contradicts the theory of chemo-mechanical models where nutrient depletion in the centre rapidly slows down growth rates.[20] Yet, it is in accordance with a metabolically active layer at the bottom and the edges of *E. coli* AR3110 biofilms.[24]

Continuous cell proliferation and matrix production seem to be the driving forces for sustained outward spreading of *E. coli* biofilms until the late stages of biofilm development (Fig. 16D – a shift of baseline intensities from 30 – 90 h). Even isotropic and uniform growth over a long period (linear radial velocity profile from 20 – 60 h) can lead to anisotropic and non-uniform patterns in *E. coli* biofilms due to non-uniform cell and matrix distribution. Such behaviour was suggested before from simulations of biofilm morphogenesis.[30]

Yet, in the latest stages of *E. coli* biofilm development (60 – 100 h), outward radial growth ceases in the biofilm interior and becomes dominated by circumferential growth around delaminated buckles. Wrinkled and delaminated biofilm regions were suggested to drive additional nutrients out of the substrate by increased evaporation or capillary action, which could serve as a driving force for bacteria proliferation in the vicinity of the delaminations.[81] Indeed, the presence of substantial deformations of the agar substrate below delaminated areas (Fig. 19B) could be caused by increased evaporation and a connected increase of cell proliferation.

A main limiting factor that we account for is the difficulty of bridging the scales between single-cell resolution (few µm-scale) and macroscopic biofilm development (cm-scale). A recently introduced mesolens optical system with the ability of 3D confocal imaging of biological specimens up to 6mm wide, still would not suffice.[140] The main constraint of our protocol for embedding fluorescent 3.5 and 10 µm fluorescent particles to follow *E. coli* biofilm growth is

the inability to sample the whole biofilm area until the later stages of *E. coli* biofilm development. For 3.5 µm fluorescent particles, outward spreading is not adequately captured from 10 h onwards as they are not embedded into the migrating non-matrix producing cells at the edge.

While in early-stage *E. coli* biofilm development (0 – 30 h) the sampling of 10 µm fluorescent particles is in a good approximation of the whole biofilm area, the further growth proceeds into late-stage biofilm development the more the sampling is restricted to the biofilm interior for the same reason as mentioned above. Another limitation of analysing particle trajectories in two dimensions is the neglected influence of movements in the vertical direction. While z-displacements might be small when tracking of 10 µm fluorescent particles inside 60-70 µm thick biofilms in a field of view of several centimetres, they are more substantial for 3.5 µm particle in a field of view of 650x650 µm. Indeed, in an early developmental period when biofilms predominantly increase their thickness due to cell proliferation and matrix production substantial vertical displacements are expected.

Future questions to investigate could comprise the individual contributions of osmotic swelling of a matrix-rich top layer and active cell growth at the bottom layer to overall non-uniform *E. coli* biofilm growth. Especially, how the impressive and stratified EPS matrix architecture in AR3110 *E. coli* biofilms gives rise to reversible deformations when undergoing a wrinkle-to-delaminated-buckle instability. The reorganization of the soft material and the ability to partially relax mechanical stresses introduced by cell proliferation and matrix synthesis should thus be further investigated on a micro-scale. Yet to follow *E. coli* biofilm development on a macroscopic scale, full-field methods (like DIC, PIV and PTV) prove useful tools to investigate morphogenesis programs *in-situ*. The adaptation of tools and methods from cell and tissue mechanics is expected to further advance the field of mechano-(micro)biology in the future.

4.3 Conclusion

In summary, we have shown that spatiotemporal non-uniform biological processes can give rise to the emergence of mechanical instabilities during *E. coli* AR3110 biofilm development. An initially non-uniform distribution of cells, due to the coffee-ring effect, favours non-uniform matrix production at an annular periphery, which is well sustained in early-stage biofilm development. The onset of outward spreading is further correlated with the onset of matrix

production in the biofilm interior at 10 to 20 h and local confinement of embedded micro-particles. These non-uniform biological processes lead to a non-uniform expansion of *E. coli* biofilms following four successive kinematic stages at a solid-air interface.

In addition to interfacial forces (e.g. friction) which confine the biofilm to the substrate, non-uniform growth gives rise to two mechanical instabilities during *E. coli* biofilm development. The initial wrinkling instability at an annular periphery is co-localized with the annular region of higher cell density (and thickness) and EPS matrix production. Due to sustained isotropic growth until the late stages of *E. coli* biofilm development, single wrinkles transition to delaminated buckles by localization of compressive forces. Thus, we have presented that biological processes such as cell proliferation and EPS matrix synthesis and film-substrate mechanics are intricately linked during *E. coli* biofilm morphogenesis.

5 ADAPTATION of *E.COLI* BIOFILM GROWTH, MORPHOLOGY and MECHANICAL PROPERTIES to SUBSTRATE WATER CONTENT

5.1 Results

The following section was written for the article "Adaptation of *E. coli* Biofilm Growth, Morphology and Mechanical Properties to Substrate Water Content." published in ACS Biomaterial Science and Engineering and adapted for this thesis with permission from the journal.[136]

In the present study, we explore how *E. coli* K-12 AR3110 biofilms adapt their spreading kinetics, morphology and rigidity to the water content of the substrate. We first study biofilm spreading kinetics with time-lapse imaging and correlate it with the delamination dynamics and the emerging morphology during and after biofilm growth. We then investigate biomass accumulation and biofilm water content as a function of substrate water content. Finally, we compare biofilm spreading and delamination behaviour to their mechanical properties and highlight how these features change as a function of substrate water content.

5.1.1 Substrates with high water content promote biofilm spreading kinetics

To understand how *E. coli* biofilm growth is influenced by substrate water content, we first explored their spreading behaviour on nutritive, hydrogel substrates of different nominal agar concentrations between 0.5 and 2.5 w/v% (Fig. 20A). The resulting substrates thus present different effective water contents between 97.70 and 95.26 w/w% and distinct mechanical properties ranging from 4.8 to 102.1 kPa as characterized by micro-indentation (Fig. 20B and Appendix 5). For this, we inoculated the various agar substrates with 5 µL of *E. coli* AR3110 cell suspensions (~2.5 x 10^6 cells / µL) and monitored biofilm growth by time-lapse imaging (Fig. 20C). The projected spreading area of the biofilm was measured as a function of time and plotted relative to the initial area A_i to account for variations of the initial droplet diameters (Fig. 20D). To better visualize the spreading kinetics, we further plotted the derivative of the relative area increase $A(t)/A_i$ (Appendix 6).

We identified the following 3 phases of *E. coli* biofilm development: in phase I, bacteria remain confined in the circular area defined by the drop of bacteria suspension initially inoculated onto the agar surface ($A(t)/A_i \leq 1$, Fig. 20D). In phase II, biofilms start spreading rapidly in lateral

directions ($A(t)/A_i > 1$, Fig. 20D) until they reach a maximum spreading rate (Appendix 6); in phase III, biofilm spreading slows down as characterized by the slower increase of relative projected spreading area (inflexion of the spreading curves on Fig. 20D).

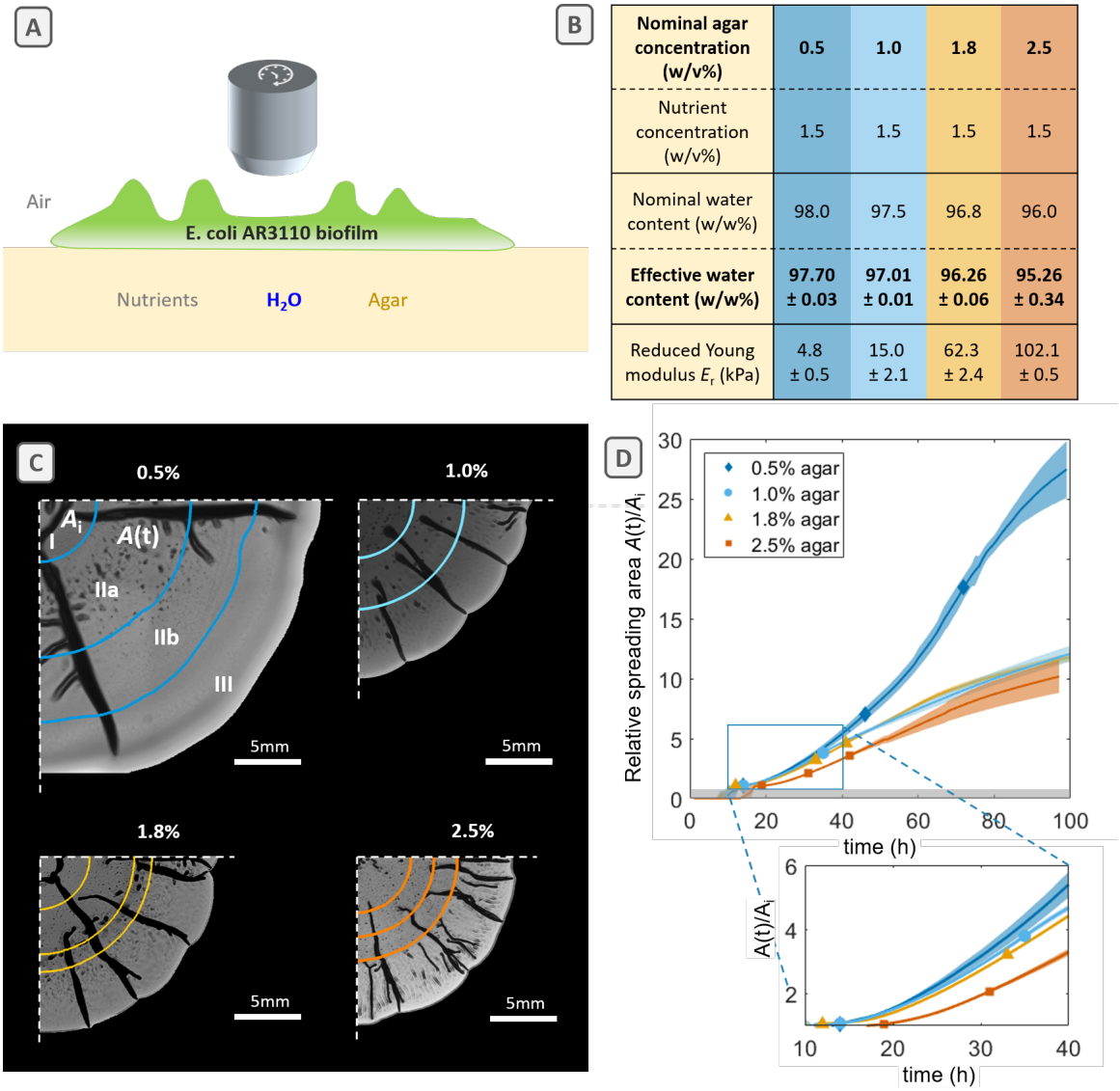

Nominal agar concentration (w/v%)	0.5	1.0	1.8	2.5
Nutrient concentration (w/v%)	1.5	1.5	1.5	1.5
Nominal water content (w/w%)	98.0	97.5	96.8	96.0
Effective water content (w/w%)	**97.70 ± 0.03**	**97.01 ± 0.01**	**96.26 ± 0.06**	**95.26 ± 0.34**
Reduced Young modulus E_r (kPa)	4.8 ± 0.5	15.0 ± 2.1	62.3 ± 2.4	102.1 ± 0.5

Fig. 20: *E. coli* AR3110 biofilm spreading kinetics on nutritive substrates with various agar concentrations. (A) Sketch of the live-imaging setup (B) Nominal and effective water contents and reduced Young moduli E_r, respectively, calculated and/ or measured for various nominal agar concentrations supplemented with 1.5 w/v% nutrients. (C) Bright-field image of a quarter of the biofilm after 90 h of growth on substrates with the respective agar concentration. Coloured outlines delimit the transitions of phase I-II (inner radius), IIa-IIb (middle radius, explanation in next section) and II-III (outer radius). Note that the latter two transitions happen at the same time point (35 h) for biofilms grown on 1.0 % agar. (D) Relative spreading area increases during 100 h of growth. The time points of the phase I-II, IIa – IIb and II-III transitions are indicated (symbols). (D, inset) Zoom into the relative area increase between 10 and 40 h of biofilm development. Individual measurements range from n = 3-9 per condition and standard deviations are shown as shaded, coloured areas.

While these 3 phases are observed in all conditions, they appear shifted in time. For example, the onset of biofilm spreading, which defines the beginning of phase II, appeared at later time points on substrates with low water content (Fig. 20D and 2C, 0.5 % agar). Indeed, biofilms grown on substrates with high and medium water content (0.5, 1.0% and also 1.8 % agar) started expanding laterally after 12-14 h. In contrast, biofilms grown on substrates with low water content (2.5 % agar) initiated spreading on average 19 h after inoculation (Fig. 20D, inset).

Moreover, the relative projected spreading area $A(t) / A_i$ increased faster on substrates with high water content (Fig. 20D). 20 h after entering phase II, the average relative spreading area of biofilms grown on 0.5 % agar increased up to 4-fold when compared to the area of the initial drop, whereas it expanded only 3-fold in the case of biofilms grown on 2.5 % agar (Fig. 20D, inset). This trend continued until 70 h after the onset of phase II. Biofilms grown on 0.5 % agar showed a 23-fold increase in spreading area, whereas biofilms grown on 2.5 % agar only reached an average area increase of 9.5-fold (Fig. 20D).

Biofilms grown on agar of medium and low water content (1.0 % - 2.5 % agar) displayed an initial accelerated spreading to reach a maximum spreading rate and entered phase III between 35 and 42 h (Fig. 20D and Appendix 6). Interestingly, biofilms grown on 1.0 and 1.8 % agar showed similar spreading kinetics in their phase III, while biofilms grown on substrates with high water content (0.5 % agar) exhibited an accelerated spreading until a late stage of biofilm development and only entered phase III after 67 h (Appendix 6).

5.1.2 Substrates with low water content promote biofilm buckling

As biofilms grow on a two-dimensional surface, accumulate biomass and subsequently internal mechanical stresses, they eventually bend in the third dimension in the form of wrinkles and eventually delaminated buckles (Fig. 20C). We thus asked if and how the observed effect of water content on biofilm spreading relates to the emergence of long and radial delaminated buckles. To compare the dynamics of this buckling process for different water contents, we measured the ratio of delaminated buckle-to-biofilm projected area as a function of time $A_{DB}(t) / A(t)$ (Fig. 21A and B). While biofilm growth can not be fully characterized in 3D with our system, this parameter called "projected delamination coverage" allows estimating quantitatively the ratio of biofilm growing in the vertical direction.

We first observed a delayed onset of delamination for biofilms grown on substrates with high water content (Fig. 21B, dark blue line plot) and defined the onset of buckling as the transition between phase IIa and IIb (Fig. 21C). Biofilms grown on 0.5 % agar substrates showed a delamination coverage >2.5 % only after 51 h. The first wrinkles appeared at about 20 h before they entered into phase III. In contrast, biofilms grown on 1.0, 1.8 and 2.5% agar substrates displayed a delamination coverage of >2.5 % already after 41, 36 and 34 h respectively. This is less than 10 h before entering the decelerating phase III of biofilm spreading for biofilms grown on 1.8 and 2.5% agar, whereas the onset of buckling and the transition to phase III coincided for biofilms grown on 1.0 % agar. Interestingly, the onset of buckling corresponds to a slight decrease of spreading acceleration in all the conditions, but the latter is only temporary in the case of biofilms grown on 0.5 % agar substrates (Appendix 6).

Fig. 21B also reveals a larger coverage with delaminated buckles for biofilms grown on substrates with low water content. After 90 h, biofilms grown on 2.5 % agar substrates were covered with up to 20 % of delaminated buckles, whereas biofilms grown on wetter substrates only reached an average delamination coverage of maximally 7 – 8 % (Fig. 21B). The values are surprisingly similar for biofilms grown on 0.5, 1.0 and 1.8 % agar substrates, considering that their buckling history is different.

The above results suggest that biofilms grown on substrates with high water content mainly rely on two-dimensional spreading while biofilms grown on dryer substrates mainly rely on the formation of three-dimensional delaminated buckles to distribute their biomass made of bacteria and hydrated matrix. We thus explored the morphology of the delaminated buckles as

a function of biofilm growth conditions in more detail. As evidenced in Fig. 21A, the delaminated buckles formed on biofilms grown on high water content substrates have a larger projected width when compared to delaminations formed on biofilms grown on substrates with low water content. To explain this observation, we embedded biofilms grown on the various substrates of interest in agar blocks and prepared cross-sections of the buckled regions (periphery). The resulting images reveal a nearly constant biofilm peripheral thickness, which ranges from 60 to 65 µm for biofilms grown on substrates with high and medium water content and a slight increase of 80 µm for biofilms grown on substrates of low water content (Appendix 8 and Appendix 9). The larger projected width observed for biofilm delaminated buckles formed on substrates with high water content (Fig. 21A) originates from a stronger tendency of the delaminated buckles to bend or collapse (Fig. 21D). On substrates with low water content, the delaminated buckles form more vertical with a higher aspect ratio, in agreement with what has been described before for AR3110 grown on 1.8% agar.[63]

Interestingly, the delamination process implies that the two bottom sides of the biofilm come in contact and adhere to form mm-scale structures from µm thick biofilms.[20] For *E. coli* AR3110, the two folded upper layers are separated by an area filled with non-matrix-producing cells,[63] which appears as a grey region in between the two matrix layers in the overlaid images (Fig. 21D, 1.0 to 2.5 %). However, the adhesion of these two upper, matrix-rich layers seems to be compromised on biofilms grown on substrates with high water content, as suggested by the white zones in the brightfield image between two detached matrix-rich layers in the overlaid images (Fig. 21D, 0.5 %). Note that we cannot completely exclude that this is an artefact of our cross-sectioning protocol, though the same morphologies were observed on several cross-sectioned delaminated buckles.

The different dynamics and apparent stabilities of the delaminated buckles, observed for *E. coli* AR3110 biofilms grown on substrates with various water contents, suggest that biofilm composition and/or matrix distribution are affected by the water availability from the substrate.

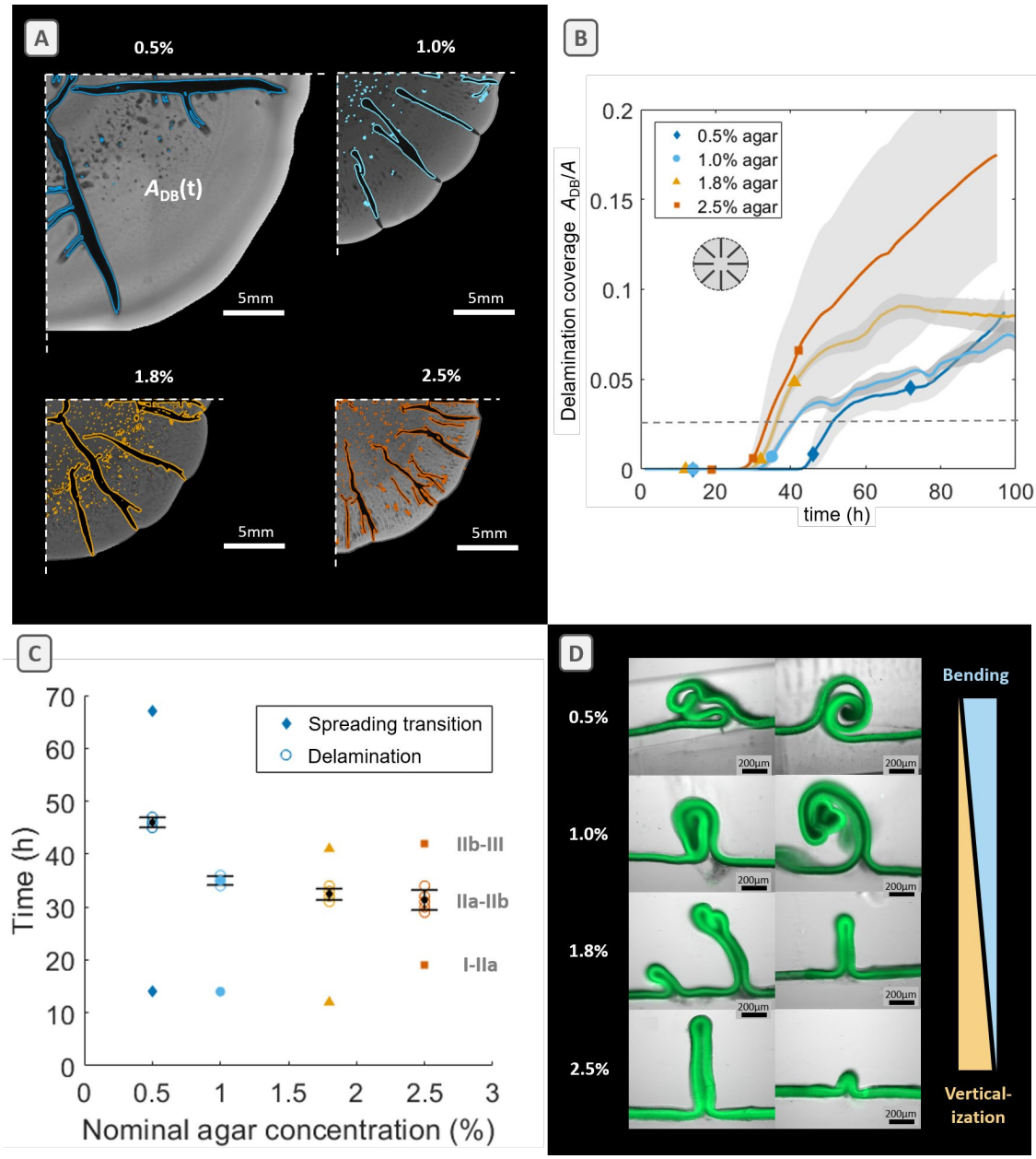

Fig. 21: *E. coli* biofilm delamination dynamics and cross-sectional delaminated buckle morphology on nutritive substrates with various agar concentrations. (A) Bright-field images of quarters of individual biofilms grown for 90 h on substrates with the respective agar concentration. Coloured outlines represent the delaminated buckle contours at 90 h (B) 2D projected delamination coverage $A_{DB}/A(t)$ during biofilm development on substrates with different water content. Symbols indicate transitions I-II (first), IIa-IIb (second) and II-III (third). Individual measurements range from n=3-9 per condition and standard deviations are shown as shaded areas. (C) Average onset times of biofilm lateral spreading (bottom, t= 12-19 h, I-II), biofilm delamination (middle, t= 31-46 h, IIa-IIb) and slow down of spreading (top, 35-67 h, II-III). (D) Brightfield images of cross-sectional cuts of biofilm wrinkles at 100 h of growth. Fluorescence images (green), showing matrix components stained with thioflavin S are overlayed.

5.1.3 Substrate water content influences biomass, biofilm water content and matrix distribution

E. coli biofilm growth at a solid-air interface is expected to result from a combination of cell proliferation, matrix production and water uptake. The total wet mass of a biofilm m_w comprises the mass fractions of cells $\phi_{\mathbf{cells}}$, matrix $\phi_{\mathbf{matrix}}$ and water $\phi_{\mathbf{water}}$ so that $\phi_{\mathbf{cells}}$ + $\phi_{\mathbf{matrix}}$ + $\phi_{\mathbf{water}}$ = 1,[39] (note that this theoretical study of Srinivasan et al used volume fractions, which are harder to measure experimentally due to the limited access to three-dimensional quantitative information). To assess the respective contributions of these components, we grew biofilms on substrates of different water contents for four days, scraped them from the agar surfaces, measured their wet (m_w) and dry mass (m_d) and calculated the biofilm effective water contents $W = \phi_{\mathbf{water}}$ * 100 % = ($m_w - m_d$) / m_w * 100 w/w%.

E. coli AR3110 biofilms grown on substrates with high water content (0.5 % agar) produced on average 1.8 times the amount of wet mass m_w relative to substrates with low water content (2.5 % agar) (Appendix 7). Upon drying at 60 °C for 3 h, single biofilms become fully dehydrated due to their small volumes and the remaining dry biomass m_d contains bacteria embedded in extracellular matrix components. This drying procedure yielded brittle yet intact pieces of biofilm material (Fig. 3A - insert). Interestingly, biofilms grown on substrates with high water content did not only contain a higher wet mass than biofilms grown on low water content substrates. On average, they also yielded 1.7 times more dry mass (Fig. 22A). Indeed, the total dry mass weighed 11.5 mg for biofilms grown on substrates with high water content (0.5 % agar) and the dry mass decreased with decreasing water content to 7.7 mg on 2.5 % agar (Fig. 22A).

As we observed a slight change in the ratio of dry to wet mass with agar concentration, we calculated biofilm effective water contents gravimetrically. Fig. 22B shows that the water content of the biofilms (W) increased as the agar concentration of the substrate decreased. Biofilms grown on substrates with high water content contained on average 80.8 % of water, whereas biofilms grown on low water content substrates stored on average 76.9 % of water. This indicates a change in the fraction of biomass ($\phi_{\mathbf{cells}} + \phi_{\mathbf{matrix}}$) inside the biofilm, which in turn suggests a change in the composition of the biofilm that may be accompanied by changes in matrix distribution. To verify this hypothesis, we analyzed cross-sections obtained from the periphery of biofilms grown on the various substrates. Fig. 22C shows cross-sectional

images of single biofilms where the matrix components amyloid curli and pEtN-cellulose fluorescently were again stained with thioflavin S.

For *E. coli* AR3110 macrocolonies, the production of matrix components is asymmetric with curli and pEtN-cellulose being synthesized exclusively in the upper layer exposed to air.[23] Within this layer, subzones that exhibit homogeneous or heterogeneous production of curli and/or pEtN-cellulose were also distinguished.[141] For biofilms grown on 1.8 % agar, we observed this asymmetric distribution of matrix components as reported before (Fig. 22C and D). Note that the 10 µm bottom layer of highly flagellated and non-matrix producing cells was probably lost during sample preparation. By lowering substrate water content (2.5% agar) we find a more symmetric distribution of matrix components from the top to the bottom of the biofilm (Fig. 22C and D), whereas the asymmetry seemed to be preserved for biofilm grown on 1.0 % agar (Fig. 22C and D). Interestingly, biofilms grown on substrates with high water content (0.5 % agar) also revealed this asymmetric distribution of matrix components (Fig. 22C and D) and presented additional heterogeneities penetrating the thick matrix layer at the top of the biofilm, which probably contains regions of non-matrix producing cells that are not stained by thioflavin S.

Clearly, the distribution of matrix across the biofilm cross sections changes depending on substrate water content while the biofilm thicknesses ranges from 60 - 80 µm for biofilms grown on substrates with high and medium water contents up to 80 - 100µm for biofilms grown on substrates with low water content (verified from brightfield images of peripheral and central cross-sections, Appendix 9). Indeed, thicker matrix-rich layers are formed on biofilms grown on substrates with low water content (2.5 % agar), whereas thinner and more porous matrix-rich layers are formed on substrates with high water content (0.5 % agar) (Fig. 22C and D).

5.1.4 Biofilms stiffen when grown on substrates with low water content

As the water content and composition of biogenic viscoelastic materials are key determinants for their mechanical properties, we hypothesized a further impact of the water content of the substrate on the mechanical properties of the biofilms. To assess how the observed differences in biofilm composition and matrix distribution translate into their mechanical properties, especially their rigidity or Young's modulus *E*, we performed micro-indentation experiments in the biofilm centre (Fig. 23A - photo). Upon contacting the biofilm surface with a spherical

diamond tip of radius R = 50 µm, the biofilms were indented by 7 to 30 µm. This allowed for locally probing the biofilm material in compression over a contact area that encompasses several bacteria embedded in a dense matrix, according to previous descriptions of the top layer of *E. coli* AR3110 biofilms.[63]

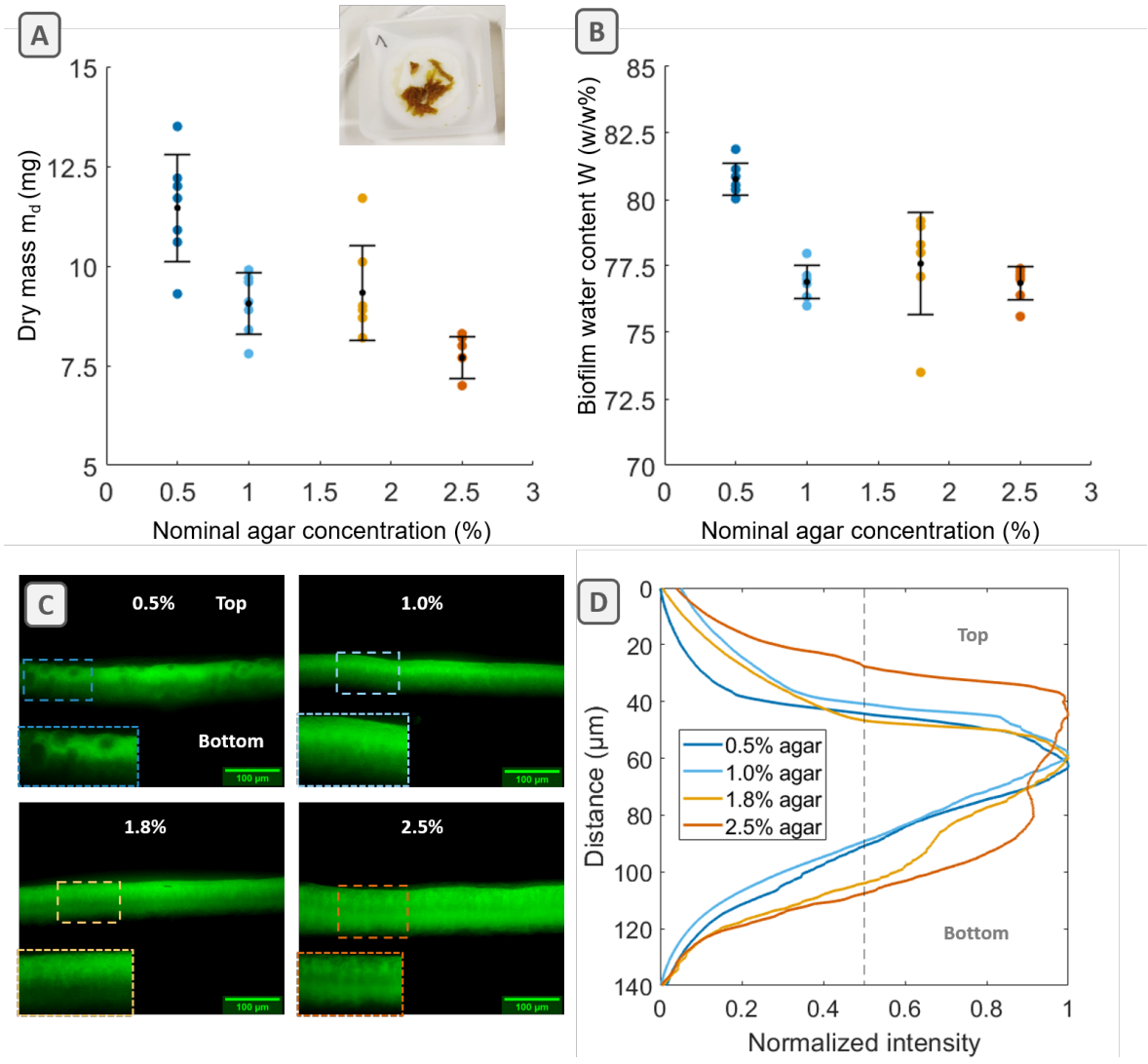

Fig. 22: Dry mass, water content and matrix distribution of *E. coli* biofilms grown on nutritive substrates with various agar concentrations. (A) Average dry masses m_d and (B) effective water content *W* of single biofilms grown for 4 days. (C) Fluorescence images of *E. coli* AR3110 peripheral biofilm cross-sections, depicting the distribution of amyloid curli protein and pEtN-modified cellulose fibres stained with Thioflavin S (green fluorescence). (D) Normalized average intensity profiles were recorded over each biofilm cross-sectional area as indicated in the rectangular colour-coded zoom in (C). The full-width at half maximum (FWHM) is indicated as a dashed line at 0.5, showing increased thickness of matrix layer in biofilms grown on 2.5 % agar. For wet and dry mass as well as water content measurements, n=7 individual biofilms per condition. Error bars indicate one standard deviation.

To estimate the rigidity of the biofilm, we calculated the reduced Young modulus values E_r from the load-displacement curves. We assumed a linear elastic response of the material at small deformations, i.e. at indentation depths of approximately 1/10 of the biofilm thickness, which is considered to measure approximatively 100 µm in the central region. We then fitted a Hertz model to the load-displacement curves, ranging from the contact of the tip on the surface (0 µm) to an indentation depth of a maximum of 10 µm (Fig. 23B). As expected, the resulting reduced Young's moduli E_r varied with the agar concentration of the substrate. Indeed, biofilms were one order of magnitude stiffer when grown on substrates with low water content, following a non-linear increase of reduced Young's moduli E_r from 50 kPa for biofilms grown on substrates with high water content to 360, 400 and 500 kPa for biofilms grown on 1.0, 1.8 and 2.5 % agar substrates, respectively (Fig. 23C).

We further observed a hysteresis behaviour between the loading and unloading curves. This allowed us to derive a plasticity index ψ, which estimates the reversibility of the surface deformation.[135] The plasticity index ψ, calculated from the areas under the loading and unloading curves, compares the amounts of energy stored (elastic behaviour) and dissipated (viscous and plastic behaviour) during the deformation of the biofilm (Fig. 23D, Fig. 14). Despite substantial differences in their rigidity (E_r), the ratio of elastic vs. plastic deformation appears similar (around 0.5) for biofilms grown on substrates with low and medium water contents (1.8 and 2.5 % agar). In contrast, biofilms grown on substrates with high and medium water content (0.5 % and 1.0 % agar) present a lower plasticity index around 0.2 - 0.3. All in all, these results suggest that both the rigidity of the biofilm material as well as the energy elastically stored adapts to the water content of their nutritive substrate.

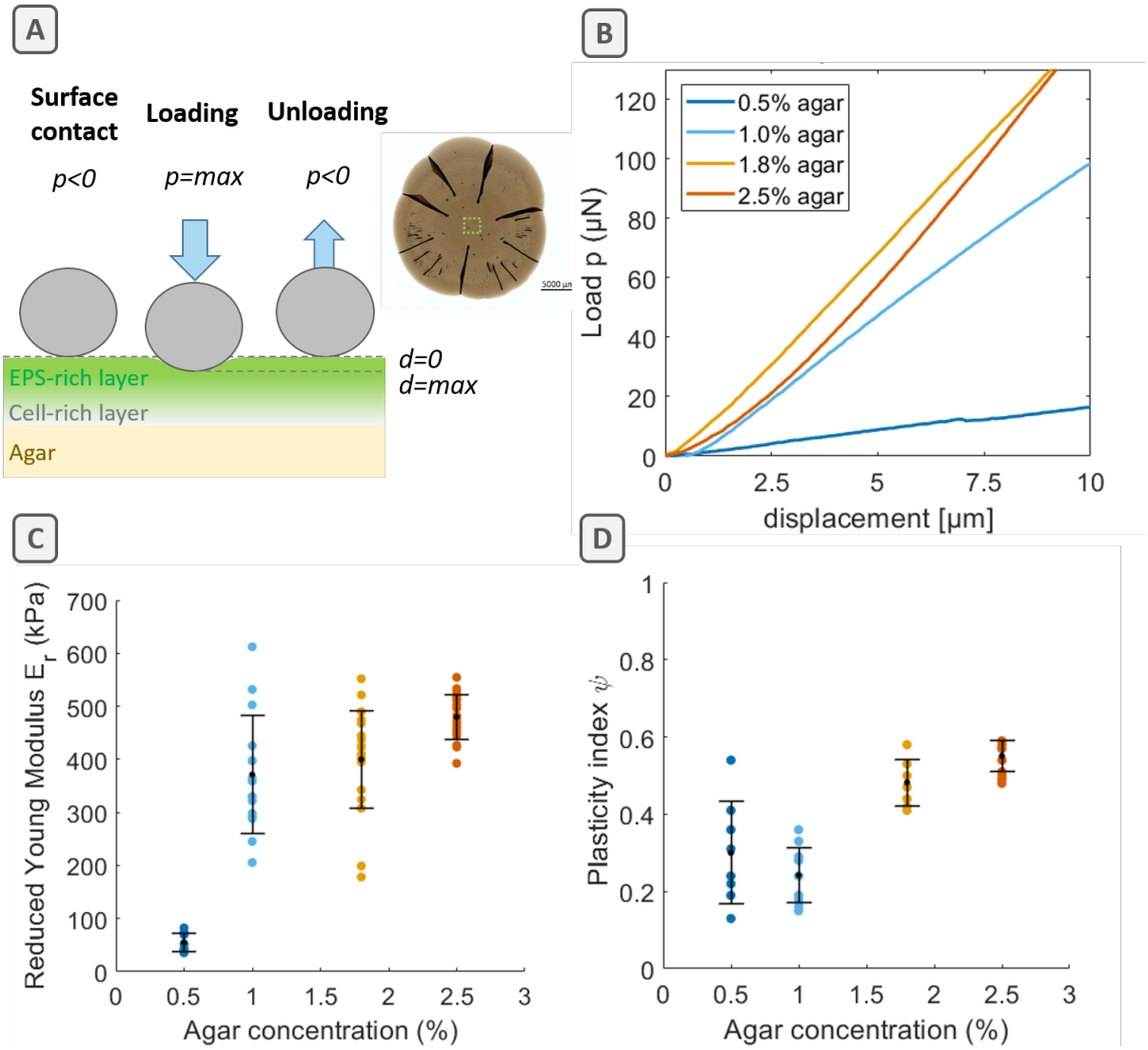

Fig. 23: Micro-indentation of *E. Coli* biofilms grown on nutritive substrates with various agar concentrations. (A) Sketch of surface indentation during loading and unloading the biofilm surface. (B) Load-displacement curves when indenting the biofilm surface (loading curve). (C) Averaged reduced Young modulus E_r values, describing the measured rigidity of the biofilm surface. (D) Averaged plasticity indices ψ, describing the ratio between dissipated (1 = fully irreversible) to elastically stored (0 = fully reversible) energy during indenting the biofilm surface. The number of individual measurements is n = 8-23 per condition. Shown are mean values and standard deviations as error bars.

5.2 Discussion

While previous studies of *E. coli* biofilm development and the emergence of complex structures focused on genetically driven effects resulting from nutrient and metabolic gradients,[23] the present work explores the interplay of these morphological features with *E. coli* biofilm mechanics and puts a particular focus on the influence of the water content in the

environment. Specifically, we have demonstrated that *E. coli* AR3110 biofilms, grown at the solid-air interface, adapt their spreading kinetics, morphology and mechanical properties to the water content of the agar substrate. In comparison, the morphogenesis of *B. subtilis* and *V. cholera* biofilms has already been shown to be influenced by agar concentration (i.e. water content). These biofilms adopt faster spreading kinetics on wet substrates and develop more morphological features on dryer substrates.[19,52,60,79,80] Here we show that *E. coli* AR3110 biofilms adopt similar behaviour (Fig. 20A and Fig. 21A), which infers that similar physical mechanisms are involved, namely surface forces,[85] water evaporation and osmotic swelling, rather than microbial sensing of substrate stiffness.[60]

E. coli biofilm spreading on wet substrates may be facilitated by the reduction of interfacial friction (or tangential adhesion) between the biofilm and the substrate due to a thin layer of water directly available at the surface.[20,142] Note that in extreme cases, like on 0.5 % agar, one approaches the concentrations used for *E. coli* swimmer plates so that such conditions might also promote bacterial swimming motility favourable to biofilm spreading.[143] On dryer substrates, however, interfacial friction was proposed to constrain biofilm spreading mechanically, thereby causing a continuous compression of the biofilms as they grow.[19,20] The accumulation of such tangential compressive stresses further leads to mechanical instabilities like buckling events from which surface wrinkles emerge. Once the normal adhesion forces on the agar gel are overcome, the biofilm delaminates from the substrate and further grows in the third dimension. Delayed biofilm spreading and early wrinkling and delamination, as observed on dryer substrates (Fig. 21C), suggest that friction plays a similar role here. Inversely, delayed buckling in biofilms grown on substrates with high water content may be attributed to the early and large spreading rates, which may slow down the accumulation of compressive stresses. Note that substrates with high water content have higher compliance to the deformations induced by biofilm growth (Fig. 20B and Appendix 5), but these are likely screened by the reduced adhesion and friction forces resulting from the abundance of water at the surface, as suggested by the few but large delaminated buckles (Fig. 21D). Interestingly, enhanced buckling of *E. coli* AR3110 biofilms due to confined growth has recently been obtained independently of substrate stiffness by coating the agar surface with positively charged polyelectrolytes.[86] In this context, interfacial friction was proposed to result from physicochemical interactions between negatively charged bacteria and positively charged coatings.

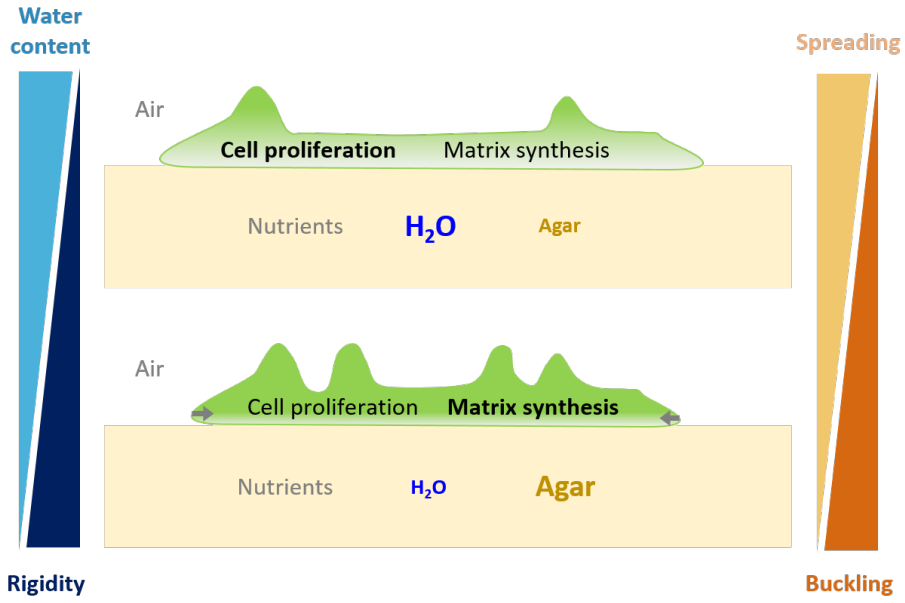

Fig. 24: *E. coli* AR3110 biofilms have higher water content when grown on substrates with high water content (top) while they are more rigid when grown on substrates with low water content (bottom). This is consistent with the higher cell proliferation expected to be supported by a nutrient supply facilitated on substrates with high water content and with the observation of a more densely and homogeneously distributed matrix across biofilms grown on substrates with low water content. Together with these biofilm materials properties, the interfacial friction at the surface of the agar may largely contribute to various morphologies of *E.coli* AR3110 biofilms as they spread more on substrates with high water content (top) while they tend to grow in the third dimension on substrates with low water content (bottom).

As demonstrated for *B. subtilis* biofilms, buckling also increases the surface area at the biofilm-air interface and promotes the evaporation of water.[81] This phenomenon constitutes a potential driving force to transport nutrient-carrying water from the substrate to the biofilm and can be particularly useful in conditions of low nutrients and/or water availability. Note that our results obtained with *E. coli* AR3110 are consistent with this proposition as biofilms grown on dryer substrates show larger delamination coverages (Fig. 21A and B).

Matrix swelling is another mechanism proposed to be involved in the adaptation of biofilm morphology to substrate water content.[41,60,85] Indeed, the excretion of matrix components by the bacteria creates osmotic gradients, inducing water uptake and biofilm swelling. At the interface with substrates of low agar concentrations (i.e. high water content), such gradients are expected to be particularly sharp and the biofilms are expected to take up more water, as we measured in *E. coli* AR3110 biofilms (Fig. 22B). For *E. coli* AR3110 biofilms, the pEtN-

modified cellulosic component is expected to greatly contribute to water-binding and matrix swelling.[126] This is different for *B. subtilis* biofilms, where water-binding was related to the presence of solutes instead of matrix components.[89] Together with the lower friction, higher matrix swelling may also partially contribute to the larger biofilm spreading observed on low agar substrates (Fig. 20C and D).

Larger spreading provides a higher number of bacteria with the advantage to be in direct contact with the nutrient-rich surface.[60] In such favourable conditions, bacteria are expected to favour proliferation upon matrix production,[23] which could explain the lower matrix signal (Fig. 22C) and the lower mechanical properties (Fig. 23C) observed for biofilms grown on 0.5 % agar substrates, despite their higher dry mass (Fig. 22A). Biofilm spreading was observed to slow down later on the substrates with high water content (beginning of phase III, Fig. 21C and S2). This change of spreading behaviour cannot be explained by the growth in the third dimension alone since the onset of wrinkling and delamination appears earlier in most of the conditions (Fig. 21C). Alternative explanations could be a reduction in nutrient supply or matrix swelling and/or an increase of interfacial friction as water from the agar surface diffuses to the biofilms. Further investigations are yet needed to understand the limits of *E.coli* AR3110 biofilm spreading at the solid-air interface.

Besides influencing biofilm morphogenesis, the water content of the underlying substrate also influences the quantity and the quality of the biofilm material produced by *E. coli* AR3110 (Fig. 22 and Fig. 23). Indeed, biofilms grown on wet substrates contain more water and, at the same time, also higher dry biomass (Fig. 22A and B). These results are consistent with the trend observed on wet masses of *V. cholerae* biofilms measured on substrates with various agar contents and further support the role of osmotic spreading[60] (Appendix 7). Moreover, a qualitative characterization of biofilm composition using fluorescence imaging indicated that the thickness of the matrix-rich layer as well as the matrix density – thus the contribution of matrix $\phi_{\mathbf{matrix}}$ to the fraction of biomass ($\phi_{\mathbf{cells}} + \phi_{\mathbf{matrix}}$) – are larger on dryer substrates (Fig. 22C). We similarly infer that the contribution of bacteria mass $\phi_{\mathbf{cells}}$ is larger in biofilms grown on wet substrates, which show thinner matrix-rich layer and lower matrix density. Consistently, micro-indentation revealed that the reduced Young moduli E_r of biofilms grown on wet substrates are lower on wet substrates (Fig. 23C), where the biofilms contain more water and less matrix, and form delaminated buckles that are mechanically unstable (Fig. 21D).

The different rigidities of the *E. coli* AR3110 biofilms thus partially stem from the different compositions of the biofilms ($\phi_{\mathbf{cells}}$, $\phi_{\mathbf{matrix}}$ and $\phi_{\mathbf{water}}$) obtained on the different substrates. In this regard, theoretical models relating polymer volume fractions to osmotic pressure and elastic properties, and which are traditionally used to predict the mechanical behaviour of hydrogels have already been applied to biofilms.[40,60,144] However, *E. coli* AR3110 biofilms are also known for their asymmetric architecture, which is greatly heterogeneous across their thickness[23,26,63] and is expected to significantly contribute to mechanical behaviour of the biofilm material. In that regards, *E. coli* AR3110 biofilm morphogenesis may be better described by trilayer models similar to those used for *V. cholerea,*[19] where the top layer would correspond to the matrix-rich layer of the biofilm, the bottom layer would be the substrate and the middle layer would be essentially made of water and bacteria (Fig. 22D and Appendix 7).[26]

In general, applying simple theoretical models on such materials may require approximations that should be considered with precautions, as done with the Hertz model used to estimate the reduced modulus from the micro-indentation curves obtained in the matrix-rich upper layer of the biofilms (Fig. 23A and B). Moreover, both swelling and mechanical properties of a hydrogel strongly depend on the interactions between the macromolecules inside the polymer network. In *E. coli* AR3110 biofilms, the presence of amyloid curli and pEtN-cellulose matrix fibers and their interactions in the form of crosslinking or simple entanglement contribute to the global mechanical behavior.[127] A greater swelling and lower rigidity of biofilms grown on high water content substrates could therefore result from weaker interactions between the matrix fibers due to the larger proportion of water. Even though multiple factors may contribute to biofilm rigidity, the general trend shows that biofilms with lower water content are more rigid. Further studies are yet needed to elucidate how water interacts with the *E. coli* AR3110 biofilm matrix on a molecular level and how this translates into altered mechanical properties.

5.3 Conclusion

Taken together, these structural and mechanical observations are not only consistent with the role of matrix swelling in biofilm spreading (Fig. 20), but also with the different winkling and delamination behaviour observed in biofilms grown on substrates with various water contents (Fig. 21). In addition to interfacial friction, non-uniform growth and substrate stiffness, the

buckling behaviour of a biofilm is known to depend on its effective mechanical properties,[70] which in turn depends on its composition and internal structure. Interestingly, the macromorphology of *E. coli* AR3110 biofilms appears to be comparable to the morphology of *B. subtilis* and *V. cholera* biofilms all characterized by the emergence of long radial wrinkles and delaminated buckles (Fig. 20A).[19,20,53,60,81] However, recent work comparing various mutants of matrix-producing *E. coli* reported distinct micromorphologies,[125] thereby illustrating the crucial role of the composite nature of the matrix in biofilm morphogenesis. Further dynamic and quantitative studies of biofilm mechanics are required to verify in which conditions the mechanisms proposed for other biofilm forming bacterial species would apply for *E. coli*.

While the observed adaptation of biofilm material properties to substrate water content certainly provides bacteria with suitable protection against stresses like starvation and desiccation,[26] it can also be leveraged in the perspective of engineering biofilm-based materials. Indeed, our work points out alternatives to complex synthetic biology and genetic engineering of bacteria for tuning biofilm properties in view of growing functional living materials. Namely, engineering the environment during biofilm production can also yield a large range of materials properties. Ultimately, understanding the genetic and biochemical pathways as well as the physicochemical mechanisms involved in biofilm response to environmental conditions will enable us to predict the properties of the resulting biofilm-based material.

The present study constitutes a first step towards understanding the physicochemical processes. It shows that *E. coli* AR3110 biofilms adapt to the water content of their substrates and contain more water and dry mass when grown on wet substrates. This in turn promotes their spreading area but results in a softer material. In contrast, *E. coli* AR3110 biofilms grown on dryer substrates cover a smaller area and have a denser matrix, which confers them mechanical properties approaching those of mammalian tissues with Young's moduli of several hundred kPa ($E \sim 4E_r/3$, Fig. 23C). These results are particularly interesting when considering the potential of biofilm-based materials, and especially *E. coli* matrix-based materials for therapeutic applications[145] and tissue engineering.[146]

6 EPS COMPOSITION DETERMINES MICROSCALE MECHANICAL PROPERTIES of *E.COLI* BIOFILMS

6.1 Results

This chapter reports the analysis of the effect of an altered EPS matrix expression of *E. coli* bacteria on the mechanical properties of their biofilms. The macro-morphology and spreading diameters of biofilm formed by wild-type and EPS-deficient *E. coli* strains are first studied using brightfield microscopy, and their dry mass and water content are quantified gravimetrically. The contribution of amyloid curli and pEtN-modified cellulose fibres to the rigidity of biofilms is assessed using micro-indentation. Further information about biofilms adhesion properties could be derived from their contact to the indenter tip during unloading. Finally, stress relaxation experiments enabled us to compare the viscoelastic behaviour of *E. coli* biofilms with altered EPS composition.

6.1.1 EPS matrix composition influences *E. coli* biofilm spreading, dry mass and water content

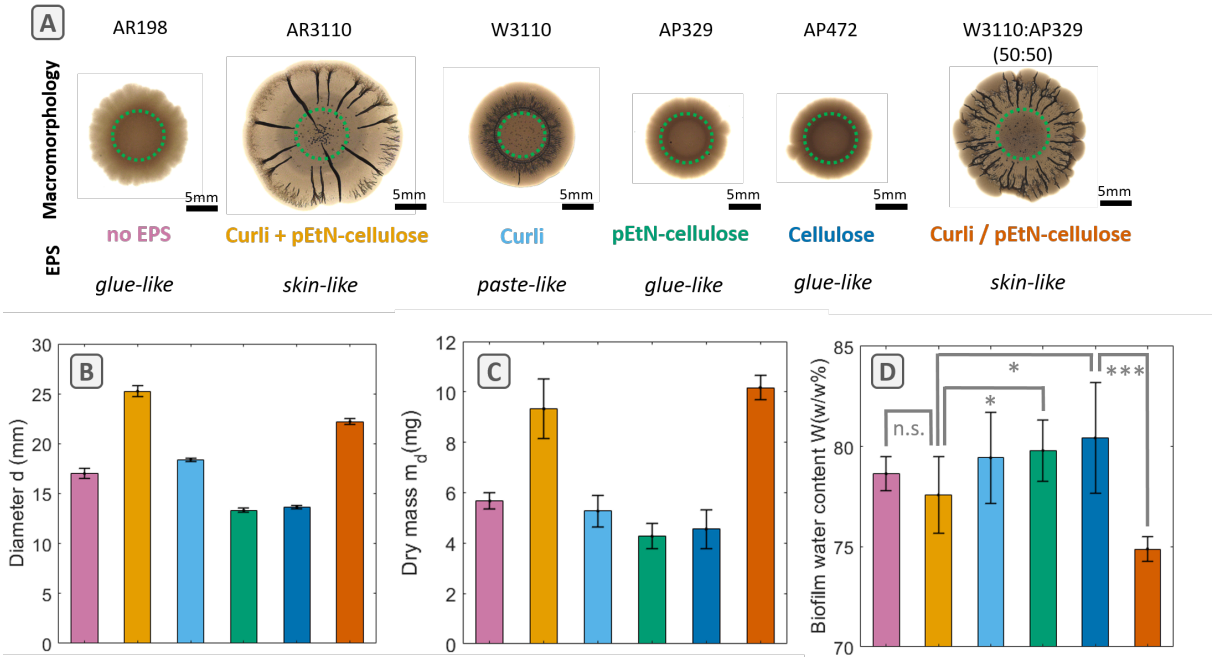

Fig. 25: EPS matrix composition influences biofilm spreading, dry mass and water content. (A) Biofilm macromorphologies for mutant *E. coli* strains with indicated EPS matrix composition after 4 days of growth (top row). (B-D) Biofilm average diameter, dry mass and water content; n = 7-9 biofilms, green circle in the biofilm centre indicates the region of micro-indentation experiments following in the next subsection. Two sample, two-tailed t-tests were performed for statistical analyses. In (D) p-values are denoted as * $p < 0.05$; *** $p < 0.0005$, n.s., $p > 0.05$.

To investigate the influence of the EPS matrix composition on biofilm growth and the emergence of rigid and viscoelastic mechanical properties in AR3110 *E. coli* biofilms, we grew biofilms from various EPS deficient strains for four days. Besides AR3110, we cultured biofilms from a strain producing only curli (W3110), from a strain producing only pEtN-cellulose (AP329), from a strain producing only non-modified cellulose (AP472) and from a strain producing neither curli nor cellulose (AR198). Moreover, we cultured biofilms from a suspension containing a 50:50 mixture of W3110 and AP329 bacteria. As reported before, we observed different macro-morphologies in biofilms lacking some components of their EPS matrix. AR3110 biofilms form long radial delaminated buckles, whereas W3110 biofilms form an annular buckle with slight radial features (Fig. 25A). When manipulating them, AR3110 biofilms exhibit a skin-like behaviour whereas W3110 biofilms exhibit a paste-like behaviour. Biofilms lacking the amyloid curli component or both main EPS components remain featureless while exhibiting more glue-like properties upon scraping them from the soft agar substrate.

Interestingly, the mixed-species biofilms expressing curli and pEtN-cellulose components from different cells resemble a macro-morphology similar to that of AR3110 with long radial features and skin-like properties (Fig. 25A).

As EPS-deficiency usually results in lower biomass production of biofilms, we measured the average dry biomass produced and diameters to which the biofilms expanded after 4 days of growth. *E. coli* AR3110 biofilms produce almost twice the amount of dry biomass compared to the curli-deficient strains, which is correlated by approximately twice the average spreading diameters of these biofilms (Fig. 25B, C). An increase in dry biomass suggests increased cell proliferation and matrix production. In turn, matrix production favours biofilm spreading (increased diameters) and thereby enables access to a larger nutrient rich-surface. All biofilms deficient in producing either amyloid curli or pEtN-modified cellulose only reach an average dry mass of 4 – 6 mg, while biofilms with both these two EPS matrix components reach 8 – 10 mg. The average spreading diameter of these matrix-deficient biofilms is reduced to 10 – 20 mm compared to 20 – 25 mm for biofilms producing both the two main EPS components. Therefore, the combination of amyloid curli and pEtN-modified cellulose as main EPS matrix components seems to enable the wild-type *E. coli* AR3110 biofilms to produce more biomass by increasing the access to the nutrient-rich surface. While this ability is lost in matrix-deficient biofilms, it appears to be restored when growing mixed-species biofilms expressing curli and pEtN-cellulose from different bacteria (Fig. 25B, C).

Furthermore, AR3110 biofilms were proposed to benefit from the assembly of a curli and pEtN-cellulose fibre network, which provides them with tissue-like elasticity.[63,126] Besides EPS composition, the ability for water uptake also influences the mechanical properties of hydrogel-like materials like biofilms. We further compared the water contents of biofilm obtained from wild-type and EPS-deficient strains (Fig. 25D). We found that curli-deficient strains show slightly increased water contents of biofilms of about 80% w/w compared to 77.6 % w/w for the wild type AR3110 biofilms. The mixed-species biofilms reveals a same trend as their water content of 74.9 % w/w appears to be significantly reduced compared to curli-deficient biofilms. Since the water uptake of *E. coli* biofilms presents only slight differences upon altered EPS compositions, its influence on *E. coli* biofilm mechanical properties is expected to be minor.

6.1.2 Curli amyloid fibres provide rigidity to *E. coli* biofilms

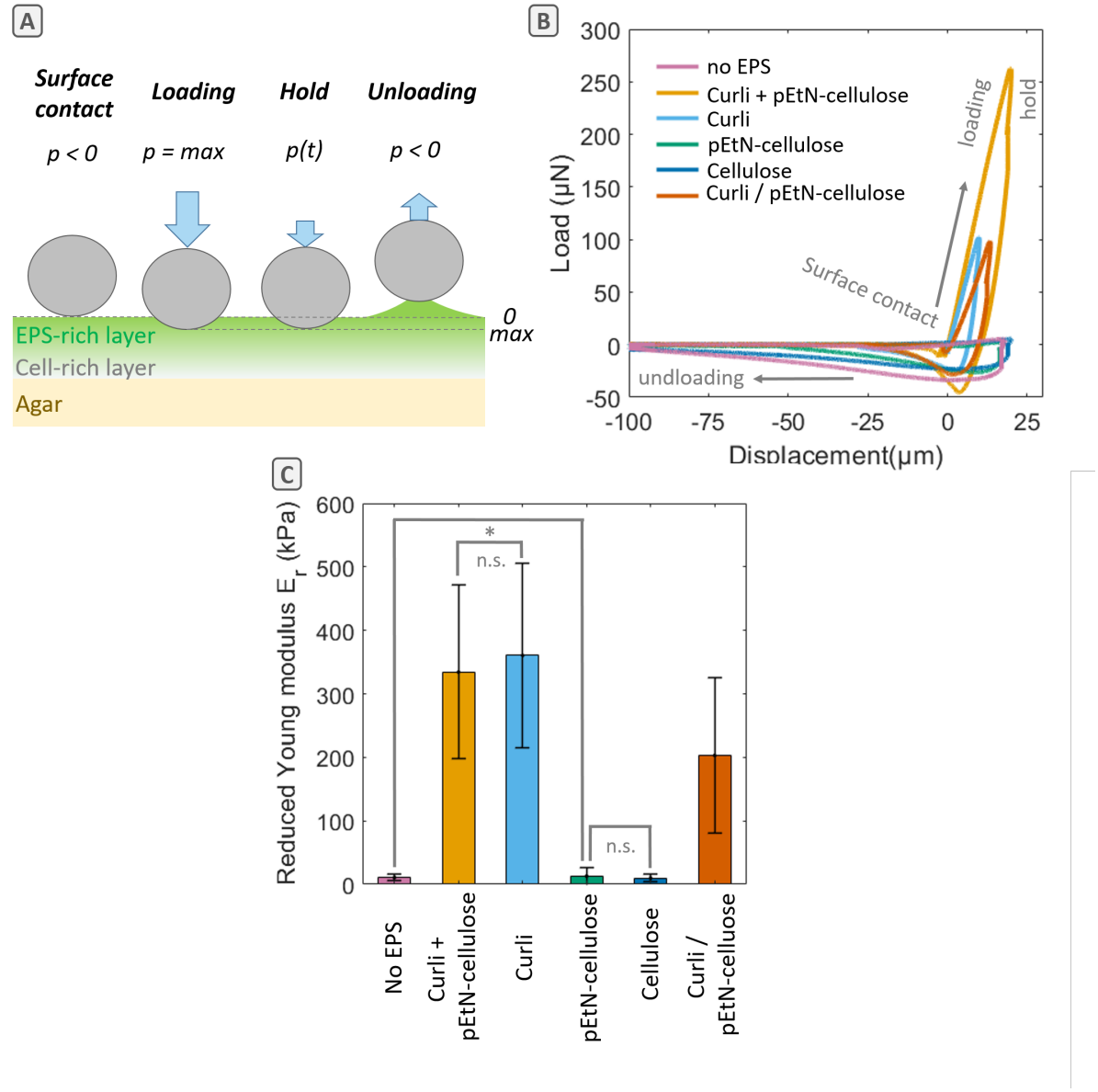

Fig. 26: Mechanical properties of *E. coli* biofilms with different EPS compositions. (A) Sketch of the micro-indentation process, done in displacement-controlled mode, showing the establishment of surface contact, the loading segment, a hold segment at constant displacement and the unloading of the tip from the surface. (B) Representative load-displacement curves of *E. coli* biofilms with different EPS matrix compositions with indicated loading and unloading direction. (C) Averaged reduced Young's moduli values E_r for *E. coli* biofilms with different EPS matrix compositions. Two sample, two-tailed t-tests were performed for statistical analysis. In (C) p-values are denoted as * $p < 0.05$; n.s., $p > 0.05$.

The material properties of viscoelastic hydrogel-like materials are not only influenced by their water uptake but also by the nature of their constitutive molecules, as well as their assembly and their crosslinking.[103] Therefore, we further studied the rigidity of biofilm surface layers as a function of their EPS matrix composition. As biofilm material properties are highly heterogeneous and structure-dependent, we performed micro-indentation experiments to test the EPS-fibre network surrounding the bacteria and thereby find a compromise between highly localized and bulk mechanical information.

Therefore, a 50 µm diamond indenter tip was utilized to ensure contact to several tens of bacteria embedded in a fibrous EPS network at the biofilm surface.[63] In depth-sensing indentation studies using AFM and nano-indentation techniques, finding the true surface of soft samples is often challenging, and any pre-approach/contact of the tip-sample can influence the surface characteristics and/or vary the tip-surface contact energies over tip contamination. Accordingly, the "air-indent" technique[134] was deployed to ensure contact with a pristine surface by starting the measurements before the tip-surface contact. In this technique, the measurement can be started while the tip is away (100-300 µm) from the sample surface (Fig. 22B). Accordingly, by starting the measurement and approach of the tip toward the sample surface ($p = 0$), the attraction force from the biofilm surface toward the tip was detected, and the recorded depth was used for defining the true surface of the sample (Fig. 26A - $p < 0$, Fig. 26B – surface contact).

By further tip approach toward the sample, the surface is indented elastically. We only considered load-displacements curves with displacements from 7 to 30µm to avoid non-linear variation of Young's moduli upon small displacements and avoid displacements larger than 30 µm to circumvent the attachment of sample to the conical tip holder (Fig. 24A, $p = max$, Fig. 24B – loading). To ensure a stable tip-surface detachment (rather than a quick forward and backward tip movement), a holding step was included, where the biofilm surface viscoelastically relaxes the applied loading (Fig. 24A - $p(t)$, Fig. 26B – hold). Later and by reaching the maximum defined approach distance, the tip is retracted from its maximum indentation depth to about 100 µm above the surface (displacement = -100 µm). This was necessary as biofilms, especially curli-deficient ones, strongly adhere to the indenter tip (Fig. 26A – $p < 0$, Fig. 26B – unloading).

The slope of the load-displacement curve gives the first impression of the rigidity of material upon loading. Fig. 26B shows that all biofilms producing amyloid curli reach much higher maximum loads (p = max) than curli-deficient strains when loaded to comparable indentation depths. To quantify the rigidity, we fitted a Hertz model for small displacements (< 10 µm) remaining in the linear elastic region. When calculating the reduced Young's modulus values E_r, we find that the most rigid materials under compression are found in the AR3110 and W3110 biofilms (about 360 kPa), in which every cell is capable to produce amyloid curli-fibres. Interestingly, while mixed species biofilms are well capable of creating skin-like films (Fig. 25A), their rigidity is reduced to around 200 kPa. This is still 10-fold higher than the reduced Young's modulus values obtained from all biofilms grown from curli-deficient strains. A reduced Young's modulus of 20 kPa for curli-deficient biofilms resembles more the mechanical properties of a soft hydrogel (such as a 1% agar hydrogel - Appendix 5),

Combining these impressive differences in mechanical rigidity, we conclude that the amyloid curli matrix component is essential for the structural integrity of *E. coli* biofilms. Curli-deficient strains are not able to produce a rigid material. The reduced rigidity of mixed-species biofilms, where only one of its two mutant strains is capable of producing amyloid curli fibres, might be attributed to the overall reduced amount of curli available for the construction of a rigid fibre network. Furthermore, we cannot observe a statistical difference between average reduced Young's moduli between mutant strains that produce pEtN-modified cellulose and non-modified cellulose. A possible explanation is a change in microscopic EPS architecture, as cellulose-only producing bacteria were shown to be embedded in loose sheets of cellulose fibres at the biofilm surface.[63] This altered architecture might be insufficient to support long-range cohesion and elasticity on the microscopic scale tested here. If the EPS structure is not coherent, deriving Young's moduli from a purely elastic material model is thus insufficient. A better description might be a viscoelastic material model accounting for stress relaxation over time.[103]

6.1.3 Lack of curli fibres increases adhesion energy and fluid-like behaviour

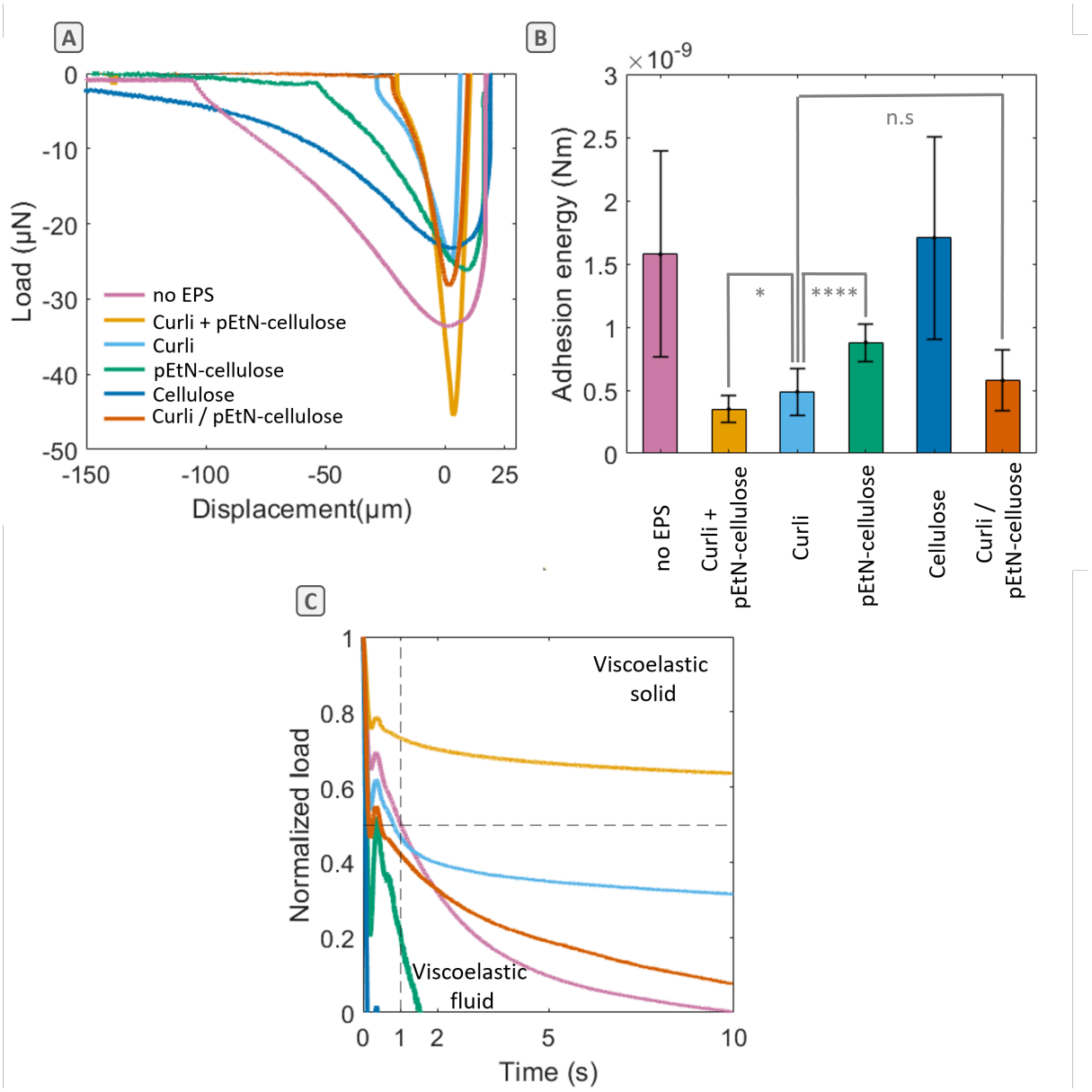

Fig. 27: The composition of the EPS matrix in *E. coli* biofilms modulates the adhesion energy of the biofilm surface and its viscoelastic stress relaxation behaviour. (A) Representative load-displacement curves upon retraction of the spherical indenter from the biofilm surface, ($p < 0$). (B) Averaged adhesion energy calculated as the integrated area under the load-displacement curves for $p < 0$; $n = 10 – 25$ individual indentation experiments from 2 - 4 different biofilm samples per condition. (C) Averaged load – time curves during 10 s holding periods indicating the stress – relaxation behaviour for *E. coli* biofilms with different EPS matrix composition; $n = 5 – 10$ individual indentation experiments from 2 different biofilm samples per condition. Two-sample, two-tailed t-tests were performed for statistical analyses. In (B) p-values are denoted as * $p < 0.05$; **** $p < 0.00005$; n.s., $p > 0.05$

As we observed that large negative forces (p = - 50 µN) and displacements (< -150 µm) are necessary to detach the tip from the biofilm surface, we quantified biofilm adhesion energies as the respective areas under the unloading part of the load-displacement curves (Fig. 27A). The EPS components, the bacteria and the interfacial tension of water, all can mediate the adhesion of the biofilm to the diamond tip. Reaching zero loads with positive displacement indicates a hysteresis behaviour, which is indicative of viscoelastic materials.[94] For more compliant hydrogel materials (< 100 kPa), capillary forces can dominate in the tip-surface interaction arising upon indentation.[115]

A lack of amyloid curli fibres renders *E. coli* biofilms more adhesive or 'sticky'. What was a qualitative description in Fig. 25A describing the handling of biofilms when scraping them from the agar substrate, is quantified here by the substantial negative load and displacement needed to separate the tip from the biofilm surface, especially for curli-deficient strains (Fig. 27A). The formation of a liquid bridge visible to the naked eye upon unloading below zero displacements (i.e. above the surface), mirrors the long tail in the load-displacement curves (Fig. 27A). When amyloid curli is present in the *E. coli* EPS matrix, such as in AR3110 and W3110 biofilms, low averaged adhesion energies of 0.35 and 0.49 x 10^{-9} Nm respectively are reached (Fig. 27B). Slightly increased adhesion energies of 0.58 x 10^{-9} Nm are reached when curli and pEtN – modified cellulose is produced from different bacteria inside the biofilm (Fig. 27B). The adhesive behaviour of amyloid curli containing biofilms is characterized by a narrow load-displacement curve, which is almost symmetric around the initial contact point with the surface (zero displacements).

The opposite behaviour was observed for curli–deficient biofilms, which reveal a wide and asymmetric load-displacement behaviour upon unloading and averaged adhesion energies of 0.88 and 1.71 x 10^{-9} Nm for pEtN-modified cellulose and cellulose – only containing biofilms respectively. Here, the complete detachment of the tip happens beyond 50 µm above the surface, which shows that the biofilm surface undergoes a substantial deformation during tip retraction. This mechanical behaviour may be mediated by the reorganization of bacterial cells, EPS matrix fibres and water, as suggested by the loosely organized EPS matrix architecture present at the surface of curli–deficient *E. coli* biofilms.[63]

A change of EPS composition and architecture is expected to provide curli-deficient *E. coli* biofilms with the ability to relax stresses faster. To study the viscoelastic stress relaxation

behaviour of biofilms, we included a hold segment of 10 s at the maximum load after reaching the maximum indentation (constant mechanical strain/deformation). During this 10 s hold period, the compressive stresses can relax through the reorganization of the biofilm material. It is expected that the stress relaxation on shorter times scales (10 s) would derive from the flow of water in the porous network (fast, t < 1 s) and the reorganization of the EPS network itself (slower, t < 10 s).[122]

The reorganization of single bacterial cells was shown to appear only on very large time-scales (> 100 s) for *P. aeruginosa* biofilms and is thus expected to play a minor role.[147] Consequently, we observed the fastest relaxation of normalized load for curli-deficient biofilms, reaching complete stress relaxation after 0.1 and 2 s on average for cellulose and pEtN-cellulose only (Fig. 27C). This stress-relaxation behaviour is comparable to that of viscoelastic fluids, which are capable to relax stresses on short time scales. Amyloid curli-producing biofilms reduce the normalized load to approximately 50 % on the same time scale (up to 2s). Wild-type biofilms containing both EPS components (AR3110) even retain on average 75% of the initial load, which represents a stress relaxation behaviour similar to that of brain tissue (Fig. 27C).[103] With such a time-dependent material behaviour, wild type *E. coli* biofilms can be described as viscoelastic solids, as they retain a plateau of residual loading even on longer time scales.

Yet, time scales observed in our experiments are still short and the viscoelastic behaviour is expected to be dominated by water flow especially at time < 1s. The consistently noticed local maximum in the load-time curves present for all biofilm samples at 350 ms we attribute to an initial tip instability when the tip switched from displacement-controlled indentation to constant displacement during the 10 s hold period. Compared to more elastic mammalian tissues (e.g. skin), all biofilms produced in this study should rather be considered as viscoelastic fluids than solids due to their higher water contents and ability of (re-)organization of the extracellular matrix fibre network.[103]

6.2 Discussion

E.coli AR3110 biofilms were previously described to exhibit tissue-like elasticity [23,25,26]. Here we quantified this observation at the micro-scale using a micro-indentation setup, and we confirmed that biofilms present rigidities in the range of a few hundred kPa when they contain amyloid curli fibres. Yet, characterizing the mechanical behaviour of biofilms grown from EPS-deficient *E. coli* strains, we showed that the presence of pEtN-modified cellulose, the second main EPS component, seems to confer the biofilm surface with decreased adhesive and increased solid-like behaviour, when co-expressed with amyloid curli from the same bacteria. This result strengthens the hypothesis that the combination of the two EPS matrix components amyloid curli and pEtN-cellulose, which co-assemble into a fibrous network, confer such biofilms with enhanced mechanical properties.[125] The rigid biofilms are then more prone to undergo mechanical instabilities and verticalization of single delaminated buckles.[29]

Upon combined expression of amyloid curli and pEtN-modified cellulose, accumulated dry mass of bacteria and EPS matrix increases. We attribute this behaviour of the wild type *E. coli* biofilms to their increased spreading along the solid-air interface, which provides them with a larger contact to the nutrient-rich substrate and favours their overall fitness.[60] Faster surface spreading was related to osmotic swelling of matrix-rich layers in *B. Subtilis* and *V. cholera* biofilms, which EPS mutants lack.[55,61] For *E. coli* biofilms, the combination of the two main EPS matrix components seems to be particularly advantageous for surface spreading and the formation of thin biofilms.[25]

Additionally, biofilms are known to regulate their water content by controlling the composition of the extracellular matrix and thereby influencing its mechanical properties.[40] In particular, the crosslink density of the EPS network sets a limit to the maximum water uptake of the biofilm.[40] The measured trends in *E. coli* biofilm water contents of mutant strains are limited. Still, the lower water content measured when amyloid curli and pEtN-modified cellulose are co-expressed by bacteria can hint at an increased crosslink density of the EPS fibre network. In contrast, the slightly higher water contents measured when no EPS or only one main component of the EPS is present, suggest a lower crosslink density. As the mechanical properties of a hydrogel at equilibrium are directly related to the water content, water content provides a means of controlling the mechanics of a biofilm.[40]

In mammalian tissues, elastic properties are known to depend on the composition and structure of the biological material (i.e. the fraction of cells and extracellular matrix, ECM). Here we build on this knowledge to assess the contribution of EPS components on native *E. coli* biofilms. An enhanced elasticity when co-expressing the two main EPS components was suggested, as pEtN-modified cellulose fibres were proposed to form a tight nanocomposite with amyloid curli fibres at the surface of *E. coli* AR3110 biofilms.[25,125] Yet, we don't find enhanced rigidities on a microscale when pEtN-modified cellulose is co-expressed with amyloid curli (AR3110) compared to exclusive expression of amyloid curli (W3110). Therefore, amyloid curli expression of *E. coli* cells seems to be sufficient to provide structural rigidity to the biofilm on a microscale. This conclusion is following a rheological study of *E. coli* MG1655, which suggests that biofilm mechanical behaviour is dominated by the presence of curli proteins.[122] However, we showed that pEtN-modified cellulose plays a role in biofilm surface adhesion and viscoelasticity, which suggests that its co-expression with rigid amyloid curli fibres may lead to a multifunctional composite material.

Crosslinked and semiflexible biopolymer networks (such as amyloid fibrils in biofilms) provide structural and adhesive properties to many biological and biomaterials.[148] Adhesion properties of polymer and biofilm surfaces were often characterized by measuring the maximum negative forces developed upon retraction of the tip from the sample after nano-indentation.[113,149] In contrast, here we measured adhesive energies (i.e. area under load-displacement curves upon retraction) as we observed extended negative displacements while maintaining similar negative forces upon retraction for different EPS-mutant strains (Fig. 27A).

At first, it seems counter-intuitive that curli-deficient strains present much higher adhesion energies than curli-producing strains providing the important role of curli fibres in biofilm adhesion.[150] Yet, the comparison of curli-containing and curli-deficient biofilms here may prove inadequate given that their mechanical rigidities differ by an order of magnitude. In addition to rigidity and adhesion, capillarity has a critical role when performing small scale indentations on soft material with Young's moduli below 100 kPa.[115]

Upon indentation, water is drawn out of the biofilm surface and can form a meniscus around the indenter. Increased contact area leads to increased surface stress, which needs to be overcome during the separation of the tip and the sample surface.[114] Because curli-producing biofilms are more rigid, here we expect adhesion and elasticity to be the main factors that

mediate the micro-contact upon loading and unloading. A lack of curli fibres in the biofilm renders its surface much more compliant and the spherical indenter contact might then be better described as adsorbed to a fluid interface.[114]

Viscoelastic fluid and solid-like mechanical behaviour of soft biological materials (e.g. cells and tissues) and biomaterials (e.g. hydrogels) can be characterized by their ability to relax introduced stresses.[103,151] We find the fastest average relaxation times (complete relaxation < 10 s) for biofilms grown from curli-deficient strains, i.e. producing only cellulose (AP472) or pEtN-cellulose (AP329) or no EPS (AR198). The EPS architecture of *E. coli* biofilms deficient in curli production is characterized by the assembly of loose sheets of cellulose fibres at the biofilm surface, which might be more prone to reassemble upon constant deformation.[25] In comparison, we detect slower relaxation times for biofilms grown from curli-producing strains (complete relaxation > 10 s). The EPS architecture of these biofilms encloses bacteria more tightly (W3110) or forms a dense EPS layer at the top (AR3110).[25] Such an increase in the amount of matrix production and a complex and dense EPS matrix architecture are suggested to improve the storage of elastic energy upon constant deformation on medium time scales (10 s). The combination of amyloid curli and pEtN-modified cellulose fibres (AR3110) shows the slowest relaxation times (retaining >50 % of load after 10 s), which points to the important role of the co-assembly of these two main EPS matrix components in determining the viscoelasticity of *E. coli* biofilms.

This work presents an overview of how an altered EPS composition affects the rigidity and viscoelasticity of *E. coli* biofilms. To measure the rigidity of the biofilm surface and its adhesive behaviour, the Johnson-Kendall-Roberts (JKR) theory or extended JKR models for adhesive contact between a spherical indenter and a soft biological material could be further used to account for the potential influence of adhesion and surface tension for micro contact mechanics.[112,115] *In situ* imaging of the contact interface and potential liquid meniscus formation by a combined confocal microscopy and micro-indentation setup would further help to understand the differences measured when indenting compliant (few kPa) versus more rigid (several hundred kPa) biofilm samples.

Besides changing EPS composition by growing biofilms from different *E. coli* strains, we also alter the complex EPS architecture at the biofilm surface.[25] The possibility to chemically extract the individual EPS components, i.e. amyloid curli and pEtN-modified cellulose, and manipulate

them apart from the bacteria is therefore expected to give a clearer understanding of how their co-assembly into a complex fibre network provides biofilms with enhanced rigidity, adhesion and viscoelasticity.[152] Additional bulk rheology measurements on biofilm material and nano-mechanical analyses of purified EPS or their gels by AFM would allow us to set our results in the context of a true multiscale mechanical characterization of *E. coli* biofilms.

6.3 Conclusion

In conclusion, we performed microscale mechanical testing on *E. coli* biofilms grown from various strains producing different EPS. The tissue-like elasticity of wild type *E. coli* biofilms was previously attributed to the co-assembly of amyloid curli and pEtN-cellulose fibres into a dense EPS network. Yet, we find that the presence of amyloid curli fibres seems to be sufficient to provide *E. coli* biofilms with increased rigidity upon compression. We further suggest that the role of the co-assembly of both fibres is to provide *E. coli* biofilms with enhanced viscoelastic solid-like behaviour and slow down the relaxation of introduced stresses. Their rigidity might be the main mechanical origin of the ability of *E. coli* AR3110 biofilms to form high-aspect ratio delaminated buckles out of mechanical instabilities. Taken together, the combination of amyloid curli and pEtN-modified fibres seems to form a composite material encasing *E. coli* AR3110 bacteria. While curli amyloid fibres provide rigid elements of the EPS fibre network, pEtN-modified cellulose fibres provide more compliant elements.

7 GENERAL DISCUSSION AND OUTLOOK

The overall purpose of this thesis was to investigate the processes involved in the formation of complex morphological structures during *E. coli* biofilm development, with a special focus on their growth dynamics, their adaptation to environmental stimuli and their mechanical properties. In the scope of this thesis, I first addressed how biological activity alters *E. coli* biofilm growth and morphogenesis. By using time-lapse fluorescence imaging, I investigated the spatiotemporal distribution of bacteria and EPS matrix production and their correlation with the emergence of mechanical instabilities. Moreover, embedding microparticles into the growing biofilms and the subsequent application of single-particle tracking algorithms enabled me to distinguish several kinematic stages during the early and late stages of *E. coli* biofilm development.

In a second project, I studied how *E. coli* biofilm morphology and mechanical properties adapt to an environmental parameter, namely the water content of their substrate. By employing time-lapse brightfield imaging, I found that substrates with high water content promote biofilm spreading, while they reduce the relative area of delaminated buckles. Gravimetric measurements also revealed higher dry masses and water contents for *E. coli* biofilms grown on substrates with high water content. In addition, such biofilms were found to be more compliant by an order of magnitude compared to biofilms grown on substrates with low water content as measured by micro-indentation.

In a third and final study, I estimated how the combination of the two main EPS fibres of *E. coli* biofilms, i.e. amyloid curli and pEtN-modified cellulose, contribute to the emergent biofilm mechanical properties. Micro-indentation measurements suggested that amyloid curli is sufficient to provide compressive rigidity to *E. coli* biofilms, while a lack of amyloid curli leads to larger adhesion energy and more viscoelastic fluid-like material properties.

7.1 Biofilm morphogenesis

Fundamental research on biofilm morphogenesis got increasing attention over the last decade.[19,20,30,70] The emergence of complex morphologies in a growing biofilm is attributed to the stratification of cell differentiation and EPS matrix expression due to external gradients of nutrient and oxygen availability from a microbiological viewpoint.[23,25,38] In contrast, from the

viewpoint of biomechanics, complex morphologies are described to emerge from mechanical instabilities influenced by non-uniform (or differential) growth, the mechanical properties of the biofilm and the substrate, and interfacial friction. While the heterogeneous distribution of cells and matrix, the non-uniform growth and the emergence of mechanical instabilities in biofilms were mostly studied separately, Chapter 4 of this thesis tried to bridge this gap.[19,36] Some modelling approaches do not account for the non-uniform thickness of biofilms and the non-uniform distribution of cells and matrix, nor their respective influence on the emerging morphologies.[20] Despite the extended periods of linear velocity profiles observed when studying biofilm movements, which suggest homogenous biofilm growth, *E. coli* AR3110 biofilms still show a transition from initial wrinkling to delaminated buckle instabilities. One possible reason resides in the limitation of our particle tracking method that only samples the central part of the biofilm and yields growth velocities projected in the plane parallel to the substrate. Such limitation might be overcome by using novel methods of wide-field 3D confocal imaging such as Mesolens systems.[46]

Nevertheless, by estimating biofilm spreading areas as presented in chapter 5, we can also infer a non-uniform growth behaviour as the biofilm projected area increase is accelerated in the early stage of biofilm development, whereas it becomes decelerated in a late stage.[136] Here, increasing the water content of the substrate may have also favoured the presence of an interfacial layer of water, thereby decreasing the friction (or tangential adhesion) of the biofilm onto the substrate.[142] In chapter 5 and 6, we could verify the theoretical assumption that a stiff film on a soft substrate is able to undergo a wrinkling instability when internal mechanical strains progressively increase due to continuous growth (stiffness ratio $\frac{\mu_F}{\mu_S} \sim \frac{E_F}{E_S}$ > 5 for all curli-producing biofilms).[29] In contrast, in chapter 6 we observe no morphological features for curli-deficient biofilms, while they appear much more compliant than their substrates ($\frac{\mu_F}{\mu_S} \sim \frac{E_F}{E_S}$ < 0.3 with $E_{1.8\%\,agar} = 60\ kPa$).

However, most theoretical modelling approaches for biofilm morphogenesis are limited when it comes to capture the emergence of mechanical rigidity over time and to account for the highly heterogeneous structure of the EPS fibre network that constitutes the matrix.[25,111] Despite using the same experimental conditions, variability in biofilm morphology is often observed from experiment to experiment or even from plate to plate within an experimental batch (even in the literature). However, biofilms grown with the same bacteria and within the

same plate show very similar growth pattern. These variations of behaviour are another evidence that biofilms are highly sensitive to their environment. We realized that the presence of water in the environment is the only parameter we could not control reliably during the different steps of the experiments. This observation actually motivated the work performed in chapter 5. These differences, readily visible in the morphology of the biofilm, indicate differences in one (or several) determinants of the morphology, namely growth, mechanical properties and/or the interfacial interactions between the biofilm and the substrate. Especially, studies focusing at the complex interrelationship of the three dominating parameters for the emergence of mechanical instabilities in correlation with biological activity inside a growing biofilm. A better understanding of complex morphogenesis programs in nature can further contribute to the design of living, autonomous and adaptive materials and soft robots.[65]

7.2 Biofilm material properties

The complex mechanical properties of biofilms result from their composite multi-scale structure.[10,27,40,100] Due to their high ability for water uptake, biofilms can be considered as biological hydrogels.[88] A key characteristic of hydrogels is their viscoelastic and therefore time-dependent mechanical behaviour. In chapter 6, we presented measured biofilm rigidities, adhesion energies between the indenter tip and the biofilms, and biofilm viscoelastic stress-relaxation over time, for all of which we obtained high standard deviations. Some variability can be attributed to the micro-indentation setup we used, as the displacement-controlled 'air indent' indentation mode proved suitable for the investigation of adhesion energies but controlling absolute displacement upon indentation was not possible. This limited precision in controlling tip-surface contact increases the variability of the mechanical measurements. However, the highly heterogeneous EPS architecture of *E. coli* biofilms also explains these high standard deviations for measured rigidities, adhesive energies and viscoelastic relaxation times.[129]

We have shown in chapters 5 and 6 that the amount, composition and asymmetric distribution of EPS matrix components inside *E. coli* biofilms impact the microscale rigidity of the biofilm surface. These findings are following previous microbiological studies on *E. coli* biofilms and support the proposed tissue-like elasticity with micromechanical parameters.[25,38,153] The formation of rigid curli fibres closely embedding bacteria also provides a rigid EPS network at

the microscale, which complements rheological studies finding similar results for bulk properties of *E. coli* biofilms.[25,122] Upon altered EPS composition, we further find changes in adhesion energy and viscoelasticity of the *E. coli* biofilm surface. Strong adhesion of the biofilm surface might aid the entrapment of other microorganisms or microparticles, which could serve to strengthen the biofilm or act as a nutrient supply.[154] While elasticity of the extracellular matrix of mammalian cells is well known to influence fundamental cellular processes,[155] matrix viscoelasticity has been implicated in remodelling the micro-environment of cells in confinement.[103] Viscoelasticity of the EPS network might play a similar role for bacterial cells. Upon growth and deformation of *E. coli* biofilms the EPS matrix network, especially in upper matrix-rich layers, also needs to undergo remodelling due to internal stresses.[28,149] Such local stress relaxation could be facilitated by the formation of transient crosslinks (e.g. by polyvalent ions).[156] Micro-rheological studies (e.g. by magnetic micro-particle actuation) investigating the movement of particles through the EPS network could further improve the knowledge about local viscoelasticity and its role for biofilm mechanics.[105]

Biofilm mechanics constitute a complex phenomenon involving elastic, plastic, adhesive and viscoelastic material properties at different length scales. Further fundamental mechanical studies of the multi-scale and multifunctional role of EPS networks in native biofilms or using simplified models made of purified EPS fibres and hydrogels are thus needed. This basic knowledge will further be crucial to target the prevention of biofilms and their application as bio-sourced protein and polysaccharide materials.

7.3 Implications for engineered living materials

In the context of the emerging field of engineered living materials, bacterial cells are seen as living factories for their ability to produce nano-fibre materials.[18] From the development of bio-cements with self-healing properties to gut mucosal patches potentially used against inflammatory bowel disease, bacteria are involved and engineered to produce specific protein and polysaccharide materials with tailored properties.[157] In chapter 5, we have shown how we can use the water content of the biofilm substrate to control the dry mass and the mechanical properties of the biofilm. This knowledge could potentially be of interest when upscaling the production of *E. coli* biofilms and their amyloid curli and modified cellulose components are intended. For such large-scale production, the mechanical properties and dry mass of different

EPS-deficient *E. coli* mutant strains would be of similar importance. However, this would require culturing of genetically modified organisms, whereby regulatory issues are still a barrier towards real-world applications of living materials.[18] Yet, amyloid curli and pEtN-modified cellulose materials remain of high interest. Indeed, curli nanofibers have been shown to self-assemble also from engineered CsgA fusion proteins expressed by *E. coli*, leading to the formation of an intact amyloid fibre network.[14] Our method of measuring adhesion or viscoelastic properties from micro-indentation experiments presented in chapter 6 could thus add to the toolbox of mechanical testing of engineered amyloid fibre networks (e.g. recently reported aquaplastics from engineered biofilms).[158]

Also the recent discovery, that common *E. coli* lab strains produce a naturally modified cellulose material (phosphoethanolamine-modified cellulose) opened many new directions of research in microbiology, biochemistry and materials science.[125,146] In chapter 6, we confirm its beneficial role in enhancing microscale material properties of the *E. coli* biofilm when co-expressed with amyloid curli fibres. However, fundamental questions of the chemical and physical properties of pEtN-cellulose remains open, as well as their potential implication for tissue engineering and biotechnology.[146]

Conclusively, the two main EPS matrix components present in *E. coli* biofilms constitute promising fibrous biomaterials. In the field of engineered living materials, they can further be functionalized with the tools of synthetic biology, which are expected to yield new living materials.[14] However, besides bottom-up approaches of genetic modification, top-down approaches consisting of (I) engineering the environment of bacteria by charged surfaces, water or mineralizing media and (II) by processing EPS matrix components by ionic solutions or drying, we expect further interesting scientific questions to emerge in the field of biofilm research.

8 CONCLUSIONS

The present thesis focused on the emergence of complex structures during *E. coli* biofilm morphogenesis by understanding the influence of its growth dynamics and mechanical properties. A literature survey showed that biofilm morphogenesis is promoted by the spatiotemporal non-uniform distribution of cells and EPS matrix and can be modelled by the physical parameters of growth, stiffness ratio between biofilm and substrate and their adhesion (Chapter 2). The emergence of the mechanical properties of *E. coli* biofilms was further attributed to their heterogeneous and asymmetric EPS matrix composition and architecture (Chapter 2). However, biofilms provide living biological systems and their ability to undergo morphogenesis and their material properties are interrelated, which complicates the design and generalization of experimental findings. I thus tackled the question with an interdisciplinary approach combining bacterial culture, microscopy, computational image processing and mechanical characterization methods (Chapter 3). This strategy allowed me to address three main questions and draw conclusions relative to each of them.

- How does biological activity in *E. coli* biofilms grown at the solid-air interface alters their growth and morphogenesis on a macroscopic scale? (Chapter 4)

  - Non-uniform distributions of bacterial cells and EPS matrix precede mechanical instability patterns during *E. coli* biofilm morphogenesis.
  - Initial movements at the biofilm annular periphery slow down due to local confinement of the bacteria micro-environment before overall macroscopic biofilm spreading is initialized.
  - *E. coli* biofilm expansion follows four kinematic stages during biofilm morphogenesis.
  - Biofilm growth mechanics in the late stage of biofilm morphogenesis involves large compressive strains along the developing delaminated buckles with the potential to deform the underlying soft substrate.

- How do *E. coli* biofilm morphogenesis and mechanical properties adapt to an environmental parameter? Here, the water content of the substrate (Chapter 5).

  - Substrates with high water content promote biofilm spreading kinetics while substrates with low water content promote biofilm buckling in the third dimension.
  - Substrates with high water content increase the amount of accumulated biomass and the water content of *E. coli* biofilms, while the asymmetric cross-sectional distribution and heterogeneity of EPS matrix components become altered.
  - Biofilms are stiffer when grown on substrates with low water content.
  - Substrates with high water content are proposed to favour cell proliferation, whereas substrates with low water content are proposed to produce larger amounts and a thicker top layer of EPS matrix components.

- How do the main components of the EPS matrix of *E. coli* biofilms contribute to the emergent biofilm mechanical properties at the microscale? (Chapter 6)

  - Amyloid curli expression in monoclonal and mixed-species *E. coli* biofilms leads to larger spreading diameters and dry mass, reduced water content of the biofilm and the potential to form morphological structures.
  - Amyloid curli fibres provide *E. coli* biofilms with a rigidity of a few hundred kPa and lower adhesion energy, while a lack of amyloid curli fibres is associated with high compliance and stickiness.
  - Amyloid curli fibres decrease the adhesion energy of the *E. coli* biofilm surface
  - Amyloid curli fibres confer *E. coli* biofilms with more viscoelastic solid-like behaviour, while a lack of curli fibres generates viscoelastic fluid-like material properties.

I finished the work of this thesis with a general discussion of its results for their implications in the field of biofilm morphogenesis, biofilm mechanics and biofilm mechanical properties (Chapter 7). Future applied biofilm research can be directed towards applying the *E. coli* two main EPS components of amyloid curli and (pEtN)-modified cellulose for tissue engineering or engineered living materials applications.

REFERENCES

1. Hug, L. A., Baker, B. J., Anantharaman, K., Brown, C. T., Probst, A. J., Castelle, C. J., Butterfield, C. N., Hernsdorf, A. W., Amano, Y., Ise, K., Suzuki, Y., Dudek, N., Relman, D. A., Finstad, K. M., Amundson, R., Thomas, B. C. & Banfield, J. F. A new view of the tree of life. *Nature Microbiology 2016 1:5* (2016) *1*, 1–6.
2. Schopf, J. W. & Packer, B. M. Early Archean (3.3-billion to 3.5-billion-year-old) microfossils from Warrawoona Group, Australia. *Science (New York, N.Y.)* (1987) *237*, 70–73.
3. Flemming, H. C. & Wingender, J. The biofilm matrix. *Nature Reviews Microbiology 2010 8:9* (2010) *8*, 623–633.
4. Flemming, H. C. Eps—then and now. *Microorganisms* (2016) vol. 4 41.
5. Flemming, H. C. & Wingender, J. The biofilm matrix. *Nature Reviews Microbiology* (2010) *8*, 623–633.
6. Hartmann, R., Singh, P. K., Pearce, P., Mok, R., Song, B., Díaz-Pascual, F., Dunkel, J. & Drescher, K. Emergence of three-dimensional order and structure in growing biofilms. *Nature Physics* (2019) *15*, 251–256.
7. Arnaouteli, S., Bamford, N. C., Stanley-Wall, N. R. & Kovács, Á. T. Bacillus subtilis biofilm formation and social interactions. *Nature Reviews Microbiology* (2021) *19*, 600–614.
8. Sharma, G., Sharma, S., Sharma, P., Chandola, D., Dang, S., Gupta, S. & Gabrani, R. Escherichia coli biofilm: development and therapeutic strategies. *Journal of Applied Microbiology* (2016) *121*, 309–319.
9. Percival, S. L., Malic, S., Cruz, H., Williams, D. W., Percival, S. L., Malic, S., Williams, • D W & Cruz, H. Introduction to Biofilms. *Springer Series on Biofilms* (2011) *6*, 41–68.
10. Yan, J., Moreau, A., Khodaparast, S., Perazzo, A., Feng, J., Fei, C., Mao, S., Mukherjee, S., Košmrlj, A., Wingreen, N. S., Bassler, B. L., Stone, H. A., Yan, J., Moreau, A., Khodaparast, S., Perazzo, A., Feng, J., Mao, S., Košmrlj, A., Stone, H. A., Fei, C., Mukherjee, S., Wingreen, N. S. & Bassler, B. L. Bacterial Biofilm Material Properties Enable Removal and Transfer by Capillary Peeling. *Advanced Materials* (2018) *30*, 1804153.
11. Nerenberg, R. The membrane-biofilm reactor (MBfR) as a counter-diffusional biofilm process. *Current Opinion in Biotechnology* (2016) *38*, 131–136.
12. Roberson, E. B. & Firestone, M. K. Relationship between desiccation and exopolysaccharide production in a soil Pseudomonas sp. *Applied and Environmental Microbiology* (1992) *58*, 1284–1291.
13. Hufnagel, D. A., Depas, W. H. & Chapman, M. R. The Biology of the Escherichia coli Extracellular Matrix . *Microbiology Spectrum* (2015) *3*, 1–24.
14. Nguyen, P. Q., Botyanszki, Z., Tay, P. K. R. & Joshi, N. S. Programmable biofilm-based materials from engineered curli nanofibres. *Nature Communications* (2014) *5*, 1–10.
15. Zhang, C., Huang, J., Zhang, J., Liu, S., Cui, M., An, B., Wang, X., Pu, J., Zhao, T., Fan, C., Lu, T. K. & Zhong, C. Engineered Bacillus subtilis biofilms as living glues. *Materials Today* (2019) *28*, 40–48.
16. Praveschotinunt, P., Duraj-Thatte, A. M., Gelfat, I., Bahl, F., Chou, D. B. & Joshi, N. S. Engineered E. coli Nissle 1917 for the delivery of matrix-tethered therapeutic domains to the gut. *Nature Communications 2019 10:1* (2019) *10*, 1–14.
17. Gilbert, C., Tang, T. C., Ott, W., Dorr, B. A., Shaw, W. M., Sun, G. L., Lu, T. K. & Ellis, T. Living materials with programmable functionalities grown from engineered microbial co-

cultures. *Nature Materials* (2021).
18. Nguyen, P. Q., Courchesne, N. M. D., Duraj-Thatte, A., Praveschotinunt, P. & Joshi, N. S. Engineered Living Materials: Prospects and Challenges for Using Biological Systems to Direct the Assembly of Smart Materials. *Advanced Materials* (2018) *30*, 1–34.
19. Yan, J., Fei, C., Mao, S., Moreau, A., Wingreen, N. S., Košmrlj, A., Stone, H. A. & Bassler, B. L. Mechanical instability and interfacial energy drive biofilm morphogenesis. *eLife* (2019) *8*, 1–28.
20. Fei, C., Mao, S., Yan, J., Alert, R., Stone, H. A., Bassler, B. L., Wingreen, N. S. & Košmrlj, A. Nonuniform growth and surface friction determine bacterial biofilm morphology on soft substrates. *Proceedings of the National Academy of Sciences of the United States of America* (2020) *117*, 7622–7632.
21. Shapiro, J. A. THINKING ABOUT BACTERIAL POPULATIONS AS MULTICELLULAR ORGANISMS. *https://doi.org/10.1146/annurev.micro.52.1.81* (2003) *52*, 81–104.
22. Collinet, C. & Lecuit, T. Programmed and self-organized flow of information during morphogenesis. *Nature Reviews Molecular Cell Biology* (2021) *22*, 245–265.
23. Serra, D. O. & Hengge, R. Stress responses go three dimensional - The spatial order of physiological differentiation in bacterial macrocolony biofilms. *Environmental Microbiology* (2014) *16*, 1455–1471.
24. Klauck, G., Serra, D. O., Possling, A. & Hengge, R. Spatial organization of different sigma factor activities and c-di-GMP signalling within the three-dimensional landscape of a bacterial biofilm. *Open Biology* (2018) *8*,.
25. Serra, D. O., Richter, A. M. & Hengge, R. Cellulose as an architectural element in spatially structured escherichia coli biofilms. *Journal of Bacteriology* (2013) *195*, 5540–5554.
26. Serra, D. O., Klauck, G. & Hengge, R. Vertical stratification of matrix production is essential for physical integrity and architecture of macrocolony biofilms of Escherichia coli. *Environmental Microbiology* (2015) *17*, 5073–5088.
27. Tallawi, M., Opitz, M. & Lieleg, O. Modulation of the mechanical properties of bacterial biofilms in response to environmental challenges. *Biomaterials Science* (2017) *5*, 887–900.
28. Rode, D. K. H., Singh, P. K. & Drescher, K. Multicellular and unicellular responses of microbial biofilms to stress. *Biological Chemistry* (2020) *401*, 1365–1374.
29. Wang, Q. & Zhao, X. A three-dimensional phase diagram of growth-induced surface instabilities. *Scientific Reports* (2015) *5*, 1–10.
30. Zhang, C., Li, B., Huang, X., Ni, Y. & Feng, X. Q. Morphomechanics of bacterial biofilms undergoing anisotropic differential growth. *Applied Physics Letters* (2016) *109*,.
31. Rumbaugh, K. P. & Sauer, K. Biofilm dispersion. *Nature Reviews Microbiology* (2020) vol. 18 571–586.
32. Flemming, H. C., Wingender, J., Szewzyk, U., Steinberg, P., Rice, S. A. & Kjelleberg, S. Biofilms: an emergent form of bacterial life. *Nature Reviews Microbiology 2016 14:9* (2016) *14*, 563–575.
33. Koo, H., Allan, R. N., Howlin, R. P., Stoodley, P. & Hall-Stoodley, L. Targeting microbial biofilms: Current and prospective therapeutic strategies. *Nature Reviews Microbiology* (2017) vol. 15 740–755.
34. Valentini, M. & Filloux, A. Biofilms and Cyclic di-GMP (c-di-GMP) signaling: Lessons from Pseudomonas aeruginosa and other bacteria. *Journal of Biological Chemistry* (2016) *291*, 12547–12555.
35. Yan, J. & Bassler, B. L. Surviving as a Community: Antibiotic Tolerance and Persistence in

Bacterial Biofilms. *Cell Host and Microbe* (2019) *26*, 15–21.
36. Srinivasan, S., Vladescu, I. D., Koehler, S. A., Wang, X., Mani, M. & Rubinstein, S. M. Matrix Production and Sporulation in Bacillus subtilis Biofilms Localize to Propagating Wave Fronts. *Biophysical Journal* (2018) vol. 114 1490–1498.
37. Sutherland, I. W. The biofilm matrix – an immobilized but dynamic microbial environment. *Trends in Microbiology* (2001) *9*, 222–227.
38. Serra, D. O. & Hengge, R. Annual Review of Microbiology Bacterial Multicellularity: The Biology of Escherichia coli Building Large-Scale Biofilm Communities. (2021).
39. Srinivasan, S., Nadir Kaplan, C. & Mahadevan, L. A multiphase theory for spreading microbial swarms and films. *eLife* (2019) *8*, 1–28.
40. Wilking, J. N., Angelini, T. E., Seminara, A., Brenner, M. P. & Weitz, D. A. Biofilms as complex fluids. *MRS Bulletin* (2011) *36*, 385–391.
41. Seminara, A., Angelini, T. E., Wilking, J. N., Vlamakis, H., Ebrahim, S., Kolter, R., Weitz, D. A. & Brenner, M. P. Osmotic spreading of Bacillus subtilis biofilms driven by an extracellular matrix. *Proceedings of the National Academy of Sciences of the United States of America* (2012) *109*, 1116–1121.
42. Billings, N., Ramirez Millan, M., Caldara, M., Rusconi, R., Tarasova, Y., Stocker, R. & Ribbeck, K. The Extracellular Matrix Component Psl Provides Fast-Acting Antibiotic Defense in Pseudomonas aeruginosa Biofilms. *PLOS Pathogens* (2013) *9*, e1003526.
43. Jeckel, H., Jelli, E., Hartmann, R., Singh, P. K., Mok, R., Totz, J. F., Vidakovic, L., Eckhardt, B., Dunkel, J. & Drescher, K. Learning the space-time phase diagram of bacterial swarm expansion. *Proceedings of the National Academy of Sciences of the United States of America* (2019) *116*, 1489–1494.
44. Beroz, F., Yan, J., Meir, Y., Sabass, B., Stone, H. A., Bassler, B. L. & Wingreen, N. S. Verticalization of bacterial biofilms. *Nature Physics* (2018) *14*, 954–960.
45. Duvernoy, M.-C., Mora, T., Ardré, M., Croquette, V., Bensimon, D., Quilliet, C., Ghigo, J.-M., Beloin, C., Lecuyer, S. & Desprat, N. Asymmetric adhesion of rod-shaped bacteria controls microcolony morphogenesis.
46. Rooney, L. M., Amos, W. B., Hoskisson, P. A. & McConnell, G. Intra-colony channels in E. coli function as a nutrient uptake system. *The ISME Journal 2020 14:10* (2020) *14*, 2461–2473.
47. Asally, M., Kittisopikul, M., Rué, P., Du, Y., Hu, Z., Çağatay, T., Robinson, A. B., Lu, H., Garcia-Ojalvo, J. & Süel, G. M. Localized cell death focuses mechanical forces during 3D patterning in a biofilm. *Proceedings of the National Academy of Sciences of the United States of America* (2012) *109*, 18891–18896.
48. Campàs, O. A toolbox to explore the mechanics of living embryonic tissues. *Seminars in Cell and Developmental Biology* (2016) *55*, 119–130.
49. Blanchard, G. B., Kabla, A. J., Schultz, N. L., Butler, L. C., Sanson, B., Gorfinkiel, N., Mahadevan, L. & Adams, R. J. Tissue tectonics: Morphogenetic strain rates, cell shape change and intercalation. *Nature Methods* (2009) *6*, 458–464.
50. Bidan, C. M., Fratzl, M., Coullomb, A., Moreau, P., Lombard, A. H., Wang, I., Balland, M., Boudou, T., Dempsey, N. M., Devillers, T. & Dupont, A. Magneto-active substrates for local mechanical stimulation of living cells. *Scientific Reports 2018 8:1* (2018) *8*, 1–13.
51. Tseng, Q., Wang, I., Duchemin-Pelletier, E., Azioune, A., Carpi, N., Gao, J., Filhol, O., Piel, M., Théry, M. & Balland, M. A new micropatterning method of soft substrates reveals that different tumorigenic signals can promote or reduce cell contraction levels. *Lab on a Chip* (2011) *11*, 2231–2240.

52. Wang, X., Koehler, S. A., Wilking, J. N., Sinha, N. N., Cabeen, M. T., Srinivasan, S., Seminara, A., Rubinstein, S., Sun, Q., Brenner, M. P. & Weitz, D. A. Probing phenotypic growth in expanding Bacillus subtilis biofilms. *Applied Microbiology and Biotechnology* (2016) *100*, 4607–4615.
53. Wang, X., Kong, Y., Zhao, H. & Yan, X. Dependence of the Bacillus subtilis biofilm expansion rate on phenotypes and the morphology under different growing conditions. *Development Growth and Differentiation* (2019) *61*, 431–443.
54. Hamouche, L., Laalami, S., Daerr, A., Song, S., Holland, I. B., Séror, S. J., Hamze, K. & Putzer, H. Bacillus subtilis Swarmer Cells Lead the Swarm, Multiply, and Generate a Trail of Quiescent Descendants. *mBio* (2017) *8*,.
55. Yan, J., Nadell, C. D., Stone, H. A., Wingreen, N. S. & Bassler, B. L. Extracellular-matrix-mediated osmotic pressure drives Vibrio cholerae biofilm expansion and cheater exclusion. *Nature Communications 2017 8:1* (2017) *8*, 1–11.
56. Boudarel, H., Mathias, J. D., Blaysat, B. & Grédiac, M. Towards standardized mechanical characterization of microbial biofilms: analysis and critical review. *npj Biofilms and Microbiomes 2018 4:1* (2018) *4*, 1–15.
57. De Beer, D. & Van Den Heuvel, J. C. Gradients in immobilized biological systems. *Analytica Chimica Acta* (1988) *213*, 259–265.
58. de Beer, D., Stoodley, P., Roe, F. & Lewandowski, Z. Effects of biofilm structures on oxygen distribution and mass transport. *Biotechnology and Bioengineering* (1994) *43*, 1131–1138.
59. Watnick, P. I. & Kolter, R. Steps in the development of a Vibrio cholerae El Tor biofilm. *Molecular Microbiology* (1999) *34*, 586–595.
60. Yan, J., Nadell, C. D., Stone, H. A., Wingreen, N. S. & Bassler, B. L. Extracellular-matrix-mediated osmotic pressure drives Vibrio cholerae biofilm expansion and cheater exclusion. *Nature Communications* (2017) *8*,.
61. Seminara, A., Angelini, T. E., Wilking, J. N., Vlamakis, H., Ebrahim, S., Kolter, R., Weitz, D. A. & Brenner, M. P. Osmotic spreading of Bacillus subtilis biofilms driven by an extracellular matrix. *Proceedings of the National Academy of Sciences of the United States of America* (2012) *109*, 1116–1121.
62. Trinschek, S., John, K. & Thiele, U. From a thin film model for passive suspensions towards the description of osmotic biofilm spreading. *AIMS Materials Science* (2016) *3*, 1138–1159.
63. Serra, D. O., Richter, A. M. & Hengge, R. Cellulose as an architectural element in spatially structured escherichia coli biofilms. *Journal of Bacteriology* (2013) *195*, 5540–5554.
64. Thompson, D. W. *On Growth and Form*. (Cambridge University Press, 1992).
65. Huang, C., Wang, Z., Quinn, D., Suresh, S. & Jimmy Hsia, K. Differential growth and shape formation in plant organs. *Proceedings of the National Academy of Sciences of the United States of America* (2018) *115*, 12359–12364.
66. Savin, T., Kurpios, N. A., Shyer, A. E., Florescu, P., Liang, H., Mahadevan, L. & Tabin, C. J. On the growth and form of the gut. *Nature 2011 476:7358* (2011) *476*, 57–62.
67. Hill, R. S. & Walsh, C. A. Molecular insights into human brain evolution. *Nature 2005 437:7055* (2005) *437*, 64–67.
68. Brau, F., Damman, P., Diamant, H. & Witten, T. A. Wrinkle to fold transition: Influence of the substrate response. *Soft Matter* (2013) *9*, 8177–8186.
69. Beyhan, S. & Yildiz, F. H. Smooth to rugose phase variation in Vibrio cholerae can be mediated by a single nucleotide change that targets c-di-GMP signalling pathway.

Molecular Microbiology (2007) *63*, 995–1007.
70. Zhang, C., Li, B., Tang, J. Y., Wang, X. L., Qin, Z. & Feng, X. Q. Experimental and theoretical studies on the morphogenesis of bacterial biofilms. *Soft Matter* (2017) *13*, 7389–7397.
71. Li, B., Cao, Y. P., Feng, X. Q. & Gao, H. Mechanics of morphological instabilities and surface wrinkling in soft materials: a review. *Soft Matter* (2012) *8*, 5728–5745.
72. Trepat, X. & Sahai, E. Mesoscale physical principles of collective cell organization. *Nature Physics* (2018) *14*, 671–682.
73. Budday, S., Andres, S., Bastianwalter, Steinmann, P. & Kuhl, E. Wrinkling instabilities in soft bilayered systems. *Philosophical Transactions of the Royal Society A: Mathematical, Physical and Engineering Sciences* (2017) *375*,.
74. Kothari, M., Lemon, Z., Roth, C. & Cohen, T. Controlled propagation and jamming of a delamination front. *Soft Matter* (2020) *16*, 9838–9843.
75. Cooper, A. L., Dean, A. C. & Hinshelwood, C. Factors affecting the growth of bacterial colonies on agar plates. *Proceedings of the Royal Society of London. Series B. Biological sciences* (1968) *171*, 175–199.
76. Matsushita, M., Wakita, J., Itoh, H., Watanabe, K., Arai, T., Matsuyama, T., Sakaguchi, H. & Mimura, M. Formation of colony patterns by a bacterial cell population. *Physica A: Statistical Mechanics and its Applications* (1999) *274*, 190–199.
77. References Botts, J., Morales, M. F., Kielley, W. W., Kielley, R. K., Nordlie, R. C., Fromm, H. J. & Zewe, V. Diffusion Measurements in Agar Gel. *Trans. Faraday Soc* (1953) *49*, 1668.
78. Bae, E., Aroonnual, A., Bhunia, A. K. & Hirleman, E. D. On the sensitivity of forward scattering patterns from bacterial colonies to media composition. *Journal of Biophotonics* (2011) *4*, 236–243.
79. Zhang, W., Seminara, A., Suaris, M., Brenner, M. P., Weitz, D. A. & Angelini, T. E. Nutrient depletion in Bacillus subtilis biofilms triggers matrix production. *New Journal of Physics* (2014) *16*,.
80. Yan, J., Moreau, A., Khodaparast, S., Perazzo, A., Feng, J., Fei, C., Mao, S., Mukherjee, S., Košmrlj, A., Wingreen, N. S., Bassler, B. L. & Stone, H. A. Bacterial Biofilm Material Properties Enable Removal and Transfer by Capillary Peeling. *Advanced Materials* (2018) *30*, 1–10.
81. Wilking, J. N., Zaburdaev, V., De Volder, M., Losick, R., Brenner, M. P. & Weitz, D. A. Liquid transport facilitated by channels in Bacillus subtilis biofilms. *Proceedings of the National Academy of Sciences of the United States of America* (2013) *110*, 848–852.
82. Asp, M., Thanh, M. T. H., Gopinath, A. & Patteson, A. How do biofilms feel their environment? *bioRxiv* (2021) 2021.03.15.435407.
83. Zhang, W., Dai, W., Tsai, S. M., Zehnder, S. M., Sarntinoranont, M. & Angelini, T. E. Surface indentation and fluid intake generated by the polymer matrix of Bacillus subtilis biofilms. *Soft Matter* (2015) *11*, 3612–3617.
84. Angelini, T. E., Roper, M., Kolter, R., Weitz, D. A. & Brenner, M. P. Bacillus subtilis spreads by surfing on waves of surfactant. *Proceedings of the National Academy of Sciences* (2009) *106*, 18109–18113.
85. Trinschek, S., John, K., Lecuyer, S. & Thiele, U. Continuous versus Arrested Spreading of Biofilms at Solid-Gas Interfaces: The Role of Surface Forces. *Physical Review Letters* (2017) *119*, 1–5.
86. Ryzhkov, N. V., Nikitina, A. A., Fratzl, P., Bidan, C. M. & Skorb, E. V. Polyelectrolyte Substrate Coating for Controlling Biofilm Growth at Solid–Air Interface. *Advanced Materials Interfaces* (2021) *8*,.

87. Wolcott, R. D., Rumbaugh, K. P., James, G., Schultz, G., Phillips, P., Yang, Q., Waiters, C., Stewart, P. S. & Dowd, S. E. Biofilm maturity studies indicate sharp debridement opens a time-dependent therapeutic window. *http://dx.doi.org/10.12968/jowc.2010.19.8.77709* (2013) *19*, 320–328.
88. Lieleg, O. & Ribbeck, K. Biological hydrogels as selective diffusion barriers. *Trends in Cell Biology* (2011) *21*, 543–551.
89. Ido, N., Lybman, A., Hayet, S., Azulay, D. N., Ghrayeb, M., Liddawieh, S. & Chai, L. Bacillus subtilis biofilms characterized as hydrogels. Insights on water uptake and water binding in biofilms. *Soft Matter* (2020) *16*, 6180–6190.
90. Peterson, B. W., He, Y., Ren, Y., Zerdoum, A., Libera, M. R., Sharma, P. K., van Winkelhoff, A. J., Neut, D., Stoodley, P., van der Mei, H. C. & Busscher, H. J. Viscoelasticity of biofilms and their recalcitrance to mechanical and chemical challenges. *FEMS Microbiology Reviews* (2015) *39*, 234–245.
91. Even, C., Marlière, C., Ghigo, J. M., Allain, J. M., Marcellan, A. & Raspaud, E. Recent advances in studying single bacteria and biofilm mechanics. *Advances in Colloid and Interface Science* (2017) *247*, 573–588.
92. Peterson, B. W., van der Mei, H. C., Sjollema, J., Busscher, H. J. & Sharma, P. K. A distinguishable role of eDNA in the viscoelastic relaxation of biofilms. *mBio* (2013) *4*,.
93. Rupp, C. J., Fux, C. A. & Stoodley, P. Viscoelasticity of Staphylococcus aureus biofilms in response to fluid shear allows resistance to detachment and facilitates rolling migration. *Applied and Environmental Microbiology* (2005) *71*, 2175–2178.
94. Gordon, V. D., Davis-Fields, M., Kovach, K. & Rodesney, C. A. Biofilms and mechanics: a review of experimental techniques and findings. *Journal of Physics D: Applied Physics* (2017) *50*, 223002.
95. Tuson, H. H., Auer, G. K., Renner, L. D., Hasebe, M., Tropini, C., Salick, M., Crone, W. C., Gopinathan, A., Huang, K. C. & Weibel, D. B. Measuring the stiffness of bacterial cells from growth rates in hydrogels of tunable elasticity. *Molecular Microbiology* (2012) *84*, 874–891.
96. Kovach, K., Davis-Fields, M., Irie, Y., Jain, K., Doorwar, S., Vuong, K., Dhamani, N., Mohanty, K., Touhami, A. & Gordon, V. D. Evolutionary adaptations of biofilms infecting cystic fibrosis lungs promote mechanical toughness by adjusting polysaccharide production. *npj Biofilms and Microbiomes 2017 3:1* (2017) *3*, 1–9.
97. Cao, H., Habimana, O., Safari, A., Heffernan, R., Dai, Y. & Casey, E. Revealing region-specific biofilm viscoelastic properties by means of a micro-rheological approach. *npj Biofilms and Microbiomes 2016 2:1* (2016) *2*, 1–7.
98. Cense, A. W., Peeters, E. A. G., Gottenbos, B., Baaijens, F. P. T., Nuijs, A. M. & van Dongen, M. E. H. Mechanical properties and failure of Streptococcus mutans biofilms, studied using a microindentation device. *Journal of Microbiological Methods* (2006) *67*, 463–472.
99. Gordon, V. D., Davis-Fields, M., Kovach, K. & Rodesney, C. A. Biofilms and mechanics: A review of experimental techniques and findings. *Journal of Physics D: Applied Physics* (2017) *50*, aa6b83.
100. Gloag, E. S., Fabbri, S., Wozniak, D. J. & Stoodley, P. Biofilm mechanics: Implications in infection and survival. *Biofilm* (2020) *2*,.
101. Rmaile, A., Carugo, D., Capretto, L., Zhang, X., Wharton, J. A., Thurner, P. J., Aspiras, M., Ward, M. & Stoodley, P. Microbial tribology and disruption of dental plaque bacterial biofilms. *Wear* (2013) *306*, 276–284.

102. Islam, M. R. & Oyen, M. L. A poroelastic master curve for time-dependent and multiscale mechanics of hydrogels. *Journal of Materials Research* (2020).
103. Chaudhuri, O., Cooper-White, J., Janmey, P. A., Mooney, D. J. & Shenoy, V. B. Effects of extracellular matrix viscoelasticity on cellular behaviour. *Nature* (2020) *584*, 535–546.
104. Allen, A., Habimana, O. & Casey, E. The effects of extrinsic factors on the structural and mechanical properties of Pseudomonas fluorescens biofilms: A combined study of nutrient concentrations and shear conditions. *Colloids and Surfaces B: Biointerfaces* (2018) *165*, 127–134.
105. Galy, O., Latour-Lambert, P., Zrelli, K., Ghigo, J. M., Beloin, C. & Henry, N. Mapping of bacterial biofilm local mechanics by magnetic microparticle actuation. *Biophysical Journal* (2012) *103*, 1400–1408.
106. Grumbein, S., Opitz, M. & Lieleg, O. Selected metal ions protect Bacillus subtilis biofilms from erosion. *Metallomics* (2014) *6*, 1441–1450.
107. Safari, A., Tukovic, Z., Walter, M., Casey, E. & Ivankovic, A. Mechanical properties of a mature biofilm from a wastewater system: from microscale to macroscale level. *Biofouling* (2015) *31*, 651–664.
108. Pavlovsky, L., Younger, J. G. & Solomon, M. J. In situ rheology of Staphylococcus epidermidis bacterial biofilms. *Soft Matter* (2012) *9*, 122–131.
109. Kretschmer, M., Schüßler, C. A. & Lieleg, O. Biofilm Adhesion to Surfaces is Modulated by Biofilm Wettability and Stiffness. *Advanced Materials Interfaces* (2021) *8*,.
110. Briscoe, B. J., Fiori, L. & Pelillo, E. Nano-indentation of polymeric surfaces. *Journal of Physics D: Applied Physics* (1998) *31*, 2395–2405.
111. Kreis, C. T. & Sullan, R. M. A. Interfacial nanomechanical heterogeneity of the E. coli biofilm matrix. *Nanoscale* (2020) *12*, 16819–16830.
112. Ebenstein, D. M. Nano-JKR force curve method overcomes challenges of surface detection and adhesion for nanoindentation of a compliant polymer in air and water. *Journal of Materials Research* (2011) *26*, 1026–1035.
113. Kohn, J. C. & Ebenstein, D. M. Eliminating adhesion errors in nanoindentation of compliant polymers and hydrogels. *Journal of the Mechanical Behavior of Biomedical Materials* (2013) *20*, 316–326.
114. Style, R. W., Hyland, C., Boltyanskiy, R., Wettlaufer, J. S. & Dufresne, E. R. Surface tension and contact with soft elastic solids. *Nature Communications 2013 4:1* (2013) *4*, 1–6.
115. Pham, J. T., Schellenberger, F., Kappl, M. & Butt, H. J. From elasticity to capillarity in soft materials indentation. *Physical Review Materials* (2017) *1*, 4–6.
116. Huang, J., Liu, S., Zhang, C., Wang, X., Pu, J., Ba, F., Xue, S., Ye, H., Zhao, T., Li, K., Wang, Y., Zhang, J., Wang, L., Fan, C., Lu, T. K. & Zhong, C. Programmable and printable Bacillus subtilis biofilms as engineered living materials. *Nature Chemical Biology* (2019) *15*, 34–41.
117. Rossi, E., Cimdins, A., Lüthje, P., Brauner, A., Sjöling, Å., Landini, P. & Römling, U. "It's a gut feeling"–Escherichia coli biofilm formation in the gastrointestinal tract environment. *Critical Reviews in Microbiology* (2018) *44*, 1–30.
118. Croxen, M. A. & Finlay, B. B. Molecular mechanisms of Escherichia coli pathogenicity. *Nature Reviews Microbiology* (2010) vol. 8 26–38.
119. Cegelski, L., Pinkner, J. S., Hammer, N. D., Cusumano, C. K., Hung, C. S., Chorell, E., Åberg, V., Walker, J. N., Seed, P. C., Almqvist, F., Chapman, M. R. & Hultgren, S. J. Small-molecule inhibitors target Escherichia coli amyloid biogenesis and biofilm formation. *Nature Chemical Biology 2009 5:12* (2009) *5*, 913–919.

120. MacArisin, D., Patel, J., Bauchan, G., Giron, J. A. & Sharma, V. K. Role of curli and cellulose expression in adherence of escherichia coli O157:H7 to spinach leaves. *Foodborne Pathogens and Disease* (2012) *9*, 160–167.
121. Bokranz, W., Wang, X., Tschäpe, H. & Römling, U. Expression of cellulose and curli fimbriae by Escherichia coli isolated from the gastrointestinal tract. *Journal of Medical Microbiology* (2005) *54*, 1171–1182.
122. Horvat, M., Pannuri, A., Romeo, T., Dogsa, I. & Stopar, D. Viscoelastic response of Escherichia coli biofilms to genetically altered expression of extracellular matrix components. *Soft Matter* (2019) *15*, 5042–5051.
123. Barnhart, M. M. & Chapman, M. R. Curli biogenesis and function. *Annual review of microbiology* (2006) *60*, 131–147.
124. Ogasawara, H., Yamamoto, K. & Ishihama, A. Role of the biofilm master regulator CsgD in cross-regulation between biofilm formation and flagellar synthesis. *Journal of Bacteriology* (2011) *193*, 2587–2597.
125. Thongsomboon, W., Serra, D. O., Possling, A., Hadjineophytou, C., Hengge, R. & Cegelski, L. Phosphoethanolamine cellulose: A naturally produced chemically modified cellulose. *Science* (2018) *338*, 334–338.
126. Serra, D. O. & Hengge, R. *Cellulose in Bacterial Biofilms*. (2019).
127. Jeffries, J., Thongsomboon, W., Visser, J. A., Enriquez, K., Yager, D. & Cegelski, L. Variation in the ratio of curli and phosphoethanolamine cellulose associated with biofilm architecture and properties. *Biopolymers* (2021) *112*, 1–11.
128. Nicole, B., Alona, B., S., S. T., S., D. P. & Katharina, R. Permeability and Mechanics. *Rep Prog Phys* (2016) *78*, 36601.
129. Kreis, C. T. & Sullan, R. M. A. Interfacial nanomechanical heterogeneity of the: E. coli biofilm matrix. *Nanoscale* (2020) *12*, 16819–16830.
130. Lagendijk, E. L., Validov, S., Lamers, G. E. M., De Weert, S. & Bloemberg, G. V. Genetic tools for tagging Gram-negative bacteria with mCherry for visualization in vitro and in natural habitats, biofilm and pathogenicity studies. *FEMS Microbiology Letters* (2010) *305*, 81–90.
131. Schindelin, J., Arganda-Carreras, I., Frise, E., Kaynig, V., Longair, M., Pietzsch, T., Preibisch, S., Rueden, C., Saalfeld, S., Schmid, B., Tinevez, J. Y., White, D. J., Hartenstein, V., Eliceiri, K., Tomancak, P. & Cardona, A. Fiji: an open-source platform for biological-image analysis. *Nature Methods 2012 9:7* (2012) *9*, 676–682.
132. Ershov, D., Phan, M.-S., Pylvänäinen, J. W., Rigaud, S. U., Blanc, L. Le, Charles-Orszag, A., Conway, J. R. W., Laine, R. F., Roy, N. H., Bonazzi, D., Duménil, G., Jacquemet, G. & Tinevez, J.-Y. Bringing TrackMate into the era of machine-learning and deep-learning. *bioRxiv* (2021) 2021.09.03.458852.
133. Cornell, W. C., Morgan, C. J., Koyama, L., Sakhtah, H., Mansfield, J. H. & Dietrich, L. E. P. Paraffin embedding and thin sectioning of microbial colony biofilms for microscopic analysis. *Journal of Visualized Experiments* (2018) *2018*, 1–8.
134. Amini, S., Kolle, S., Petrone, L., Ahanotu, O., Sunny, S., Sutanto, C. N., Hoon, S., Cohen, L., Weaver, J. C., Aizenberg, J., Vogel, N. & Miserez, A. Preventing mussel adhesion using lubricant-infused materials. *Science* (2017) *357*, 668–673.
135. Zeng, G., Vad, B. S., Dueholm, M. S., Christiansen, G., Nilsson, M., Tolker-Nielsen, T., Nielsen, P. H., Meyer, R. L. & Otzen, D. E. Functional bacterial amyloid increases Pseudomonas biofilm hydrophobicity and stiffness. *Frontiers in Microbiology* (2015) *6*, 1–14.

136. Ziege, R., Tsirigoni, A.-M., Large, B., Serra, D. O., Blank, K. G., Hengge, R., Fratzl, P. & Bidan, C. M. Adaptation of Escherichia coli Biofilm Growth, Morphology, and Mechanical Properties to Substrate Water Content . *ACS Biomaterials Science & Engineering* (2021) *7*, 5315–5325.
137. Yanni, D., Kalziqi, A., Thomas, J., Ng, S. L., Vivek, S., Ratcliff, W. C., Hammer, B. K. & Yunker, P. J. Life in the coffee-ring: how evaporation-driven density gradients dictate the outcome of inter-bacterial competition. (2017) 1–12.
138. Choi, S., Stassi, S., Pisano, A. P. & Zohdi, T. I. Coffee-ring effect-based three dimensional patterning of micro/nanoparticle assembly with a single droplet. *Langmuir* (2010) *26*, 11690–11698.
139. Sharon, E., Marder, M. & Swinney, H. Leaves, Flowers and Garbage Bags: Making Waves. *American Scientist* (2004) *92*, 254.
140. McConnell, G., Trägårdh, J., Amor, R., Dempster, J., Reid, E. & Amos, W. B. A novel optical microscope for imaging large embryos and tissue volumes with sub-cellular resolution throughout. *eLife* (2016) *5*,.
141. Serra, D. O. & Hengge, R. A c-di-GMP-Based Switch Controls Local Heterogeneity of Extracellular Matrix Synthesis which Is Crucial for Integrity and Morphogenesis of Escherichia coli Macrocolony Biofilms. *Journal of Molecular Biology* (2019) *431*, 4775–4793.
142. Lucia Stecchini, M., Del Torre, M., Donda, S., Maltini, E. & Pacor, S. Influence of agar content on the growth parameters of Bacillus cereus. *International Journal of Food Microbiology* (2001) *64*, 81–88.
143. Kasyap, T. V., Koch, D. L. & Wu, M. Bacterial collective motion near the contact line of an evaporating sessile drop. *Physics of Fluids* (2014) *26*,.
144. Horkay, F. & Lin, D. C. Mapping the local osmotic modulus of polymer gels. *Langmuir* (2009) *25*, 8735–8741.
145. Duraj-Thatte, A. M., Courchesne, N. M. D., Praveschotinunt, P., Rutledge, J., Lee, Y., Karp, J. M. & Joshi, N. S. Genetically Programmable Self-Regenerating Bacterial Hydrogels. *Advanced Materials* (2019) *31*, 1–9.
146. Jeffries, J., Fuller, G. G. & Cegelski, L. Unraveling Escherichia coli 's Cloak: Identification of Phosphoethanolamine Cellulose, Its Functions, and Applications . *Microbiology Insights* (2019) *12*, 117863611986523.
147. Peterson, B. W., Busscher, H. J., Sharma, P. K. & Van Der Mei, H. C. Visualization of Microbiological Processes Underlying Stress Relaxation in Pseudomonas aeruginosa Biofilms. *Microscopy and Microanalysis* (2014) *20*, 912–915.
148. Zhang, Y., Debenedictis, E. P. & Keten, S. Cohesive and adhesive properties of crosslinked semiflexible biopolymer networks. *Soft Matter* (2019) *15*, 3807–3816.
149. Lau, P. C. Y., Dutcher, J. R., Beveridge, T. J. & Lam, J. S. Absolute quantitation of bacterial biofilm adhesion and viscoelasticity by microbead force spectroscopy. *Biophysical Journal* (2009) *96*, 2935–2948.
150. Kikuchi, T., Mizunoe, Y., Takade, A., Naito, S. & Yoshida, S. I. Curli fibers are required for development of biofilm architecture in Escherichia coli K-12 and enhance bacterial adherence to human uroepithelial cells. *Microbiology and Immunology* (2005) *49*, 875–884.
151. Chaudhuri, O., Gu, L., Klumpers, D., Darnell, M., Bencherif, S. A., Weaver, J. C., Huebsch, N., Lee, H. P., Lippens, E., Duda, G. N. & Mooney, D. J. Hydrogels with tunable stress relaxation regulate stem cell fate and activity. *Nature Materials* (2016) *15*, 326–334.

152. Oh, Y. J., Cui, Y., Kim, H., Li, Y., Hinterdorfer, P. & Park, S. Characterization of curli a production on living bacterial surfaces by scanning probe microscopy. *Biophysical Journal* (2012) *103*, 1666–1671.
153. Thongsomboon, W., Serra, D. O., Possling, A., Hadjineophytou, C., Hengge, R. & Cegelski, L. Modified Cellulose. (2018) *338*, 334–338.
154. Kim, Y. M. & Kwon, T. H. Entrapment of clay particles enhances durability of bacterial biofilm-associated bioclogging in sand. *Acta Geotechnica* (2022) *17*, 119–129.
155. Engler, A. J., Sen, S., Sweeney, H. L. & Discher, D. E. Matrix Elasticity Directs Stem Cell Lineage Specification. *Cell* (2006) *126*, 677–689.
156. Wloka, M., Rehage, H., Flemming, H. C. & Wingender, J. Rheological properties of viscoelastic biofilm extracellular polymeric substances and comparison to the behavior of calcium alginate gels. *Colloid and Polymer Science* (2004) *282*, 1067–1076.
157. Service, R. F. In 'living materials,' microbes are makers. *Science* (2020) *367*, 841.
158. Duraj-Thatte, A. M., Manjula-Basavanna, A., Courchesne, N. M. D., Cannici, G. I., Sánchez-Ferrer, A., Frank, B. P., van't Hag, L., Cotts, S. K., Fairbrother, D. H., Mezzenga, R. & Joshi, N. S. Water-processable, biodegradable and coatable aquaplastic from engineered biofilms. *Nature Chemical Biology* (2021).

DECLARATION OF ORIGINALITY/ EIDESSTATTLICHE ERKLÄRUNG

I hereby declare that this thesis work 'Growth dynamics and mechanical properties of *E. Coli* biofilms' is my work and that only the resources denoted were used. This thesis work has not been submitted for the award of any other degree to another university in this or similar form.

Hiermit erkläre ich, die vorliegende Arbeit zum Thema „Wachstumsdynamik und mechanische Eigenschaften von *E. coli* Biofilmen" selbstständig unter ausschließlicher Verwendung der angegebenen Literatur und Hilfsmittel erstellt zu haben. Die Arbeit ist bisher an keiner anderen Hochschule in dieser oder ähnlicher Form eingereicht worden.

Ricardo Ziege Potsdam-Golm, 24.02.2021

ACKNOWLEDGEMENTS

I want to thank Cécile, my supervisor, for her relentless help in developing the work of this thesis together with me and for the incredible attention she pays to all members of the group. Her creative, open and exploring personality was inspiring and strengthened my confidence to be a scientist and person with such attributes, in addition to scientific rigour. I also want to thank her and the whole group for creating an atmosphere of mutual respect and openness in opposition to a competitive mentality, which still is present in many scientific workplaces. Another point I was very pleased with from the very beginning, was the trust that was put in me, despite myself feeling inadequate and overwhelmed at times.

Another thank goes to the whole Biomaterials department of the Max-Planck Institute of Colloids and Interfaces and all the people present between February 2019 and March 2022. Many excellent scientists and still humble personalities were an encouraging, sometimes daunting environment to work in. An environment that encourages personal and professional growth rather than forcing outputs will stick with me. A special thanks to Prof. Peter Fratzl for stimulating scientific discussions and the exchange of ideas. I am pleased to have had two other good mentors as an associated member of the IMPRS graduate school on Multiscale Bio-systems. Prof. Kerstin Blank and Prof. Stefanie Barbirz, thanks for your help and input at our regular mentoring meetings. Furthermore, I want to acknowledge Prof. Regine Hengge and Dr Diego Serra from Humboldt University in Berlin for providing the *E. coli* strains used within the work of this thesis. Moreover, I want to recognize Dr. Shahrouz Amini for navigating difficulties, when indenting soft biological materials on the microscale and for his help with data analysis. Other thanks to Christine Pilz-Allen for being the most helpful lab technician I have encountered so far. And at last a more personal mention of Anna-Maria Tsirigoni and Hubert Taieb for being themselves and spending many fun evenings together.

After finishing my 1st year as a PhD candidate, the COVID-19 pandemic took its toll on all of us. As we are still in the pandemic, the fourth and fifth wave of infections are ravaging in Germany and it might be too early to understand all its effects on us and our societies. Still, we managed to continue working as described above, some felt more lonely, some less productive, some became depressed, whereas others enjoyed the slow-down of our ever-accelerating, often hectic lives. Yet, I am glad that the pandemic raised more awareness about mental health in

academia and senior scientists need to acknowledge that our science can just be as good as our students, PhDs, postdocs and group leaders ability to maintain and nurture their mental health apart from science. Where there is no break, where there is no free time the science will suffer. When there is no time to think, explore and prioritize, then there will be the repetition of non-reproducibility in academia. However, people in academia do organize and can bring a change. Therefore, a very last thanks go to the organizers of #IchbinHanna, fighting for better working conditions in academia in germany.

APPENDIX

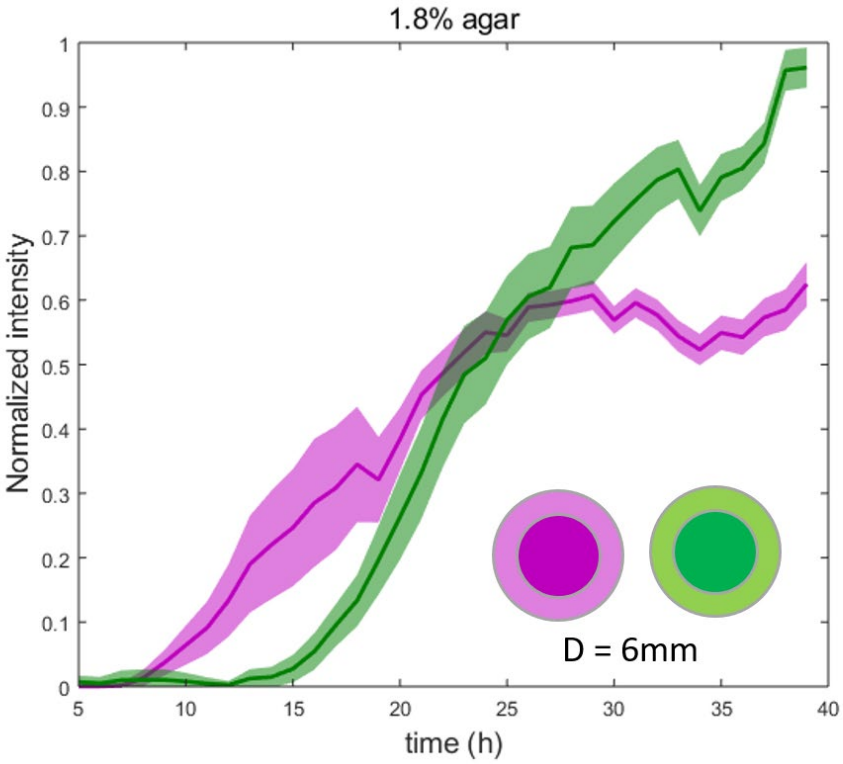

Appendix 1: Fluorescence intensity of mCherry and thioflavin S over time in the biofilm centre with an inner diameter of D = 6mm; normalization by thioflavin S maximum intensity.

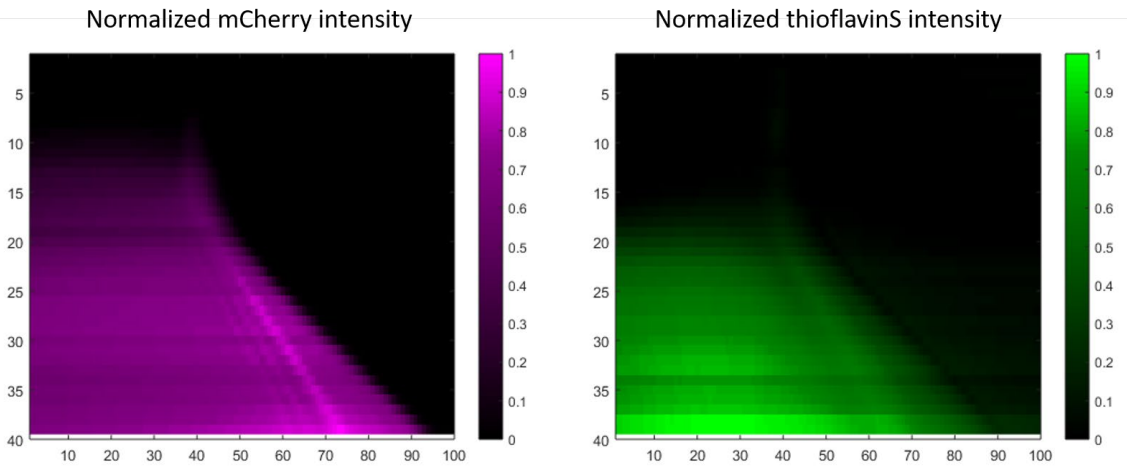

Appendix 2: Azimuthally averaged fluorescence intensity kymographs of mCherry (left) and thioflavinS (right), plotted over space (azimuthally averaged and normalized radius ; 0 – 100) and time (0 - 40h).

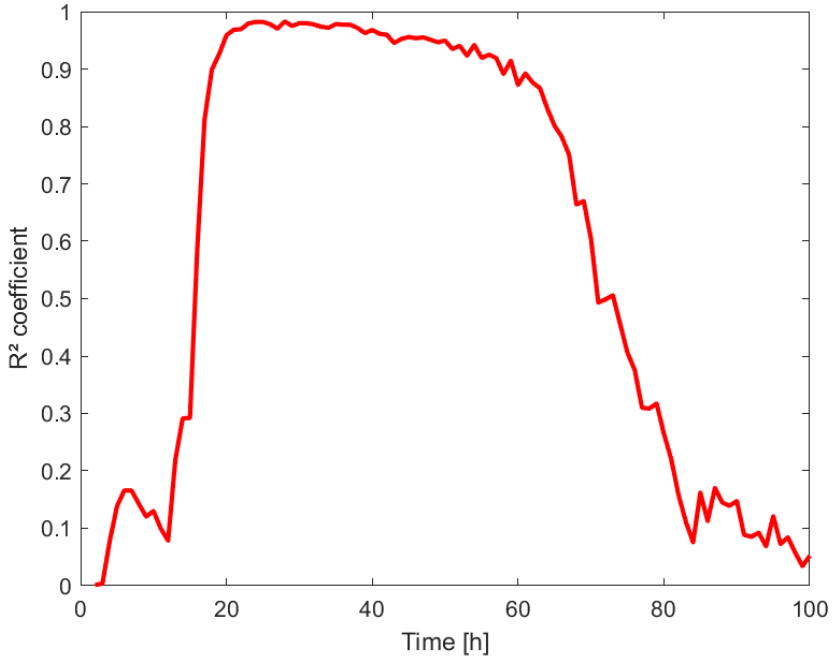

Appendix 3: R^2 coefficient of the linear fit of the velocity profiles corresponding to Fig. 18C.

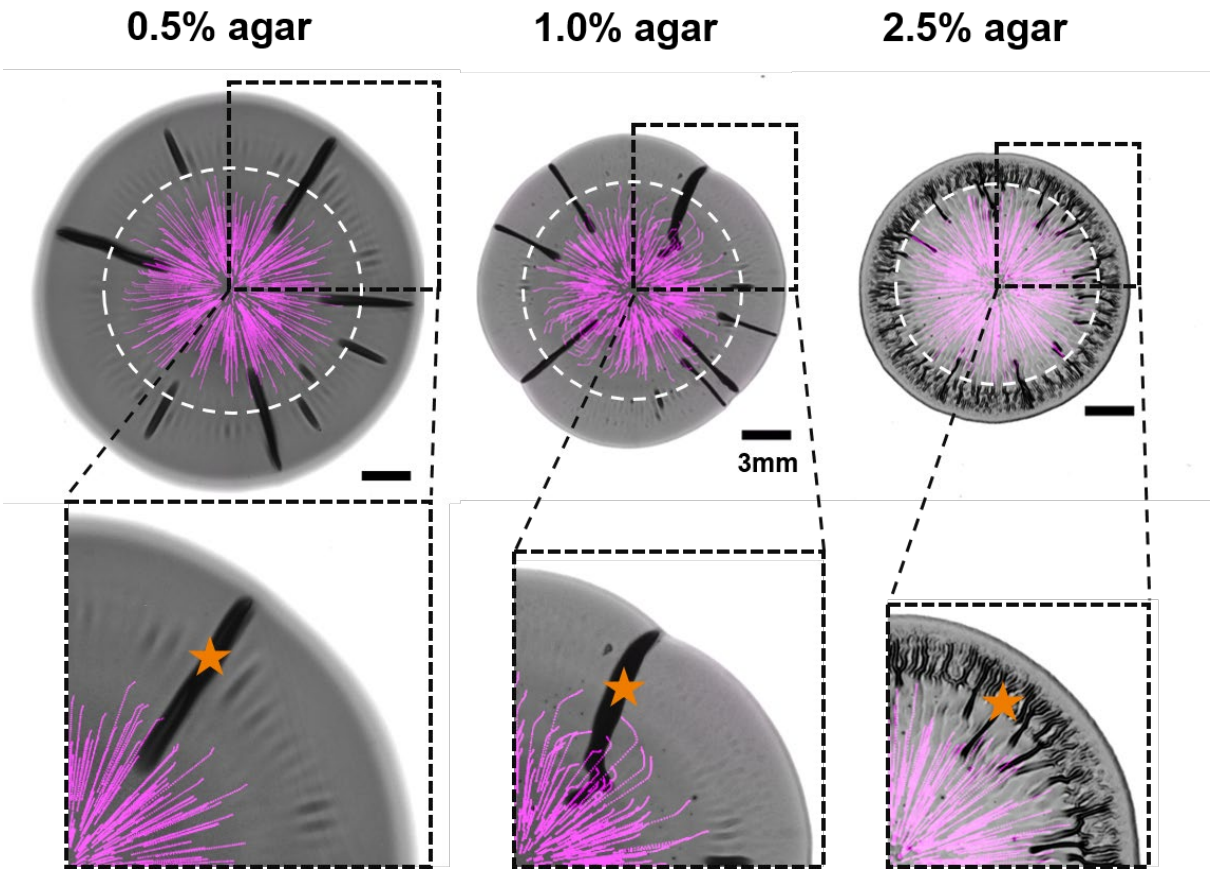

Appendix 4: Particle trajectories overlayed over brightfield images of *E. coli* biofilms grown on respective agar concentration, indicated by stars is a region where delaminated buckles initially form.

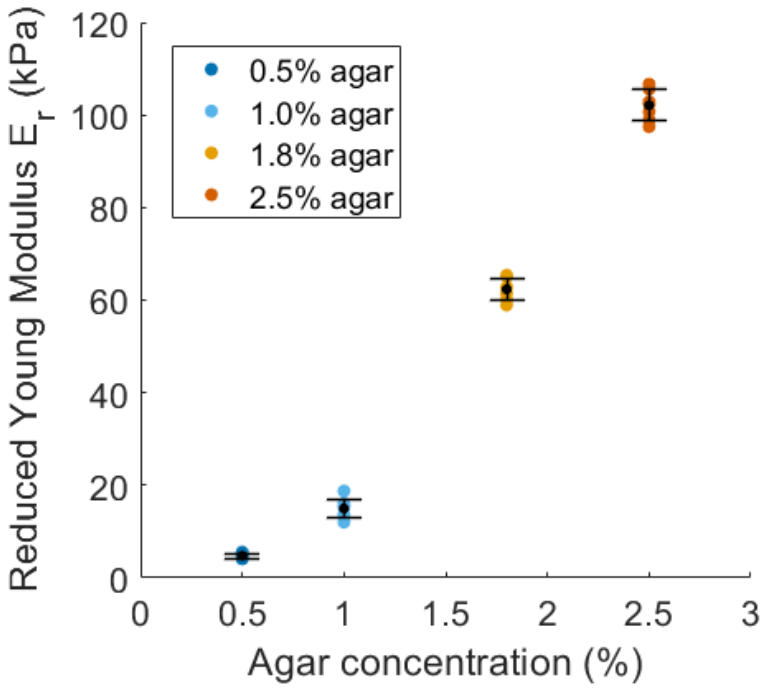

Appendix 5: Averaged reduced Young modulus E_r values, describing the measured rigidity of the substrate surface by nanoindentation (from 0.5% to 2.5% agar: 4.8 ± 0.5 kPa, 15.0 ± 2.1 kPa, 62.3 ± 2.4 kPa, 102.1 ± 3.4 kPa; n = 7-8 individual measurements).

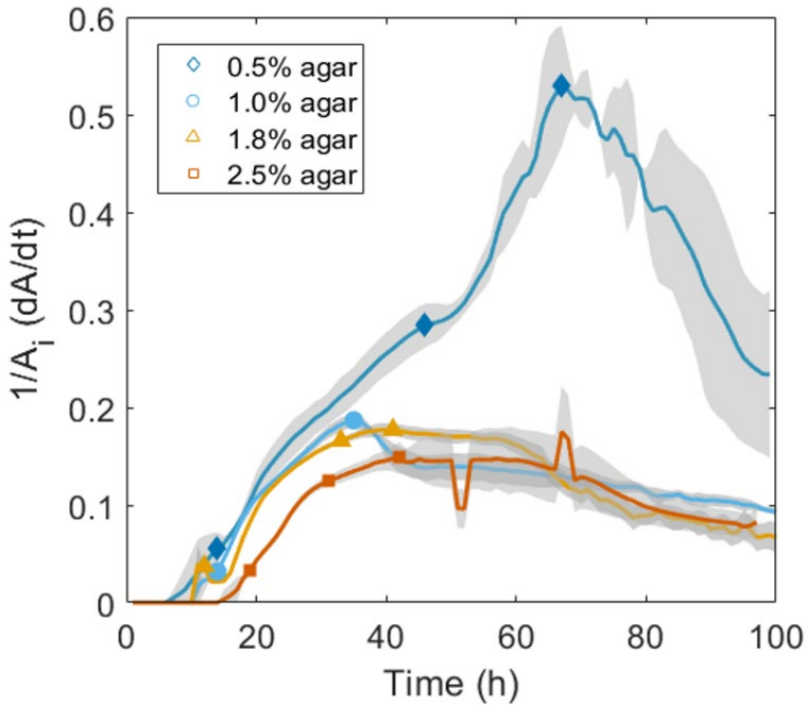

Appendix 6: Relative area spreading rates of *E. coli* AR3110 biofilms grown on agar of different agar concentrations, calculated from the derivative $1/A_i * dA/dt$.

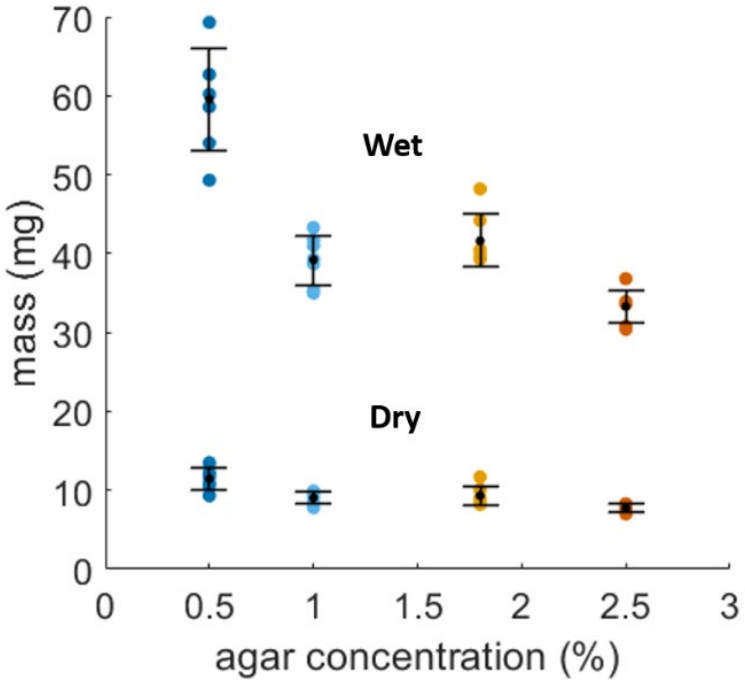

Appendix 7: Wet and corresponding dry biofilm mass from gravimetric measurements.

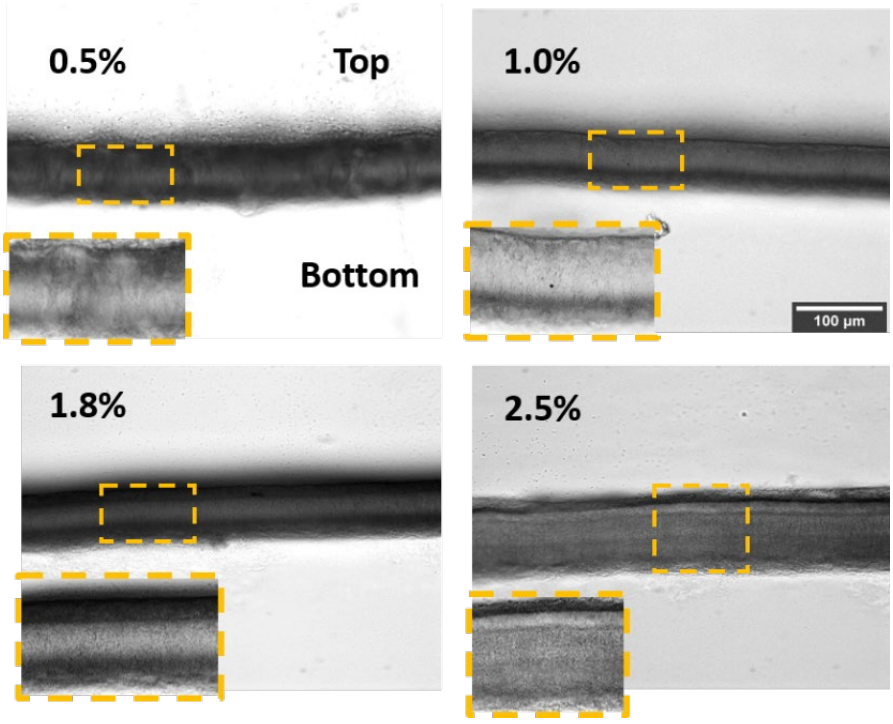

Appendix 8: Brightfield images of cross-sections corresponding to the fluorescence intensity images shown in Fig. 22C.

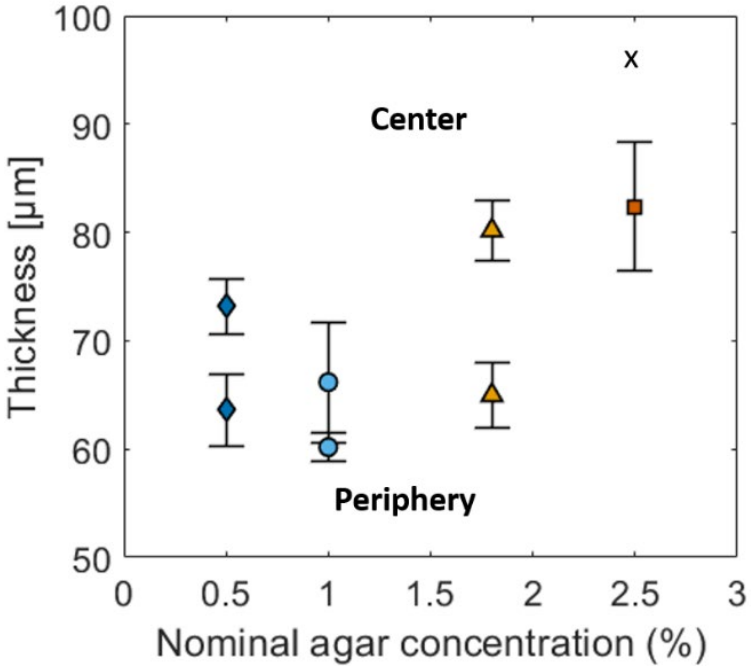

Appendix 9: Average biofilm thicknesses (n = 10) measured on brightfield images on central and peripheral biofilm cross-sections.